2012

Contribution of active site dynamics to enzyme catalysis: study on a series of mutants of dihydrofolate reductase

Vanja Stojkovic
University of Iowa

CONTRIBUTION OF ACTIVE SITE DYNAMICS TO ENZYME CATALYSIS: STUDY ON A SERIES OF MUTANTS OF DIHYDROFOLATE REDUCTASE

by

Vanja Stojković

An Abstract

Of a thesis submitted in partial fulfillment of the
requirements for the Doctor of Philosophy degree
in Chemistry in the Graduate College of
The University of Iowa

December 2012

Thesis Supervisor: Professor Amnon Kohen

ABSTRACT

This thesis describes an effort to expand current knowledge of catalysis in biological systems. The focus is on understanding how enzymes activate covalent bonds and specifically to study C-H bond activation *via* enzymes. The work presented here examined the role of protein dynamics and hydrogen tunneling in enzyme catalysis. Dihydrofolate reductase from *Escherichia coli* (*ec*DHFR), which catalyzes a single hydride transfer reaction, was selected as the model system for these studies. Intrinsic kinetic isotope effects (KIEs) have been shown to be highly sensitive probes in examining the chemical steps of enzymatic reactions, especially since they can indirectly infer the role of certain dynamic fluctuations in the *ec*DHFR-catalyzed reaction. This study provides evidence in support of the phenomenological Marcus-like model presently well accepted amongst both experimental enzymologists and some members of the computational community—this model suggests that certain molecular fluctuations prevail during the enzyme- catalyzed hydrogen transfer reaction and assist the chemical step. Previous studies of the temperature-dependence of KIEs focused on examining the network of residues that are dynamically linked to the hydride-transfer step and are localized far from the active site; a network initially proposed by computational studies. This thesis, on the other hand, focuses on the effect of the active site environment on the C-H→C transfer. While no spectroscopy experiments were performed to measure the dynamics in the active site, sensitive kinetic experiments were used to examine the physical features of the C-H→C transfer via rigorous perturbation of the donor-acceptor-distance (DAD). KIE measurements on a series of carefully designed active site mutants have been interpreted using a Marcus-like model and complemented by results obtained via molecular dynamic simulations and x-ray crystallography. Active site mutants were designed to alter the DAD and its dynamics in a controlled manner with a minimal effect

on the active-site electrostatics. The results suggest that the mutations have affected the reorganization energy necessary for the system to reach the transition state and have modulated the average DAD as well as its distribution at the transition state. The study on the active-site mutants was extended on N23PP—a dynamically altered mutant that was the source of an extensive debate in the field due to opposing views regarding the altered dynamics and its role in assisting the hydride transfer step. Findings presented in this thesis indicate that temperature dependent kinetic complexity masked the intrinsic KIEs in the earlier studies, and that our methodology revealed the significant differences between the natures of the hydride transfer catalyzed by the WT and by the dynamically impaired mutant. Collectively these results further our understanding of the role of enzyme dynamics and quantum tunneling in enhancing enzymatic reactions. In the future these results will be correlated to findings from vibrational spectroscopy, high-level calculations and NMR studies (as they become available) in order to establish the structure-dynamic-function-relationship both in *ec*DHFR and in enzymes in general.

Abstract Approved:_____
Thesis Supervisor

_____
Title and Department

_____
Date

CONTRIBUTION OF ACTIVE SITE DYNAMICS TO ENZYME CATALYSIS: STUDY ON A SERIES OF MUTANTS OF DIHYDROFOLATE REDUCTASE

by

Vanja Stojković

A thesis submitted in partial fulfillment
of the requirements for the Doctor of
Philosophy degree in Chemistry
in the Graduate College of
The University of Iowa

December 2012

Thesis Supervisor: Professor Amnon Kohen

Graduate College
The University of Iowa
Iowa City, Iowa

CERTIFICATE OF APPROVAL

_____

PH.D. THESIS

_____

This is to certify that the Ph.D. thesis of

Vanja Stojković

has been approved by the Examining Committee
for the thesis requirement for the Doctor of Philosophy
degree in Chemistry at the December 2012 graduation.

Thesis Committee: _____
Amnon Kohen, Thesis Supervisor

_____
Maxwell Geng

_____
James Gloer

_____
Ernesto Fuentes

_____
Daniel Quinn

To my parents

Kod unutarnjih borba koje čovjek vodi sa samim sobom i sa nepoznatim silama u sebi, važi više nego igdje pravilo: ne predaj se nikad! — Ni predaje, ni ustupanja! A prije svega, što kažu u Bosni: ne veži tugu za srce!

Ivo Andrić
"Znakovi pored puta"

ACKNOWLEDGMENTS

I am sincerely grateful and indebt to all the scientists and scholars I encountered during my PhD studies, especially: Dr. Sonya Franklin, Dr. Samantha Nolting and Dr. Jennifer Wong-Deyrup from the Franklin research group; Dr. Arundhuti Sen, Eric Koehn, Daniel Roston, Zhen Wang, Thelma Abeysinghe from Kohen research group at University of Iowa. Many thanks to Dr. Lokesh Gahkar from the protein crystallography facility at the University of Iowa for all the assistance and support in my protein crystallography endeavors. I would also like to thank all the present and past members of the Kohen group for providing a great working environment. Thanks go also to all the staff at Department of Chemistry and Department of Biochemistry who facilitated this research.

I am indebt to my advisor Dr. Amnon Kohen for the mentorship, guidance and support through out the years. Amnon, thank you for both the criticism and encouragement, for always keeping me focused on the big picture and for believing in me.

Big thanks to my wonderful parents, Stojanka and Bratislav, who even though being physically far away, were always there to give me support and strength to keep on going. No words can describe my gratitude. Many thanks to my sister Bojana, Ian and Lana, and many friends who were my family away from home: my co-housemates Nina, Ana, Tomislav and Juan, and many others both near and far, especially Jelena, Frane, Modei, and my Gaia's girls. I would not be able to do it without any of you. Thank you!

ABSTRACT

This thesis describes an effort to expand current knowledge of catalysis in biological systems. The focus is on understanding how enzymes activate covalent bonds and specifically to study C-H bond activation *via* enzymes. The work presented here examined the role of protein dynamics and hydrogen tunneling in enzyme catalysis. Dihydrofolate reductase from *Escherichia coli* (*ec*DHFR), which catalyzes a single hydride transfer reaction, was selected as the model system for these studies. Intrinsic kinetic isotope effects (KIEs) have been shown to be highly sensitive probes in examining the chemical steps of enzymatic reactions, especially since they can indirectly infer the role of certain dynamic fluctuations in the *ec*DHFR-catalyzed reaction. This study provides evidence in support of the phenomenological Marcus-like model presently well accepted amongst both experimental enzymologists and some members of the computational community—this model suggests that certain molecular fluctuations prevail during the enzyme- catalyzed hydrogen transfer reaction and assist the chemical step. Previous studies of the temperature-dependence of KIEs focused on examining the network of residues that are dynamically linked to the hydride-transfer step and are localized far from the active site; a network initially proposed by computational studies. This thesis, on the other hand, focuses on the effect of the active site environment on the C-H→C transfer. While no spectroscopy experiments were performed to measure the dynamics in the active site, sensitive kinetic experiments were used to examine the physical features of the C-H→C transfer via rigorous perturbation of the donor-acceptor-distance (DAD). KIE measurements on a series of carefully designed active site mutants have been interpreted using a Marcus-like model and complemented by results obtained via molecular dynamic simulations and x-ray crystallography. Active site mutants were designed to alter the DAD and its dynamics in a controlled manner with a minimal effect

on the active-site electrostatics. The results suggest that the mutations have affected the reorganization energy necessary for the system to reach the transition state and have modulated the average DAD as well as its distribution at the transition state. The study on the active-site mutants was extended on N23PP—a dynamically altered mutant that was the source of an extensive debate in the field due to opposing views regarding the altered dynamics and its role in assisting the hydride transfer step. Findings presented in this thesis indicate that temperature dependent kinetic complexity masked the intrinsic KIEs in the earlier studies, and that our methodology revealed the significant differences between the natures of the hydride transfer catalyzed by the WT and by the dynamically impaired mutant. Collectively these results further our understanding of the role of enzyme dynamics and quantum tunneling in enhancing enzymatic reactions. In the future these results will be correlated to findings from vibrational spectroscopy, high-level calculations and NMR studies (as they become available) in order to establish the structure-dynamic-function-relationship both in *ec*DHFR and in enzymes in general.

TABLE OF CONTENTS

LIST OF TABLES

LIST OF FIGURES

CHAPTER 1.
INTRODUCTION

1.1 Scope of Research

The broad scope of research presented here is to find a better understanding of C-H bond activation in enzymes. Our investigation focused on several important topics: (i) exploration of the role of enzyme dynamics in enhancing the chemical reaction, (ii) examination of the physical features of a C-H-C transfer and lastly (iii) the assessment of the role of the specific active site residues in assisting chemical transformations in enzymes. In order to investigate these issues, the nature and the molecular mechanism of the specific chemical transformation were assessed experimentally, through kinetic studies and X-ray crystallography, and computationally by classical mechanics molecular dynamic (MD) simulations. We decided to focus on the C-H bond cleavage and hydride transfer in a well-studied C-H→C system of biological and medical importance – dihydrofolate reductase from *Escherichia coli* (*ec*DHFR).

*Ec*DHFR is a small, flexible enzyme that catalyzes a single C-H→C transfer. Its structure and kinetic mechanism have been vastly studied throughout the years, making it a paradigm in numerous experimental studies as well as in theoretical investigation. Based on the large scope of knowledge available for this enzyme and the fact that it is easy to control, manipulate, simulate, and determine its structure, make it an excellent model for the investigations in hand. The main focus of our study was to examine the possible role of several active site residues in assisting the hydride transfer. The nature of the hydride transfer was studied via perturbation of the potential surface through active site mutations. Specifically, we focused on two hydrophobic active-site residues, I14 and F31, situated behind the cofactor and substrate, respectively. Systematic reduction of

these residues, to smaller hydrophobic ones, enabled us to make a control change in the active site with minimal alteration of the active-site electrostatics. Such controlled change is a holy grail and an extremely difficult task to achieve in most relevant studies of enzymes and solution reactions. Additionally, we extended the study on the active site mutants to a distal *ec*DHFR mutant (N23PP) that was designed to dynamically resemble human DHFR and was shown to have impaired active-site dynamics on micro-millisecond timescale.[1] All mutants were studied via temperature dependence of kinetic isotope effects (KIEs); the dynamics of their respective donor-acceptor distances through MD simulations, and the ground state structures were assessed through X-ray structures of relevant ternary complexes. This experimental approach was aimed at developing a framework for the examination of the structure-function-dynamics relationship in enzymatic C-H-C transfer in particular, and solution in general.

1.2 Thesis overview

The work presented in this thesis focused on several different aspects of DHFR studies. In chapter II, we present novel chemoenzymatic syntheses of radiolabeled nicotinamide adenine compounds that can be used in kinetic studies as well as for the determination of isotope effects in $NAD(P)^+$/NAD(P)H-dependent enzymes. The microscale synthesis of these sterospecifically labeled nicotinamides allowed for an alternative and cheaper way to produce radiolabeled $NAD(P)^+$/NAD(P)H. Chapter III focuses on implementing radiolabeled cofactors in measuring the temperature dependence of kinetic isotope effects (KIEs), as well as MD simulation studies on a series of mutants of residue 14 in order to determine the role of this residue in assisting hydride transfer. This work was extended in chapter IV, which includes a detailed structural study on the same series of active site mutants. Chapter V extends the work presented in chapters III and IV and is comprised of the structural/kinetic/computational

studies on another active site residue, F31. Chapter VI is somewhat different from the other chapters in that it is concerned with probing the effect of the distal mutation N23PP on the nature of the hydride transfer.

1.3 Background

1.3.1 Dihydrofolate reductase (DHFR)

*Ec*DHFR (E.C. 1.5.1.3) is a small, monomeric enzyme (18 kDa) that plays a central role in maintenance of the cellular pools of tetrahydrofolate, which is essential for the synthesis of purines and therefore is crucial for cell growth and proliferation. Due to its pivotal role in nucleotide biosynthesis in many organisms, DHFR has been the target for many antibiotic and chemotherapeutic agents[2] and an excellent platform for genetic and evolutionary analysis.[3] Consequently, DHFR has been studied by different experimental methods in order to gain understanding of its structure,[4] dynamics,[5] and kinetics.[6]

This NADPH-dependent oxidoreductase catalyzes the reduction of 7,8-dihydrofolate (H_2F) to 5,6,7,8-tetrahydrofolate (H_4F) by stereospecific transfer of a hydride from the pro-*R* C4 position of NADPH to the *re* face of C6 atom of the pterin ring (Figure 1.1.a). It was initially suggested that the hydride transfer occurs concomitant to protonation at N5 position on the pterin ring of H_2F,[7] however, certain experimental and computational work showed that hydride transfer is subsequent to protonation at the N5 position (Figure 1.1).[6,8-10] The only ionizable group within the active site that could act as a Lewis acid and donate hydrogen to the N5 is Asp 27. This has been supported by kinetic studies that showed that the rate of the hydride transfer is pH dependent, with a pKa of 6.5 – that has been attributed to Asp 27.[6] However, some computational work[11] coupled with experimental evidence[12] suggested that protonation occurs through a solvent molecule. Extensive kinetic studies on the *ec*DHFR have shown that its kinetic cascade is

quite complex, where the rate limiting step at pH 7 is release of the product H_4F from the abortive complex with NADPH (Figure 1.1.b). At this pH and 25˚C, k_{cat} is 12 s^{-1} and the hydride transfer rate, under pre-steady state conditions is measured to be 220 s^{-1}.[6] At pH values higher than 8 hydride transfer becomes more rate-determining.

The biological importance of *ec*DHFR has prompted numerous structural investigations over the years. Currently, there are more than 40 structures of *ec*DHFR available in various ligated states. This enzyme has an α/β structure consisting of a central eight-stranded β-sheet and four α-helices connected with several loop regions (Figure 1.2). The active site region divides the protein into two subdomain regions: adenosine binding subdomain and major subdomain. The major subdomain is dominated by three loops on the ligand binding face that surround the active site. The loops are termed: M20 (residues 9-24), F-G (residues 116-132), and G-H (residues 142-150). Extensive X-ray studies showed that M20 loop can adopt four characteristic conformations and its movement is coordinated with different stages of the catalytic cycle. NMR relaxation experiments confirmed the ground state conformational heterogeneity to be a common feature of DHFRs from different sources. It also suggested that the movement of the M20 loop might modulate the turnover rate by limiting the rate of product dissociation, as the flexibility of the M20 loop occurs on a relevant timescale (~2-40 s^{-1}).[13] Subsequent NMR relaxation experiments suggested that binding of different ligands resulted in dynamic changes in the regions both proximal and far removed from the active-site, including the portions of the three flexible loops. Moreover, it was suggested that the M20 loop may also contribute to catalysis through active site compression and stabilization of the transition state.[14] NMR studies of the ternary enzyme-$NADP^+$-folate complex (mimic of Michaelis complex; Figure 1.2) have revealed dynamic rotamer averaging about the χ1 dihedral angle for several threonine, isoleucine and valine residues that are in the interface between the M20 and F-G loops.[15] One of such residues is residue I14, which populates both gauche and trans rotameric states in

solution, and is situated just behind the nicotinamide ring of the cofactor. Since the optimal geometry for hydride transfer involves sub-van der Waals contacts between the hydride donor and acceptor it was proposed that dynamic sampling of the trans rotamer of I14 could play a role in transition state stabilization, thereby facilitating the hydride transfer.[15]

A number of theoretical studies over the years on *ec*DHFR provided a way to identify motional correlations between different parts of the protein, and to examine the dynamics of transient complexes. For example, molecular dynamic (MD) simulations identify motions of the several residues in the F-G loop to be coupled to motions of a number of active site residues, including I14 (part of the M20 loop) and F31.[16] Both of these residues are in direct contact with cofactor and substrate, respectively. The aforementioned NMR relaxation experiments suggested rotamer averaging of residue I14 in solution, a phenomenon which was not observed in the X-ray crystal structures, but which was confirmed by the MD simulations.[17] Quantum/classical molecular dynamics approach allowed for the identification of the network of coupled motions extending throughout the protein and ranging from the femtosecond to millisecond timescale.[18,19] "Promoting motions" refers to the thermally averaged structural changes that occur as the system proceeds from the ground state Michaelis complex to transition state to product. The simulation indicated that several active site residues, including the already mentioned I14 and F31, participate in the network of promoting motions. More specifically, the side chains of these residues were suggested to aid in directing cofactor or substrate towards each other, as was previously suggested through experimental studies. The experimental approach that was used to indirectly infer the role of the fast-timescale dynamics in assisting catalyzed reaction is temperature dependence of KIEs (presented in detail in Chapter 3, for mutants of I14, and Chapter 5 for the F31V mutant).

1.3.2 Kinetic isotope effect (KIE)

An isotope effect is the ratio of any property between two compounds that differ only in their isotopic composition (isotopologues). Isotope effects are among the most powerful tools available to both physical organic chemists as well as mechanistic enzymologists due to the amount and different types of information one can obtain. Isotope effects are very useful for studying the reaction coordinate of the enzymatic reaction because they are isosteric and isoelectronic and therefore nonperturbing. However, isotope effects do reflect changes in vibrational frequencies of reactants as they are converted to products in the rate-determining transition states. Application of isotope effects is vast, as they can probe kinetic mechanisms, yielding both quantitative and qualitative information, as well as give information about regulatory kinetic mechanisms such as chemical interconversions, reactant release, etc.[20]

The KIE is the ratio of reaction rates of two isotopologues. Two types of KIEs can be defined: primary (1˚) KIEs that refer to an isotopic substitution of an atom that is being transferred during the reaction, and secondary (2˚) KIEs, where the labeled atom is proximal to the atom being transferred. 2˚ KIEs have been used extensively in studies of H-tunneling,[21-25] however, in work presented here, only 1˚ KIEs have been employed. 1˚ hydrogen KIEs proved to be particularly interesting because: (i) the mass ratio of its isotopes is larger than for any other element, leading to large KIE values, and (ii) the mass of hydrogen is small enough so that the quantum effects are more likely to be significant.[25-28] If non-classical behavior, such as quantum mechanical (QM) tunneling, does not contribute to the reaction rate, the rate of the transfer as well as activation energies between different isotopes will mostly differ based on their zero point energies (ZPE) between the ground state vs. transitions state (Figure 1.3). A detailed treatment of transition-state theory (TST) leads to the Bigeleisen equation, in which the KIE is simply a ratio of the TST rate constant for the light and the heavy isotopes:

$$KIE = \frac{k_L^{TST}}{k_H^{TST}} = \frac{\kappa_L MMI_L EXC_L ZPE_L}{\kappa_H MMI_H EXC_H ZPE_H} \quad (1)$$

where κ, MMI, EXC, and ZPE refer to the transmission coefficient, mass moment of inertia (rotational and translational partition functions), contributions from excited state populations, and zero point energies, respectively, and the subscripts indicate the light (L) and heavy (H) isotopes. In general, computing the complete partition function for a system is infeasible, therefore, certain approximations are deemed useful. For example, the MMI term, in the most enzymatic systems, is negligible due to the overall large mass of the system. Moreover, since most enzymes are active only over a small temperature range, the excited states do not contribute significantly to the overall rate. Therefore, equation (1) reduces to the isotopic difference in the ZPE in the ground state vs. transition state:

$$\frac{k_L}{k_H} \approx \frac{\kappa_L}{\kappa_H} \exp \frac{\Delta G_H - \Delta G_L}{RT} \quad (2)$$

where $\Delta G^{\ddagger}$ represents the activation energy. The transmission coefficient is often assumed to be equal to unity, however, quantum mechanical tunneling and dynamic effects such as barrier recrossing can lead to large isotopic differences in κ.

This model predicts the a primary k_H/k_D KIE of 6.9 for C-H cleavage at 298 K, if we assume a stretching frequency of ~3000 cm^{-1} for a C-H bond and 2200 cm^{-1} for a C-D bond[29]. A similar frequency of 1800 cm^{-1} for C-T gives primary k_H/k_T=18 at the same temperature.

1.3.3 Swain-Schaad exponent

In the instances where quantum mechanical tunneling does not contribute to the reaction rate, and where the difference in the reaction rates between different isotopes depends on the difference in ZPE, the H/D/T KIEs follow a semiclassical pattern denoted as the Swain-Schaad relationship. These relationships are derived from the semi-classical

description of the rate (*vide infra*), and are determined from the reduced masses of the participating molecules. For the simple single-barrier hydride transfer reaction, the Swain-Schaad relationship can be described by the following equation:

$$\frac{k_H}{k_T} = \left(\frac{k_H}{k_D}\right)^{EXP} \qquad (3)$$

where k_i is the rate-constant for particular isotope (in the above equation, the reference isotope is hydrogen) and EXP is the Swain-Schaad exponent (SSE) and is calculated from the reduced masses of the reactants. For equation (3), where hydrogen is used as a reference isotope, the SSE will be presented by the equation (4):

$$SSE = \frac{\ln\left(\frac{k_H}{k_T}\right)}{\ln\left(\frac{k_H}{k_D}\right)} = \frac{1/\sqrt{\mu_H} - 1/\sqrt{\mu}_T}{1/\sqrt{\mu}_H - 1/\sqrt{\mu_D}} = 1.42 \qquad (4)$$

On the other hand, when tritium is used as an isotope of reference, then we obtain the following value:

$$SSE = \frac{\ln\left(\frac{k_H}{k_T}\right)}{\ln\left(\frac{k_D}{k_T}\right)} = \frac{1/\sqrt{\mu_H} - 1/\sqrt{\mu}_T}{1/\sqrt{\mu}_D - 1/\sqrt{\mu_T}} = 3.34 \qquad (5)$$

where μ_i is the reduced mass of isotope i and k_i is the rate for the same isotope. Semi-classically, the SSE is a constant for all reactions. For many reactions, the measured KIEs fall well within the semi-classical range (Table 1.1), however, the deviation of the SSE from its semi-classical value has served as a benchmark for tunneling.[30]

A very sensitive probe for studying tunneling and coupled motion is the mixed labeled SSE (mSSE).[22,31,32] In mSSE experiments, one measures the 2˚ H/T KIE, with hydrogen at the primary position, and 2˚ D/T KIE, with deuterium at the primary position. Semi-classically, there are no isotope effects on isotope effects (the rule of the geometric mean),[33] so the mSSE is:

$$mSSE = \frac{\ln(\frac{k_H^H}{k_T^H})}{\ln(\frac{k_D^D}{k_T^D})} \qquad (6)$$

where k_j^i indicates the rate with isotope *i* at the 1° position and *j* at the 2° position. Deviation from this value has been used as an indication of existence of tunneling and coupled motions in reactions.[23]

1.3.4 Kinetic complexity

Interpretation of data from KIE experiments proves to be quite challenging due to kinetic complexity, a feature common to enzymatic systems where the slower isotopically insensitive kinetic steps (*e.g.*, substrate binding, conformational changes of intermediates, product release, etc.) mask the intrinsic KIE.[34,35] As a result, under steady state conditions, for both k_{cat} and k_{cat}/K_m, the observed KIE (KIE_{obs}) is often smaller than the intrinsic KIE (KIE_{int}). In situations where only one step in an enzymatic reaction is isotopically sensitive, and KIEs are measured by a competitive method (see Chapter 2 for details), the equation for the KIE on k_{cat}/K_m can be defined by the following equation:

$$KIE_{obs} = \frac{KIE_{int} + C_f + C_r \cdot EIE}{1 + C_f + C_r} \qquad (7)$$

where C_f and C_r are forward and reverse commitments, respectively.[36] Several methods have been used to unmask KIE_{int} from KIE_{obs} and to provide direct information about the chemical step in the context of a kinetic cascade that involves other steps.[34,35,37] Three of these methods, which have been designed according to the specific system under study and the instrumentation available, are: pre-steady state measurements, the Northrop method, and the multiple KIEs method. The first and last methods are described elsewhere,[36], however we have shown (as presented in Chapter 6) that the former one has some disadvantages since even under the single-turnover conditions, the rates measured

for some enzymatic systems are not commitment-free. The Northrop method, developed for hydrogen isotopes, requires measurements of KIEs for all three isotopes of hydrogen. This method can be used only when the equilibrium isotope effect (EIE) is close to unity or when the reaction is irreversible. Under these assumptions, equation (7) can be rewritten to contain single commitment C. Moreover, if one measures the deuterium and tritium KIEs on k_{cat}/K_m, KIE_{int} will be related by equation (8):

$$(\frac{k_H}{k_D})_{obs} - 1 = \frac{(\frac{k_H}{k_D})_{\text{int}} - 1}{1 + C} \qquad \text{and} \qquad (\frac{k_H}{k_T})_{obs} - 1 = \frac{(\frac{k_H}{k_T})_{\text{int}} - 1}{1 + C} \qquad \text{so that}$$

$$\frac{(\frac{k_H}{k_D})_{obs} - 1}{(\frac{k_H}{k_T})_{obs} - 1} = \frac{(\frac{k_H}{k_D})_{\text{int}} - 1}{(\frac{k_H}{k_T})_{\text{int}} - 1} \qquad (8)$$

Assuming the Swain-Schaad relationship between the isotopes as presented in equations (4) and (5), one can obtain equation (9).

$$\frac{^{D}(\frac{k_{cat}}{K_m}) - 1}{^{T}(\frac{k_{cat}}{K_m}) - 1} = \frac{^{D}k - 1}{(^{D}k)^{1.43} - 1} \qquad (9)$$

One can extract the intrinsic values from equation (9) by finding the numerical solution from reference tables[38] or by computer programs, such as one available free of charge here: http://cricket.chem.uiowa.edu/~wang11/temp/intrin.html

1.3.5 Temperature dependence of KIEs as a probe for enzymatic quantum mechanical tunneling: semi-classical models with tunneling correction

One of the first models that addressed the phenomenon of hydrogen QM tunneling, observed initially in organic solutions, was the Bell model. In general terms,

QM tunneling occurs when the probability of finding the particle in the reactant well overlaps with the probability of finding the particle in the product well (Figure 1.4). A more precise description would be that the wave function for the particle at the reactant well (Ψ_r) interacts with the wave function in the product state (Ψ_p). In a ground state, the two new wave functions ($\Psi_r+\Psi_p$ and $\Psi_r-\Psi_p$) would lead to two new energy levels, a phenomenon termed as tunneling splitting. At the non-stable state (e.g. TS), this phenomenon will lower the effective barrier (ΔE_a) and affect the transmission coefficient.

According to the Bell model, H-transfer can be described by the semi-classical TST with the addition of a multiplier term (Q_t) that indicates the probability that the particle will move through an inverse parabolic barrier (equation (10)):

$$k_{obs} = Q_t * k_{SC}$$
$$Q_t = \frac{1}{k_B T} e^{\frac{E}{k_B T}} \int G(W) e^{-\frac{W}{k_B T}} \qquad (10)$$

where W represents the energy of the particle, and k_B is a Boltzman constant. Barrier penetration occurs just below the classical transition state, and its effect is predicted to be most significant for the lightest isotope. This results in both a primary H/D KIE exceeding the semiclassically predicted value of 7 for C-H bond cleavage, and in isotopic differences in activation energy (ΔE_a) and A_L/A_H to be smaller than limits predicted by the semi-classical model (Table 1.1).

Recently, temperature dependence of KIEs has become another way to probe enzymatic reactions in establishing contribution from tunneling.[39] Analysis of the Arrhenius parameters can yield a large amount of information regarding the nature of the tunneling. According to the Arrhenius equation, the rate of the reaction is exponentially proportional to E_a, and the reaction's absolute temperature, and since the KIE is, as mentioned, a ratio of the rates, its temperature dependency will follow:

$$\frac{k_L}{k_H} = \frac{A_L}{A_H} \exp \frac{\Delta E_a}{RT} \qquad (11)$$

where A is the Arrhenius pre-exponential factor and ΔE_a is the isotopic difference in activation energy. As evident from Figure 1.5, Arrhenius plots of a reaction in different temperature regimes can yield vastly different results for both A_L/A_H and ΔE_a. For majority of the enzymatic systems, only a narrow experimental temperature range is available (0-80˚C), thus the plot of ln(k) *vs*. 1/T often appears linear. At the high temperature end, the slope of the Arrhenius plot is exponentially proportional to ΔE_a (region I). At very low temperatures, only tunneling contributes significantly to rates due to the lack of thermal energy (region III). Consequently, the rates are temperature independent, and KIEs are very large and temperature independent. As a result, A_L/A_H, which are intercept values of the tangent to the plot in Figure 1.5, are expected to be inflated in comparison to the high temperature limit. In region II, which includes the experimental temperature for the majority of enzymatic systems, Arrhenius plots of the KIEs will be curved as the lighter isotope has the higher probability to tunnel at the higher temperature than the heavier one. As a result, the plot will appear very steep and A_L/A_H is expected to be smaller than unity.[40-42] The value of using isotope effects on Arrhenius preexponential factor as means to determine the extent of tunneling in enzymatic systems has been reviewed extensively, and the semi-classical limits for these values are presented in Table 1.1.[40]

TST-like models with or without tunneling correction, could, in several instances rationalize temperature-dependent KIEs,[43] assuming a rigid 1D potential surface, and large temperature independent KIEs for systems which showed no E_a for the isotopically sensitive step. However, these models fall short in explaining temperature independent small KIEs, with significant E_a for the isotopically sensitive step. One of the shortcomings of the Bell tunneling correction and similar TST-like models is that they exclusively focus on the hydrogen reaction coordinate and ignore the contributory motions of the heavy-atom environment. It is important to note that theoreticians have tried, somewhat successfully, to explain and predict KIEs using models that are in

essence based on the tunneling corrections to TST.[44] The few such examples include high-level hybrid QM/MM simulations of well-characterized model enzymes such alcohol dehydrogenase,[45-48] dihydrofolate reductase,[49] and thymidylate synthase,[50,51] among others.

1.3.6 Temperature dependence of KIEs as a probe for dynamics: Marcus-like models (full tunneling model)

During the past two decades, the simple Bell correction model proved to be insufficient in rationalizing data for several enzymatic systems (few such examples are presented in Table 1.2, however, this list is not meant to be exhaustive). As mentioned above, instances where KIEs greatly exceeded the semi-classical limit and where A_L/A_H surpassed unity (*e.g*. methylamine dehydrogenase and soybean lipooxygenase), or cases where systems exhibited non zero E_a for the H-transfer process with small temperature independent KIEs (*e.g.* DHFR, thymidylate synthase, alcohol dehydrogenase, etc.) required a new theoretical model to be developed. Such a model appeared under various names such as "vibrationally enhanced tunneling" model,[52] "environmentally coupled tunneling" model,[53] " protein promoting vibration" model,[54] and others. All of these models are based on Marcus' theory for the electron transfer, and therefore are commonly referred as Marcus-like models, as is the case in the following chapters,(*e.g*., Borgis and Hynes,[55,56] Kuznetzov and Ulstrup,[57] Scrutton,[52] Warshel,[58] Schwartz,[54] Klinman[39]) A common graphical representation of this model is given in Figure 1.6. This approach involves a Born-Oppernheim-like approximation which considers H-vibration to occur on a much faster timescale than the heavy atom motion in the solvent or in the protein. These motions are separately presented in Figure 1.6 as heavy-atom coordinate and hydrogen coordinate, which together constitute the reaction coordinate of the system. In these models, as the reaction proceeds, the heavy atom motions will bring the system to a

point, called tunneling ready state (TRS), where the potential surfaces for the reactant and product are degenerate, allowing the wavefunction of the transferred particle to spread from a donor well to an acceptor well without surmounting the intervening barrier. A general form of these models is given by the following equation:

$$k = C(\mathrm{T})e^{(\frac{\Delta G^\circ + \lambda)^2}{4\mathrm{RT}\lambda})} \int_{DAD_0}^{DAD_1} e^{F(m,DAD)} e^{E(DAD)/k_B \mathrm{T}} dDAD \qquad (12)$$

where C is an isotope-independent term, representing the fraction of reactive conformers in solution. The first exponential term is taken directly from Marcus's theory and is therefore referred as the "Marcus term", which is dependent on the reorganization energy (λ) and the driving force of the reaction (ΔG˚). The first integrated exponential, the "Franck-Condon" term is a nuclear overlap integral between the donor and acceptor states at a given donor acceptor distance (DAD). Therefore, it is an isotopically sensitive term. The second integrated term is a Boltzmann factor giving the probability of being at any particular DAD. These two exponents are integrated over all possible DADs to give the total tunneling probability. As evident from equation (12), at different temperatures heavy atom motions can affect the DAD distribution at TRS resulting in temperature dependent KIEs. The advantage of this model is that it was possible to explain temperature dependent rates and small temperature independent KIEs. Most mature wild type enzymes, like (WT *ec*DHFR), exhibit temperature independent KIEs, which indicate that heavy atom motions bring the system to an optimal TRS where DAD distribution does not change significantly over the experimental temperature range. Deviations from the physiological temperature and pressure, as well as certain site-specific mutations, can lead to temperature dependent KIEs (as it was studied in Chapters 3, 5 and 6).

In recent years, there have been modest attempts to model the temperature dependence of KIEs in enzymes using a form of Marcus-like model.[39] High-level QM/MM calculations have given some explanations of KIEs for soybean lipoxygenase,[59,60] alcohol dehydrogenase,[61,62] dihydrofolate reductase,[63,64] and

thymidylate synthase.[65] However, even lower level modeling has helped experimentalists to quantitatively link the experimental data to the potential energy surface describing the hydrogen coordinate (since the model represented in Equation (12) is a phenomological model).[48,66-68] However, due to the complexity of the DAD's potential surface, and the fact that the DAD's fluctuations do not constitute a normal mode, there are certain limitations, e.g. in determining a precise DAD and its fluctuations.[69] In addition, even though lower level modeling has helped experimentalists in understanding the KIEs in soybean lipoxygenase[70,71] and alcohol dehydrogenase,[72] in some cases these models required heavy parameterization in order to replicate experimental data. KIE data obtained for the mutants of residue 14, presented in Chapter 3, has been recently fitted to a form of Equation (12),[73] using a program available free of charge at http://chemmath.chem.uiowa.edu/webMathematica/kohen/marcuslikemodel.html. KIE data for both I14 mutants and F31V DHFR have been fitted using that program and presented in reference [73] and Chapter 5, respectively.

a

b

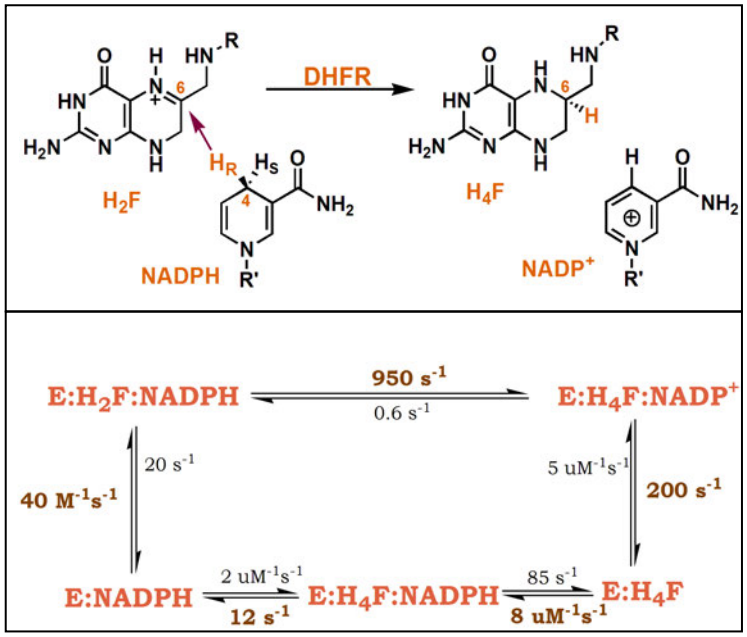

Figure 1.1 (a) Dihydrofolate reductase catalyzed reaction; R= *para*-aminobenzoyl polyglutamate moiety, R'= 2'-monophosphoadenosine-5'-diphosphoribose. (b) The catalytic cycle of *ec*DHFR. The five primary intermediates and the pH-independent rate constants at 25˚C are shown[6]; E = *ec*DHFR, H_2F = 7,8-dihydrofolate, H_4F = 5,6,7,8-tetrahydrofolate , NADPH = reduced nicotinamide adenine dinucleotide phosphate, $NADP^+$ = oxidized nicotinamide adenine dinucleotide phosphate.

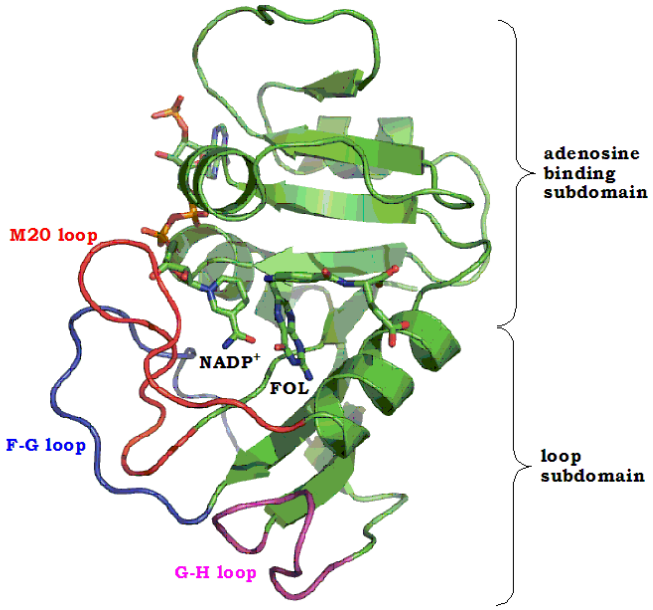

Figure 1.2 Structure of *ec*DHFR in a ternary complex with Folate and $NADP^+$ crystallized in $P2_12_12_1$space group (PDB ID 1RX2). The active cleft divides the protein into two subdomains: adenosine binding subdomain (residues 38-88) and the loop subdomain (major subdomain). Three flexible loops mentioned in the main text are: M20 (shown in red), F-G (shown in blue) and G-H loop (shown in mangenta). In this particular crystal structure, which is considered to represent the active Michaelis complex, the M20 loop is in the closed conformation.

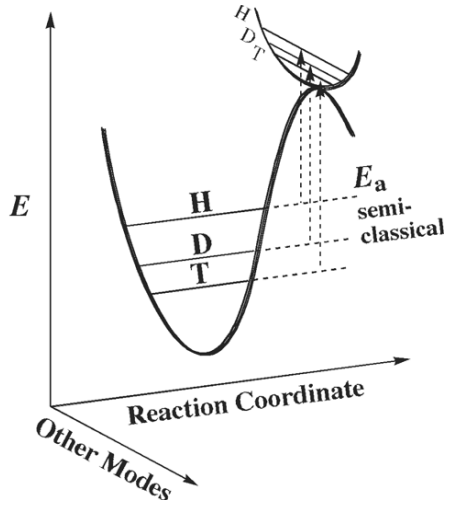

Figure 1.3 Graphical representation of the semi-classical model indicating that the difference in the energy of activation (ΔE_a) for H, D, and T, result from their different zero-point energies (ZPE) in the ground state (GS) and transition state (TS). The GS-ZPE is constituted by all degrees of freedom but mostly by the C-H stretching frequency and the TS-ZPE is constituted by all degrees of freedom orthogonal to the reaction coordinate. Reproduced from ref [42].

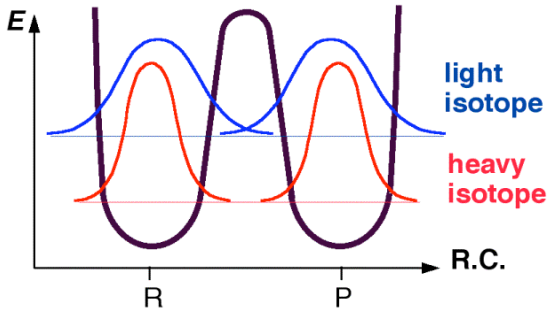

Figure 1.4 An example of the ground state tunneling along the reaction coordinate. The picture depicts the probability of a particle to tunnel, where the blue and red lines represent the probability functions for lighter and heavier isotopes, respectively. As noticeable from the figure, lighter isotope has a higher probability of tunneling than the heavier one. Reproduced from ref [74].

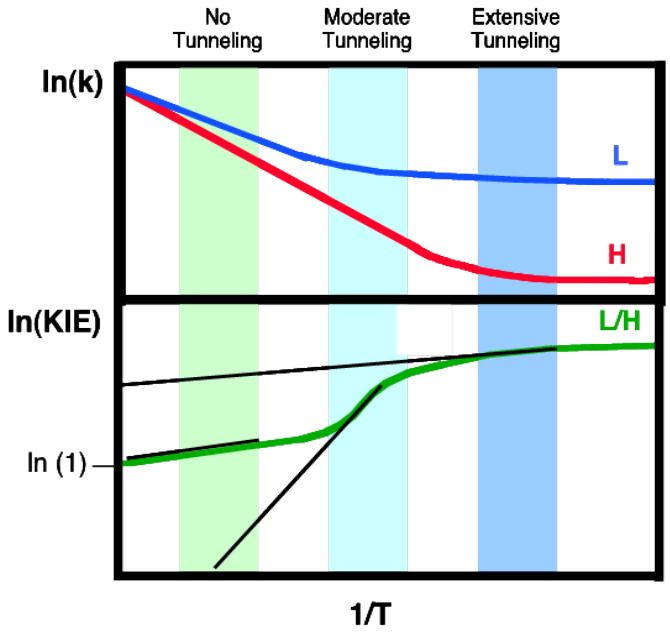

Figure 1.5 An Arrhenius plot of a H-transfer applicable for semi-classical models with tunneling correction. Top panel represents the Arrhenius plot of the reaction rates for two isotopes. Bottom panel represents the Arrhenius plot for their KIEs. The KIE on the Arrhenius preexponential factor is an intercept of the tangent to curve at different experimental temperatures. Highlighted regions indicate three distinct possibilities: I) No tunneling contribution; where A_L/A_H is close to unity and falls in the semi-classical limit; II) moderate tunneling contribution; results in A_L/A_H below the lower semi-classical limit; III) extensive tunneling contribution; where A_L/A_H is above the semi-classical limit; system exhibits very large intrinsic KIEs which are temperature independent. Reproduced from ref [74].

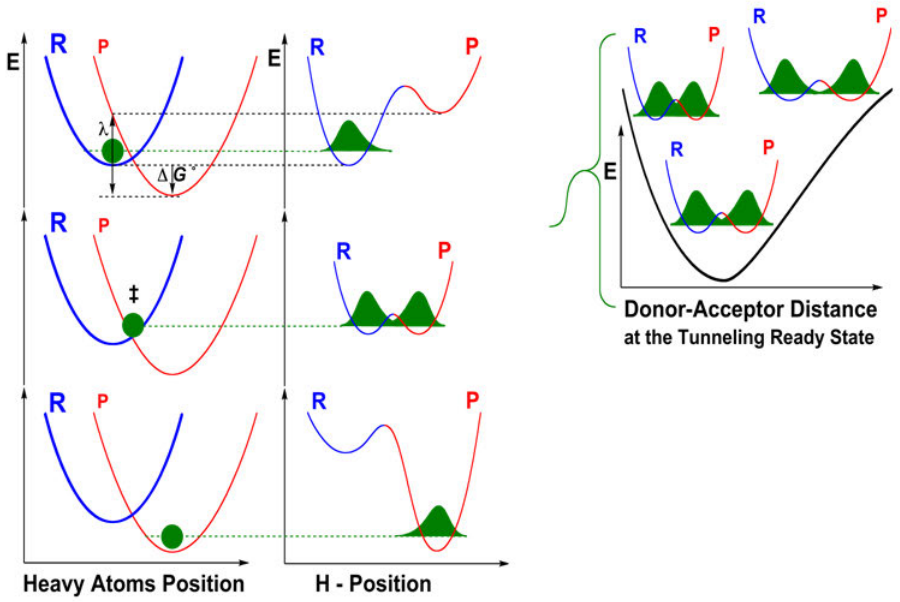

Figure 1.6 Graphical representation of a Marcus-like model. The heavy-atoms position coordinate represents the heavy-atom motions that modulate the average energies of reactant and product shown here as a double-well potential (in blue and red respectively). The heavy-atom motions will eventually bring the system to a degenerate state, TRS(‡), where tunneling is plausible. The H-position coordinate represents the double-well potential for the H-tunneling which is modulated by the heavy-atoms throughout the reaction. Tunneling probability of each isotope, at the TRS, is proportional to the overlap of the probability functions in the reactant and product states, which is dependable on the DAD. The range of the possible DADs at the TRS is determined by the heavy-atom motions, which depends on the Boltzmann distribution (as presented by the donor-acceptor distance coordinate). The thermal fluctuations of the DADs determine the temperature dependence of the KIEs for the H-transfer. This figure has been reproduced from ref [75].

Table 1.1 Semiclassical limits for the isotope effect on Arrhenius preexponential factors[29,43].

	A_H/A_T	A_H/A_D	A_D/A_T
Upper limit	1.7	1.4	1.2
Lower limit	0.3	0.5	0.7

Table 1.2 Enzymatic systems with properties outside the limits predicted by the "tunneling correction" models.

Enzyme	Type of transfer	Temperature dependence	k_H/k_D	A_H/A_D	Ref.
AADH	Proton	No	55	NR	[76]
MADH	Proton	No	16.8	13.3	[77]
TMADH	Proton	No	4.6	7.8	[78]
SRO	Proton	No	7.3	5.8	[79]
PTR	Hydride	No	~4.1	4.1	[80]
EAAL	H radical	ND	4.4-4.7	ND	[81]
GLM	H radical	ND	2.4	ND	[82]
SBL-1	H radical	Yes	81	18	[70]
SBL-1 mutants	H radical	Yes	93-112	4-0.12	[70]
Enzyme	**Type of transfer**	**Temperature dependence**	k_H/k_T	A_H/A_T	**Ref.**
DHFR	Hydride	No	6.1	7.4	[83]
G121V-M42W DHFR	Hydride	Yes	5.9	0.1	[84]
I14G DHFR	Hydride	Yes	6.1	0.024	[85]
R67 DHFR	Hydride	Yes	7.4	1.36	[86]
FDH	Hydride	No	5.9	6.1	[87]
TSase	Hydride	No	7.4 at 20˚C	6.8	[88]
TSase	Proton	Yes	6.2	$8.3*10^{-6}$	[89]
*bs*ADH above 30 ˚C	Hydride	No	5.6 at 30˚C	4.3	[90]

Table 1.2 Continued

*bs*ADH below 30 ˚C	Hydride	yes	5.6 at 30˚C	0.26	[90]

Note: For the enzymatic systems which exhibit temperature dependent KIEs, the values reported for the H/D or H/T KIEs, and their respective isotope effects on Arrhenius preexponential factors, were measured at 298K. (ND = not determined; NR= not reported in the publications) Abbreviations for the enzymes are: AADH: Aromatic amine dehydrogenase; MADH: Methylamine dehydrogenase; TMADH: Trimethylamine dehydrogenase; SRO: Sarcosine oxidase; PTR: Pentaerythritol tetranitrate reductase; EAAL: Ethanolamine ammonia lyase; GLM: Glutamate mutase; SBL-1: Soybean lipooxygenase; DHFR: Dihydrofolate reductase; FDH: Formate dehydrogenase; TSase: Thymidylate synthase; *bs*ADH: Alcohol dehydrogenase from *Bacillus stearothermophilus.*

CHAPTER 2.
SYNTHESIS OF RADIOLABELED NICOTINAMIDE COFACTORS FROM LABELED PYRIDINES: VERSATILE PROBES FOR ENZYME KINETICS[i]

2.1 Introduction

An enormous number of metabolic enzymes depend on the nicotinamide cofactors, *viz.* NAD^+, $NADP^+$, or their reduced forms, NADH and NADPH [91]. Chemical and isotopic modification of nicotinamide cofactors have enabled enzymological studies for several decades now (see refs.[92], [93], [94] and [95] for selected examples, and [96] for a comprehensive review of these cofactors). The development of new biophysical techniques drives the continued quest for novel nicotinamide derivatives prepared by rapid, cost-effective means.[97] When investigating enzymes that utilize one of these molecules as a redox cofactor, the fate of the labeled or modified cofactor may be followed to determine the mechanistic or kinetic course of the enzyme in question. While this can be achieved by a number of methods (*e.g.*, following the change in 340 nm absorbance of the reduced forms through out the reaction), radiolabeling offers higher sensitivity than most other techniques [98] and also facilitates the measurement of isotope effects.

Among the many uses of isotopically labeled nicotinamide cofactors is the measurement of kinetic isotope effects (KIEs)[ii] for H-transfer enzymatic reactions. This

---

[i] This chapter was published in the journal of Analytical Biochemistry [Sen, A., Stojković, V. and Kohen (2012), Synthesis of radiolabeled nicotinamide cofactors from labeled pyridines: versatile probes for enzyme kinetics, 430, pp123-129] (Sen and Stojković contributed equally to this work) Copyright 2012, Elsevier.

[ii] *Abbreviations used*: KIE, kinetic isotope effect; *Ec*DHFR, *Escherichia coli* dihydrofolate reductase; H_2F, dihydrofolate; H_4F, tetrahydrofolate; $^T(V/K)_{H,obs}$ and H/T_{obs}, observed tritium KIE; $^D(V/K)_{H,obs}$ and H/D_{obs}, observed deuterium KIE; H/T_{int}, intrinsic tritium

is exemplified below by KIE experiments with the *Escherichia coli* dihydrofolate reductase (*Ec*DHFR) enzyme. *Ec*DHFR is an extensively studied system and thus an excellent benchmark with which to test new nicotinamide labeling patterns. *Ec*DHFR uses NADPH as a hydride source in the reduction of 7,8-dihydrofolate (H_2F) to *S*-5,6,7,8-tetrahydrofolate (H_4F), transferring the pro-*R* hydrogen from C4 on the nicotinamide ring of NADPH to the *si*-face of C6 of the pteridine ring of H_2F (Figure 2.1). Several previous works have used NADPH labeled with deuterium (^2H) or tritium (^3H) at C4 to determine the KIE on the hydride transfer step for *Ec*DHFR and its mutants.[6,83,99-101] When such KIEs are measured competitively, both isotopologues are allowed to compete simultaneously for the enzyme. In these experiments the ratio of the reaction rates between the isotopologues is measured by following the fractionation of the isotopes at the product or the reactant, instead of determining the absolute rates.[29] For example, in competitive H/T and D/T KIE measurements [denoted also by $^T(V/K)_{H,obs}$ and $^T(V/K)_{D,obs}$, respectively] it is imperative that the non-radioactive isotopologues (^1H- or ^2H-labeled) are tracked by a radioactive labeling other than ^3H at a position on the NADPH molecule remote from the transferred hydrogen. This remote tracer (commonly ^{14}C) in the product thus represents the H (or ^2H) that has been transferred and so permits analytical examination of the ^3H depletion relative to H (or ^2H) in the product by following the $^3H/^{14}C$ ratio at different fractional conversions (as explained in detail in Materials and Methods). The same remote tracer can also be used to measure competitive H/D KIEs [denoted also by $^D(V/K)_{H,obs}$], where a remote ^3H label tracks one isotope (*e.g.*, ^2H) and a remote ^{14}C label identifies the other (*e.g.*, H). Consequently, in such experiments it is important that the remote tracer has no measurable effect on the reaction

---

KIE; H/D_{int}, intrinsic deuterium KIE; BIE, binding isotope effect; NADase, DPN nucleosidase/NAD^+ glycohydrolase; PMSF, phenylmethylsulfonate; *bm*GDH, *Bacillus megaterium* glucose dehydrogenase; *tb*ADH, *Thermoanaerobium brockii* alcohol dehydrogenase; DPM, disintegrations per minute.

rate, and no effect on the KIEs under study. If the labeling is too close to the reactive center, isotope effects due to the tracer isotope may lead to inflation or deflation of the KIEs being measured. As an extreme example, the use of [4-^{14}C]-NADPH as a labeled cofactor in the *Ec*DHFR reaction would add a primary (1˚, see below) ^{14}C KIE to the measured hydrogen KIE. While such an unwanted isotope effect would have a minor effect on 1˚ hydrogen KIEs (due to their large size), it could have a more detrimental impact on the much smaller secondary (2˚, see below) KIEs, or on KIEs of heavy isotopes.

Using such a remote-labeling dual-isotope method lends itself very well to a sequential HPLC/liquid scintillation counting (LSC) analysis, as demonstrated by a wealth of studies over the years.[20,102] For example, in the case of *Ec*DHFR, we previously performed competitive measurements of H/T KIEs using [Ad-^{14}C]-NADPH in competition with 4*R*-[4-^{3}H]-NADPH (see Figure 2.3 for radiolabeling details): here, the ^{14}C label on the adenine ring is far from the point of hydride transfer and cannot affect the rate of this step. The H/T KIEs are measured by simultaneously following the conversion of [Ad-^{14}C]-NADPH to [Ad-^{14}C]-NADP^{+}, and of 4*R*-[4-^{3}H]-NADPH to tritiated H_4F and its oxidized derivatives.[103] The measured values can be used together with D/T KIEs (measured in a similar fashion) to extract the intrinsic KIEs for the reaction, thus providing direct insight into the nature of the chemical step in the enzymatic reaction under consideration.[35,104]

The isotopic labeling pattern must be modified according to the type of KIE being measured – *i.e.*, either a 1° KIE, which results when the isotopic difference is in an atom directly involved in making or breaking bonds during the reaction, or a 2° KIE, which arises when the nature of the bonding to a labeled atom changes without formation or cleavage of bonds to that atom. Moreover, the labeling pattern should take into consideration whether H/T, D/T or H/D KIEs are being measured, as well as the interaction of the labeled nicotinamide cofactor with the enzyme. Indeed, the degree of

interaction between the remotely-labeled cofactor and the enzyme can be determined by the measurement of binding isotope effects (BIEs), which arise due to a difference in the binding constants of isotopologic reactants.[105] An inverse (<1) or normal (>1) BIE is indicative of differential binding constants for the labeled versus unlabeled cofactor. While binding effects are commonly determined by direct comparison of binding parameters (*e.g.* K_d), BIEs for enzymatic reactions can be sensitively measured by competitive KIE measurements of the labeled vs. the unlabeled cofactors as substrates (assuming that here KIEs represent the fractionation of the isotopes between the bound and the free state).[105] In other words, location of the isotopic labeling is such that measured V/K KIEs only represent the fractionation of the bound substrate since the labeling is on the adenine ring i.e., remote from the reaction site.

The [Ad-^{14}C]-NADPH cofactors used in the aforementioned studies were synthesized using the expensive (~$2,380/50 μCi) and periodically unavailable [Ad-^{14}C]-NAD^+ as the starting material, which significantly limits their use.[95] Here, we present the synthesis of [carbonyl-^{14}C]-NADPH, 4*R*-[carbonyl-^{14}C, 4-^{2}H]-NADPH and [carbonyl-^{14}C, 4-$^{2}H_2$]-NADPH from the less expensive (~$750/250 μCi) and readily available [carbonyl-^{14}C]-nicotinamide starting material. The synthesized cofactors have been examined as cost-effective alternatives to [Ad-^{14}C]-NADPH and its derivatives as reagents in KIE studies of enzymatic systems, with special emphasis on possible artifacts arising from the ^{14}C labeling at the amide position that might affect hydrogen KIEs of interest.

The remote location of the ^{14}C-label on the adenine ring in [Ad-^{14}C]-NADPH and other [Ad-^{14}C]-NAD^+ cofactors used previously is not likely to have any measurable effect on either binding or the chemistry of the aforementioned cofactors. The remoteness of the heavy-atom label from the reactive C4 hydrogen of the nicotinamide cofactor ensures no isotope effect due to the ^{14}C label on the rate of the H- or D- transfer being considered. However, in the case of the [carbonyl-^{14}C]-NADPH described here, the ^{14}C-

label is located at the amide carbonyl, γ to the reactive C4 hydrogen. This proximity to the reactive center gives rise to the question: does labeling the amide carbonyl (rather than the adenine ring) with ^{14}C lead to a significant isotope effect on H-transfer reactions occurring at the C4 position? In other words, is there a measurable isotope effect when [carbonyl-^{14}C]-NADPH is used instead of [Ad-^{14}C]-NADPH?

Since direct measurement of the isotope effect between [carbonyl-^{14}C]-NADPH and [Ad-^{14}C]-NADPH is not practical, we first measured the BIE at the adenine ring on the *Ec*DHFR reaction, using [Ad-^{3}H]-NADPH and [Ad-^{14}C]-NADPH, and then the KIE between [Ad-^{3}H]-NADPH and [carbonyl-^{14}C]-NADPH. Since [Ad-^{3}H]-NADPH is a common reference between the BIE and KIE experiments, the ratio between the measured BIE to the KIE allowed us to establish the γ-2° ^{14}C KIE of interest. In other words, since it is not possible to directly compare the reaction rate of the [carbonyl ^{14}C]-NADPH to that using unlabeled NADPH or [Ad-^{14}C]-NADPH, we have instead used multiple KIE and BIE measurements to compare the rates of [Ad-^{14}C]-NADPH to that of [carbonyl-^{14}C]-NADPH using [Ad^{-3}H]-NADPH as a common reference. The measured value after standard error propagation is 1.003 ± 0.004 for the γ-2° ^{14}C KIE, which suggests that [carbonyl-^{14}C]-NADPH and its derivatives are viable substitutes for [Ad-^{14}C]-NADPH and other labeled cofactors synthesized in the past from [Ad-^{14}C]-NAD^+.

2.2 Materials and Methods

2.2.1 Materials

All reagents were purchased from Sigma-Aldrich, unless otherwise noted. $NADP^+$- dependent glucose dehydrogenase from *Bacillus megaterium* (*bm*GDH, 218 units/mg solid) was purchased from USB-Affymetrix, while NAD^+/$NADP^+$-dependent nucleosidase (NADase) from porcine brain (≥ 0.007 un/mg solid) was purchased from Sigma-Aldrich. *Ec*DHFR was expressed and purified according to the procedure of

Cameron *et al.*[106] [carbonyl-^{14}C]-nicotinamide (55 mCi/mmol, 100 μCi/ml) was obtained from Moravek, [Ad-^{14}C]-NAD^+ (>220 mCi/mmol, 25 μCi/ml) and nicotinamide-[2,5',8-^{3}H]-adenine nucleotide ([Ad-^{3}H]-NAD^+, 24 Ci/mmol, 0.1 mCi/ml) were from Amersham (now available from Perkin-Elmer). H_2F was synthesized from folic acid by the method of Blakley [107]. [1-^{2}H]-glucose was synthesized with > 99.9% deuteration (as characterized by ^{1}H-NMR) by reduction of δ-gluconolactone with sodium amalgam in 99.96% D_2O.[108]

2.2.2 Analytical methods

All analytical separations were made by HPLC on a Beckman-Coulter System Gold instrument (model 126), using a Supelco Discovery C-18 column (250 x 4.6 mm i.d., 5 μm particle size) and the gradient elution method described in Table 2.1, but with an altered flow-rate of 0.8 ml/min suited for use with the analytical HPLC column. Eluted peaks were analyzed using an online Beckman UV-Vis detector (model 168) and a Packard 500TR Series flow scintillation detector. $NADP^+$ synthesized in the first step (Figure 2.2) was isolated in a single broad peak at ~ 12 min using a Supelco Discovery semipreparative C-18 column (250 x 10 mm i.d., 5 μm particle size) following the elution gradient shown in Table 2.1; a representative elution profile is depicted in Figure 2.4A. The semipreparative HPLC method described previously [109] was used to purify the final NADPH product, and radioactive product yields were quantified using a Packard TriCarb 2900 TR liquid scintillation counter.

2.2.3 Preparation of porcine brain NADase

Prior to the synthesis of the radiolabeled cofactor, NADase solutions were prepared in 0.1 M KH_2PO_4 buffer (pH 7.5) using a modified version of the procedure described by Hixson *et al.*[92] In short, 1 g of lyophilized NADase (~7 units) was dissolved

in 0.1 M KH_2PO_4 buffer (pH 7.5) to a final concentration of 0.5 units/ml. The buffered solution was sonicated for 45 min at 4 °C in the dark, then 6 mg of trypsin (≥10,000 units/mg) was added and the reaction mixture was incubated at 37 °C for 40 min. 3.6 mmol of phenylmethylsulfonate (PMSF) was then added, and incubation continued for an additional 5 min at 37 °C. The reaction mixture was centrifuged at 4 °C and 4000 to 5000 x *g* to remove insoluble debris. The supernatant was removed and stored at 4 °C in the dark until used. Under these conditions, NADase solution was found to be stable for at least 2 months. Prior to every synthesis, an aliquot of NADase solution corresponding to 0.175 units was spun down at 10,000 x *g* to remove any denatured or precipitated protein that may have accumulated during storage.

2.2.4 Synthesis of [carbonyl-^{14}C]-NADPH

Figure 2.2 illustrates the general synthetic strategy employed for the preparation of [carbonyl-^{14}C]-NADPH in two steps: first, the exchange reaction of $NADP^+$ and [carbonyl-^{14}C]-nicotinamide to yield [carbonyl-^{14}C]-$NADP^+$, and the subsequent reduction with *bm*GDH and glucose to yield [carbony-^{14}C]-NADPH.

Synthesis of [carbonyl-^{14}C]-$NADP^+$ (Figure 2.2, first step): 125 μL of the ethanolic solution of [carbonyl-^{14}C]-nicotinamide (12.5 μCi, 227 nmol) was blown to dryness with N_2 or Ar gas, and combined with 0.175 units NADase, 2.3 μmol $NADP^+$ and 0.1 M KH_2PO_4 (pH 7.5) buffer to a final volume of 400 μL. The reaction was allowed to proceed at 35 °C in the dark for 60 min. Reaction progress was periodically monitored by HPLC/flow scintillation detector analysis. It is important to note that, since NADase catalyzes the reversible hydrolysis of $NADP^+$ to nicotinamide and 2'-monophosphoadenosine-5'-diphosphoribose, the reaction mixture for the first step should contain a 10:1 excess of $NADP^+$ over [carbonyl-^{14}C]-nicotinamide. Different ratios lead

to lower yields or lower specific radioactivities of the radiolabeled $NADP^+$ (see discussion). It is also noteworthy that in the synthesis of radiolabeled material, the yield is measured in terms of the radiolabeled starting material ([carbonyl-^{14}C]-nicotinamide in this case), which is the limiting-reagent in the synthesis.

After completion of the exchange reaction (generally after 30 min), NADase was removed from the reaction mixture by filtration through an Amicon Ultra Ultracel-10K (10,000 MWCO) regenerated cellulose centrifugal filter. LSC analysis of the filtrate indicated minimal loss of radioactivity due to filtration. [carbonyl-^{14}C]-$NADP^+$ was then isolated from the filtrate by semipreparative HPLC purification as described in the Methods section, and lyophilized overnight to remove all traces of solvent. The lyophilized $NADP^+$ was stable at -80 °C for at least a year. Before continuing with further synthetic steps, it was critical that the large amounts of salt (the result of lyophilization) be removed, as high salt concentrations can inhibit certain enzymatic reactions. Therefore, lyophilized [carbonyl-^{14}C]-$NADP^+$ was dissolved in 1 ml of doubly de-ionized (DDI) H_2O and loaded onto a 3 ml Sephadex C-18 desalting column. The loaded column was washed through with 3 ml DDI H_2O, and [carbonyl-^{14}C] $NADP^+$ was then eluted using 3 ml of 15% MeOH/2.5 mM KH_2PO_4 buffer. This solution was lyophilized overnight.

Synthesis of [carbonyl-^{14}C]-NADPH (Figure 2.2, second step): The lyophilized [carbonyl-^{14}C]-$NADP^+$ was re-suspended in 450 μl 0.1 M KH_2PO_4 (pH 7.5) buffer immediately before its reduction to [carbonyl-^{14}C]-NADPH. 1.25 μmol D-glucose and 1 mg (~218 units) *bm*GDH were added to the [carbonyl-^{14}C]-$NADP^+$ solution and the pH was adjusted to 8.0 at 37 °C, with a final volume of 500 μl. The reaction was allowed to proceed at 37 °C for 1 hour, when HPLC/flow scintillation analysis showed >99% conversion of [carbonyl-^{14}C]-$NADP^+$ to [carbonyl-^{14}C]-NADPH (Figure 2.5). Upon completion of the reaction, the reaction mixture was centrifuged at room temperature and

13,000 x *g* for 5 min, and the products were purified by semipreparative HPLC as described in the Methods section. The purified [carbonyl-^{14}C]-NADPH was quantified by LSC analysis, and divided into 3 million DPM aliquots. These aliquots were immediately lyophilized and stored in the dark at -80 ˚C. Previously published data indicates that NADPH stored under these conditions remains viable for more than 24 months [109]. After purification and lyophilization, the NADPH product was found to be more than 99.5% pure by HPLC/radiographic flow-scintillation analysis (Figure 2.5).

2.2.5 Synthesis of 4R-[carbonyl-^{14}C,4-^{2}H]-NADPH from [carbonyl-^{14}C]-NADP^{+}

4*R*-[carbonyl-^{14}C, 4-^{2}H]-NADPH was synthesized from [carbonyl-^{14}C]-NADP^{+} using the one-step reaction catalyzed by *Thermoanaerobium brockii* alcohol dehydrogenase (*tb*ADH).[110] The final product was purified, characterized and stored in the same manner as [carbonyl-^{14}C]-NADPH described in the previous section.

2.2.6 Synthesis of [carbonyl-^{14}C,4-^{2}H$_2$]-NADPH from [carbonyl-^{14}C]-NADP^{+}

[carbonyl-^{14}C, 4-^{2}H$_2$]-NADPH was synthesized from [carbonyl-^{14}C]-NADP^{+} following the 3-step procedure involving *bm*GDH, *tb*ADH and 1-^{2}H-glucose as described in refs. [111] and [103]. Purification, characterization and storage were the same as for [carbonyl-^{14}C]-NADPH.

2.2.7 Determination of 1° H/T and D/T KIEs for EcDHFR using synthesized [carbonyl-^{14}C] derivatives

For the measurement of H/T KIEs, 4*R*-[4-^{3}H]-NADPH was prepared according to previously published procedure,[112] and co-purified in a 6:1 ratio with [carbonyl-^{14}C]-NADPH to compensate for the lower efficiency in LSC counting of tritium.[109] For the measurement of D/T KIEs, 4*R*-[4-^{3}H]-NADPH was co-purified in a 6:1 ratio with 4*R*-[carbonyl-^{14}C, 4-^{2}H]-NADPH. The co-purified materials in both cases were divided into 300,000 DPM aliquots (of ^{14}C) and frozen at -80 °C for short-term storage (up to 15 days). KIE experiments were performed according to the procedure used by Wang *et a*l.[103] in 1X MTEN buffer (100 mM NaCl, 50 mM MES, 25 mM Tris and 25 mM ethanolamine, pH 9.0 at 25 °C). As per the previous procedure, *Ec*DHFR was allowed to react with co-purified NADPH and H_2F (final concentration of 0.85 mM) at 25 °C in 1X MTEN (pH 9.0), and aliquots were removed from the reaction mixture and quenched with methotrexate to yield samples with fractional conversions (f ; determined from the ratio of ^{14}C in the product to the total amount of ^{14}C in products and reactants) ranging from 20-80%. Observed KIEs were calculated using the following equation:[29]

$$KIE_{obs} = \frac{\ln(1-f)}{\ln(1-f*\frac{R_t}{R_\infty})} \qquad (1)$$

where R_t and R_∞ are ratios of ^{3}H to ^{14}C in the products at various fractional conversions and at 100% conversion, respectively. Intrinsic H/T KIEs were calculated using the Northrop method, as elaborated upon in previous publications [103] and [83]. All KIE results are displayed in Table 2.2.

2.2.8 Measurement of γ - 2° ^{14}C KIE due to ^{14}C isotopic labeling at the amide carbonyl of NADPH

[Ad-^{3}H]-NADPH and [carbonyl-^{14}C]-NADPH for KIE measurement, and [Ad-^{3}H]-NADPH and [Ad-^{14}C]-NADPH for the BIE measurement, were combined and co-purified in a DPM ratio of 5:1 (^{3}H/^{14}C). These two mixtures were used in the kinetic measurements following the same procedure as described for 1˚ KIEs above. As mentioned in the introduction, while the experimental procedure is the same for BIE and KIE experiments, the value calculated in the BIE measurement using equation 1 corresponds to a BIE, while KIE obtained by [Ad-^{3}H]-NADPH and [carbonyl-^{14}C]-NADPH reflects the product of the BIE and the γ - 2° ^{14}C KIE of interest. Dividing the second by the first yields a value indicative of the carbonyl γ - 2° ^{14}C KIE.

2.3 Results and Discussion

2.3.1 Synthesis of [carbonyl-^{14}C]-NADPH, 4R- [carbonyl-^{14}C, 4-^{2}H]-NADPH and [carbonyl-^{14}C, 4-^{2}H$_2$]-NADPH

NADase catalyzes the conversion of NAD(P)$^+$ to nicotinamide and 2'-monophosphoadenosine-5'-diphosphoribose. The hydrolysis is reversible in both cases, and the reaction equilibrium is governed by the ratio of NAD(P$^+$) to free nicotinamide, and the amount of ADP-ribose or 2'-monophosphoadenosine-5'-diphosphoribose in solution. It was found that the reaction could be optimized for minimal reaction times (< 1 hour) and maximal yields of radioactive cofactor by using a 10:1 ratio of NADP$^+$ to [carbonyl-^{14}C]-nicotinamide in the initial reaction mixture. Deviations from this ratio produced deleterious effects on the time required for maximal yield, and the yield itself. Moreover, dissimilar ratios resulted in different specific radioactivities in the product, and in some cases led to the formation of large amounts of unidentified by-products (as determined by HPLC analysis). For example, a lower ratio (3:1) of NADP$^+$ to labeled

nicotinamide required longer reaction times and resulted in maximum yields of 37% after 1 hour, while ratios higher than 10:1 led to final products with low specific radioactivity, thus limiting their use in KIE experiments. When a ratio of 10:1 was used, yields reached a maximum value of 70-75% (measured as the percentage of total radioactivity in the desired product) after ~30 minutes (Figure 2.4B). It is important to establish a point at which the amount of formed product is at its maximum, as a slow steady decline occurs at longer reaction times. This decline could be result of several different processes, and not simply a reverse reaction catalyzed by NADase (as this is an equilibrium reaction). Moreover, we observed a small amount of unidentified by-product (max ~1.6% of total radioactivity; Figure 2.4B) that was easily separated from the $NADP^+$, and therefore did not present a major obstacle in either total yield or purity of the product. Since a 10:1 ratio produced satisfactory yields of [carbonyl-^{14}C]-$NADP^+$, the reaction was not further optimized. However, if lower specific radioactivities are acceptable in the product, it is possible to obtain up to 90% yields in 1 hr using higher ratios of $NADP^+$/nicotinamide. The relatively low price of the radioactive [carbonyl-^{14}C]-nicotinamide starting material was also a factor in the experimental design described above. Since the cost of this starting material is the major contributor to the overall cost of each synthesis, the price difference makes the [carbonyl-^{14}C]-nicotinamide more appealing as a reagent.

The [carbonyl-^{14}C]-$NADP^+$ produced must be separated from the reaction mixture that also contains [carbonyl-^{14}C]-nicotinamide and 2'-monophosphoadenosine-5'-diphosphoribose. Otherwise, it is possible that subsequent kinetic experiments with the final [carbonyl-^{14}C]-NADPH product will show artifacts due to nicotinamide contamination. In addition, 2'-monophosphoadenosine-5'-diphosphoribose has been shown to inhibit certain $NADP^+$-dependent dehydrogenases, including GDH.[113] This makes isolating the [carbonyl-^{14}C]-$NADP^+$ from the exchange reaction mixture crucial for successful downstream steps. A previously published method for the purification of NADPH [95] was found to be inefficient in separating $NADP^+$ from nicotinamide.

Therefore, that method was modified by reducing the percentage of methanol from 15 to 7.5% during the isocratic elution that starts at 11 min, consequently increasing separation between $NADP^+$ and nicotinamide peaks to 8 min. Thus, in the modified method, $NADP^+$ elutes at 12.5 min, and nicotinamide at 20.5 min. The [carbonyl-^{14}C] $NADP^+$ elutes in a broad peak over 5 min, as depicted in Figure 2.4, and is collected in at least 6 ml of 7.5% MeOH /0.1 M KH_2PO_4 solution. Further reduction in the methanol percentage caused significant peak broadening that rendered greater separation in retention times meaningless.

The lyophilized product from the first exchange step contains [carbonyl-^{14}C]-$NADP^+$ as well as significant amounts of KH_2PO_4. When this solid was simply resuspended in 500 μl water (to a final concentration of ~ 1.2 M KH_2PO_4) and used for the subsequent GDH reaction, a dramatic decrease in the rate of the reduction to NADPH was observed (80% of the $NADP^+$ still remained unreacted at 1 hour, in contrast to the 99% conversion to NADPH usually seen at 37 °C and pH 7.0 for the same reaction in the presence of 0.1 M KH_2PO_4). We hypothesized that this was due to the high salt concentration in the resuspension solution, which was either causing active GDH to precipitate out of the solution (a 'salting out' effect) or directly inhibiting the GDH reaction. To test this hypothesis, we used a Sephadex 1 ml C-18 column to remove the excess salt from the lyophilized product, and [carbonyl-^{14}C]-$NADP^+$ was eluted from the column using a 15% MeOH/2.5 mM KH_2PO_4 (pH 6.0) solution. The losses in yield due to the addition of this step were minor (<2%). Addition of this step restored the reaction rate of subsequent GDH-catalyzed reductions, providing support to the above hypothesis.

Our procedure describes the reduction of [carbonyl-^{14}C]-$NADP^+$ to [carbonyl-^{14}C]-NADPH, 4*R*-[carbonyl-^{14}C, 4-^{2}H]-NADPH, or [carbonyl-^{14}C, 4-$^{2}H_2$]-NADPH. If desired, 4*S*-[carbonyl-^{14}C-4-^{2}H] NADPH could be produced by simply truncating the procedure and reducing [carbonyl-^{14}C]-$NADP^+$ with [1-^{2}H]-glucose and GDH. Also, since NADase can accept both NAD^+ and $NADP^+$ as substrates, experimental procedures

similar to the ones described here can be envisioned for the preparation of [carbonyl-^{14}C]-NAD^{+}/NADH and their deuterated derivatives for kinetic and mechanistic studies of NAD(H) specific enzymes.

2.3.2 ^{14}C-labeling at the nicotinamide carbonyl carbon of NADPH does not result in a significant γ -2° ^{14}C KIE

Due to the location of the new label near the reaction center, more specifically at the amide carbonyl of NADPH, the possible issue of a γ-2˚ KIE artifact on hydride transfer KIEs to be measured using this compound had to be addressed. To examine the extent of that effect on cofactor oxidation, we designed experiments using [Ad-^{3}H]-NADPH in competition with either [Ad-^{14}C]-NADPH or [carbonyl-^{14}C]-NADPH as substrates of the *Ec*DHFR catalyzed reaction. The first combination ([Ad-^{14}C]-NADPH/[Ad-^{3}H]-NADPH) resulted in a BIE on the adenine ring of 1.002 ± 0.002 and the second ([carbonyl-^{14}C]-NADPH/[Ad-^{3}H]-NADPH) in a mixed KIE of 1.005 ± 0.002. The ratio of these values yield a γ-2˚ ^{14}C KIE ([carbonyl-^{14}C]-NADPH/[Ad-^{14}C]-NADPH) of 1.003 ± 0.004. This value is practically unity (no KIE) as the errors usually obtained on either 1˚ and even 2˚ hydrogen KIEs are larger than 0.01. When measuring small KIEs (e.g. 2˚ KIEs) with other enzymes than *Ec*DHFR, or when using other carbonyl-labeled nicotinamide cofactors, we recommend that researchers test for such possible artifacts for their specific system.

2.3.3 Testing the viability of synthesized materials using KIEs: Comparison of intrinsic KIEs measured using [carbonyl-^{14}C]-NADPH vs. [Ad-^{14}C]-NADPH

To validate the use of the new [carbonyl-^{14}C]-NADPH and its deuterated derivatives in kinetic experiments, we have compared the outcome of KIE experiments

that used the new synthesized materials, to previous KIE measurements that utilized adenine labeled cofactors as substrates of *Ec*DHFR. We conducted 1˚ H/T experiments using [carbonyl-^{14}C]-NADPH and 4*R*-^{3}H-NADPH as substrates, and 1˚ D/T KIEs using 4*R*-[carbonyl-^{14}C, 4-^{2}H]-NADPH and 4*R*-^{3}H-NADPH as substrates, for the *Ec*DHFR reaction. All experiments were performed at 25 °C and pH 9.0. The results, along with the calculated intrinsic KIEs, are compared to previously published values in Table 2.2. All previous measurements were done using [Ad-^{14}C]-NADPH and its deuterated analogs as substrates. The close agreement between our measured and intrinsic values and all prior results indicates that with this enzyme the [carbonyl-^{14}C]-NADPH materials are excellent substitutes for the [Ad-^{14}C]-NADPH materials in KIE experiments.

2.3.4 Comparison of cost, effort, and yield of [Ad-^{14}C]-NADPH [95] vs. [carbonyl-^{14}C]-NADPH syntheses.

The new synthesis of [carbonyl-^{14}C]-NADPH presented here is advantageous because: (i) the [carbonyl-^{14}C]-nicotinamide precursor is substantially cheaper starting material than the commercially available [Ad-^{14}C]-NAD^{+} precursor used to make [Ad-^{14}C]-NADPH (by a factor of >12 based on $/Ci and synthetic yields); (ii) the new synthesis is much faster (e.g., 30 min glycosidic exchange vs. 3 hours 2'-phosphorilation); (iii) it requires fewer enzymes and reagents (e.g., ~ U.S. $1 NADase vs. ~ U.S. $70 NAD-kinase and phosphocreatine kinase); and (iv) has better yield than that of [Ad-^{14}C]-NADPH (i.e., 60-75% vs. 40-60%). In summary, the new synthetic procedure is a cost- and effort-effective alternative to previously published procedures".

2.4 Conclusion

The development of a new labeling pattern for ^{14}C-labled nicotinamide cofactors is presented along with some applications and the examination of possible experimental

artifacts. We have shown that [carbonyl-^{14}C]-NADP^{+}, [carbonyl-^{14}C]-NADPH, 4*R*-[carbonyl-^{14}C, 4-^{2}H]-NADPH and [carbonyl-^{14}C, 4-^{2}H$_2$]-NADPH can be synthesized quickly, in reasonable yields, and at relatively low costs, using a simple chemoenzymatic procedure. We have utilized [carbonyl-^{14}C]-NADPH to demonstrate that NADPH labeled with ^{14}C at the nicotinamide carbonyl has no significant effects on the hydrogen KIEs measured using those isotopologues as substrates in the *Ec*DHFR reaction. 1° H/T and D/T KIEs measured using the newly synthesized materials are in complete agreement with KIEs previously measured with NADPH labeled at the adenine ring, and confirm the utility of this material. Finally, the synthesized material can easily be adapted for use in kinetic experiments with other NADP^{+}/NADPH/NAD^{+}/NADH-dependent enzymes, and as these are ubiquitous in nature the synthetic methods described herein could potentially be of broad utility.

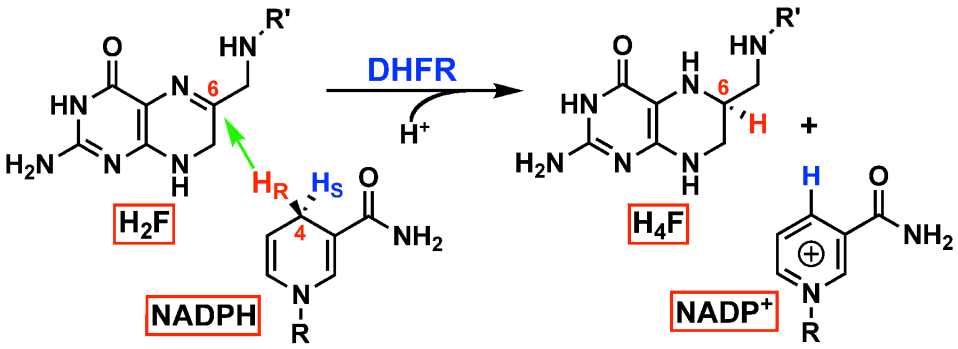

Figure 2.1 The reaction catalyzed by DHFR. R = adenine dinucleotide 2' phosphate and R' = (p-aminobenzoyl) glutamate.

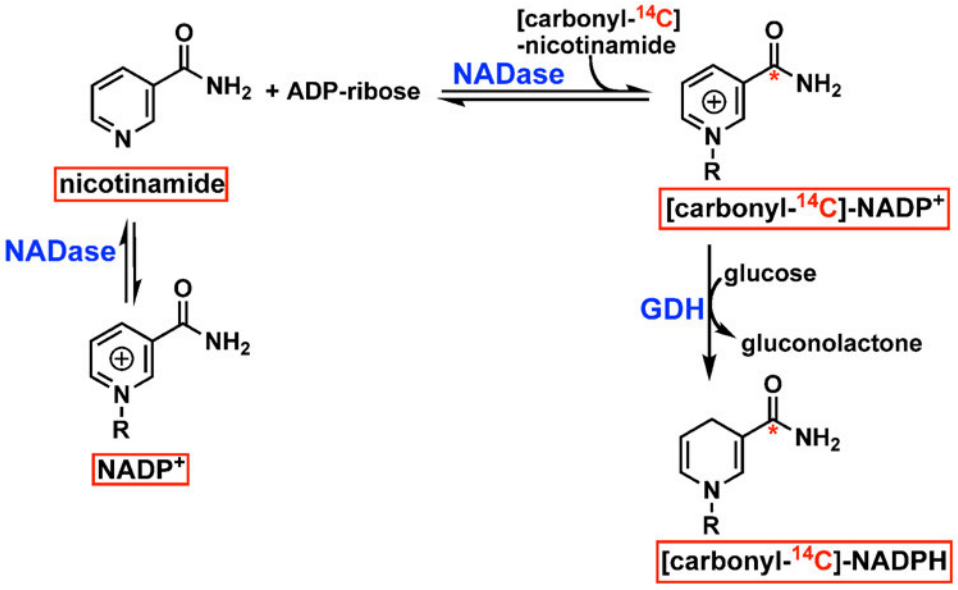

Figure 2.2 Synthesis of [carbonyl-^{14}C]-NADPH from [carbonyl-^{14}C]-nicotinamide. R = 2'- monophosphoadenosine-5'-diphosphate ribose, where the asterisks denote the position of the ^{14}C-label.

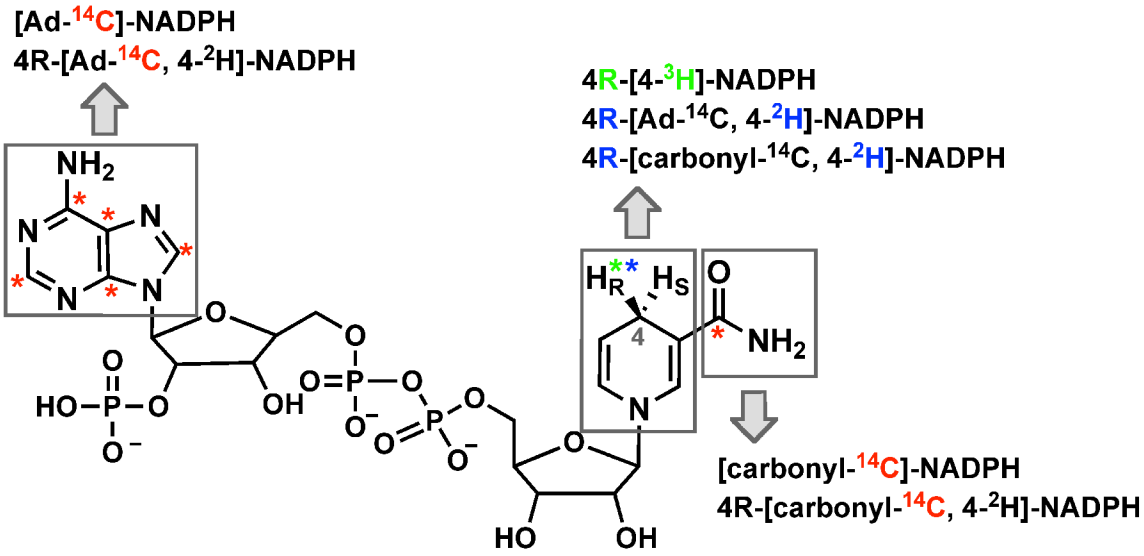

Figure 2.3 Labeled NADPH derivatives. Asterixes indicate the position of isotopic labeling with ^{14}C (red), ^{2}H (blue) or ^{3}H (green). H_R=^{1}H for NADPH, [Ad-^{14}C]-NADPH and [carbonyl-^{14}C]-NADPH; H_R=^{2}H for 4*R*-[Ad-^{14}C, 4-^{2}H]-NADPH and 4*R*-[carbonyl-^{14}C, 4-^{2}H]-NADPH; H_R=^{3}H for 4*R*-[4-^{3}H]-NADPH. For the sake of clarity, ^{3}H-labeling on [Ad-^{3}H]-NADPH and its derivatives is not shown.

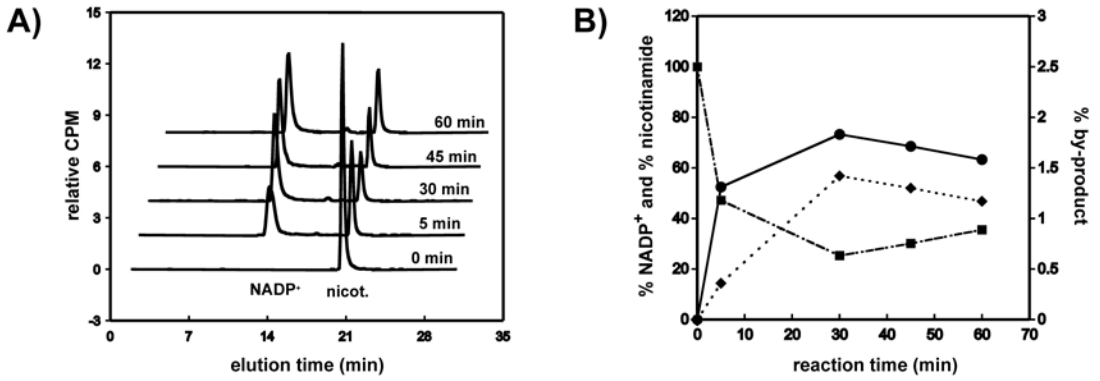

Figure 2.4 Summary of the results for the first synthetic step - synthesis of [carbonyl-^{14}C]-NADP^{+}. A) Reverse-phase HPLC-flow radiogram of the reaction mixture at different time points. The main peaks correspond to [carbonyl-^{14}C]-NADP^{+}, ~12.5 min, and [carbonyl-^{14}C] nicotinamide, ~20.5 min. The middle peak represents an unidentified by-product, which accounts for <1.6% of total radioactivity, and was easily separated from the NADP^{+}. B) Percent of each compound (from panel A) during the course of 60 min reaction, where [carbonyl-^{14}C]-NADP^{+} is presented by closed circles, [carbonyl-^{14}C]-nicotinamide by squares, and the ^{14}C-labeled by-product by diamonds.

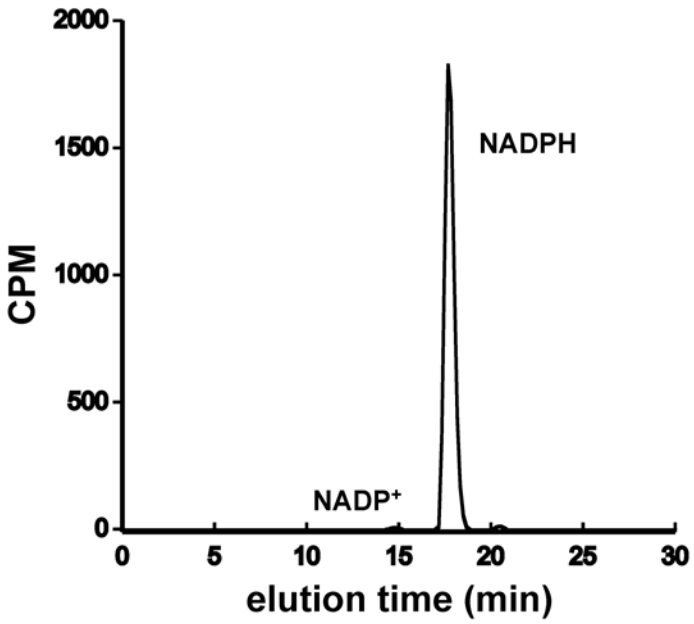

Figure 2.5 Reverse-phase HPLC-flow radiogram of the reaction mixture after the [carbonyl-^{14}C]-$NADP^+$ reduction. Radiogram indicates a complete conversion (>99.5%) of $NADP^+$ to NADPH.

Table 2.1 Semi-preparative HPLC method using reverse-phase C-18 column and gradient elution.

Time (min)	% solvent A	% solvent B	Flow rate (ml/min)
0	100	0	3.2
11	100	0	3.2
11.10	92.5	7.5	3.2
21	92.5	7.5	3.2
21.10	50	50	3.2
23	50	50	3.2
23.10	0	100	3.2
30	0	100	3.2

Note: Solvent A is 0.2 M NaCl/1 mM Tris-HCl (pH 8.2) and solvent B is MeOH.

Table 2.2 Observed and intrinsic 1° KIEs measured using [carbonyl-^{14}C]-NADPH and 4*R*-[4-^{3}H]-NADPH (for H/T experiments) and 4*R*-[carbonyl-^{14}C, 4-^{2}H]-NADPH with 4*R*-[4-^{3}H]-NADPH (for D/T experiments).

^{14}C-labeling pattern	H/T_{obs}	D/T_{obs}	H/T_{int}	D/T_{int}	H/D_{int}
[carbonyl-^{14}C]	4.86 ± 0.06	1.66 ± 0.01	6.13 ± 0.18	1.72 ± 0.02	3.56 ± 0.07
[Ad-^{14}C][a]	4.85 ± 0.09	1.66 ± 0.03	6.10 ± 0.42	1.72 ± 0.04	3.55 ± 0.17

[a] Ref. [83].

Note: The results are compared to previously published values obtained using [Ad-^{14}C] NADPH and [Ad-^{14}C, 4-$^{2}H_2$] NADPH (with 4*R*-[4-^{3}H]-NADPH and 4*S*-[4,4-^{3}H,^{2}H]-NADPH, respectively). [95]

CHAPTER 3.
EFFECTS OF THE DONOR ACCEPTOR DISTANCE AND DYNAMICS ON HYDRIDE TUNNELING IN THE DIHYDROFOLATE REDUCTASE CATALYZED REACTION[iii]

3.1 Introduction

Despite intense studies during the past century, many questions regarding enzyme catalysis still remain unanswered. Specifically, the physical features of enzyme catalyzed reactions continue to be part of a vigorous debate. The transition state (TS) approach introduced by Pauling,[114] which suggested that enzymes work by preferentially binding the activated form of the substrate(s) at the TS, still remains the generally accepted description. This static view of enzyme catalysis is likely to be correct; however it fails to address the mechanism by which physical features that contribute to that TS stabilization (e.g., electrostatics and steric effects) arise along the reaction coordinate. An approach that provides a more dynamic view of the catalytic process suggests that the thermal motions of both enzyme and substrates are essential for the chemical transformations catalyzed by an enzyme. A large amount of experimental and theoretical evidence supports such a view for certain enzymes, however the relationship between enzyme dynamics[115] and bond activation needs further description. Analogous issues are of equal importance in solution reactions, and here we take advantage of the ability to control the reactants' relative orientation in an enzyme's active site to examine the nature of C-H→C transfer reactions in general. Several experimental and theoretical approaches provide an

[iii] This chapter was published in the Journal of American Chemical Society [Stojković, V., Perissinoti, L.L., Willmer, D., Benkovic, S.J. and Kohen, A. (2012), Effects of the donor acceptor distance and dynamics on hydride tunneling in the dihydrofolate reductase catalyzed reaction, 134, pp1738-1745]. Copyright 2012, American Chemical Society.

examination of hydrogen tunneling and its environmental coupling.[39,58,66,74,116-123] Here, we focus on the temperature dependence of the intrinsic kinetic isotope effect (KIE), and on single turnover rates, as a means to probe the nature of the hydride transfer.[39,74,124,125]

Experimental data collected by this approach led to the development of several phenomenological working models, which are extensions of the Marcus theory for electron transfer.[118,126,127] They are referred to as Marcus-like models (also addressed in literature as environmentally coupled tunneling,[128] rate-promoting vibrations,[129] vibrationally enhanced tunneling,[52] and more. In these models, illustrated in Figure 3.1, heavy-atom motions along the reorganization coordinate bring the system to a point where donor and acceptor wells are degenerate and where tunneling of the hydride is possible (i.e., a tunneling ready state, TRS). Thus, environmental reorganization occurs before hydride transfer takes place.[39,58,62,72,74,116,118,127,130] At that point, the tunneling probability will depend on the overlap between the donor and acceptor wavefunctions (the first exponential inside the integral of eq. 1, referred to as the Franck-Condon term), which is sensitive to the mass of the tunneling particle, donor-acceptor distance (DAD_e)[131] and its fluctuation along the DHA coordinate (Figure 3.1). Eq. 1 summarizes, in general terms, the form of the rate equation of various Marcus-like models,

$$k = C_{(T)} e^{-(\Delta G^{\circ} + \lambda)^2 / (4\lambda RT)} \int_{DADe_0}^{DADe_1} e^{F(m, DAD_e)} e^{-E_{F(m,DADe)} / k_b T} dDAD_e \qquad (1)$$

where $C_{(T)}$ represents the fraction of reactive complexes. The first exponential term is referred to as the Marcus-term and gives the probability of reaching a TRS. This term is a function of λ, the work associated with reorganization of the heavy-atoms, the reaction's exoergicity (ΔG°), and the absolute temperature T. Importantly, while C and the Marcus-term are mostly isotopically insensitive they generate much of the temperature dependence in the reaction's rate. The second exponent represents the Franck-Condon term (FC), an overlap integral that determines the tunneling probability for each isotope

as a function of donor-acceptor distance. The last exponent has been referred to as the "gating" term, and represents the Boltzman distribution of DAD_es at a given temperature. This term is temperature sensitive, and together with the FC term is the source of the temperature dependency of the KIEs. The last two exponents are integrated over all the DAD_es sampled by the system.

Several researchers employed these models to rationalize their experimental results,[39,66,72,84,120,125,132] where temperature-independent KIEs indicate a system wherein the reactants' relative orientation and electronic states are optimized for H-tunneling and thermally-activated fluctuations of the DAD_e do not affect the KIE. On the other hand, temperature-dependent KIEs indicate a system wherein the reactants' orientation and relative dynamics are not optimal and thermally activated gating motions have a different effect on the transfer of H than that of D or T. These models have been instrumental in qualitatively rationalizing trends in both the temperature and pressure dependence of kinetic data. In recent years, there have been modest attempts to quantitatively link the experimental data to the potential energy surface describing the gating coordinate (to link it to Equation 1.).[48,66-68] However, due to the complexity of the DAD_e's potential surface, and the fact that the DAD's fluctuations do not constitute a normal mode, there are certain limitations in e.g. determining a precise DAD_e and its fluctuations.[69] MD simulations may be necessary to visualize the atomic level structural changes that affect the DAD_e in these reactions.

Here, we assess the modulation of the DAD_e by examining the relationship between the H-transfer rates and temperature dependence of KIEs, and the distribution and fluctuations of the DAD_c[131] via MD simulations, through the targeted mutagenesis of an active site residue. Several other recent studies examined the effects of active site mutations, especially residues that are in direct contact with the substrates, on H-transfer reactions. In the study of a ketoglutarate-dependent dioxygenase, residue F159, which is in a position where the size of its side chain might affect the DAD_e, was systematically

mutated to L, V and A, leading to reduced rates for substrate binding and C-H bond cleavage.[133] For this system where a hydrogen radical is transferred to Fe(IV)=O (probably through a proton coupled electron transfer), elevated KIEs were measured at two different temperatures for the F159L and the F159V mutants which was in accordance with a longer DAD_e as analyzed in terms of a Marcus-like model. However, fluctuations in the DAD_e were not directly examined. In another relevant study on horse liver alcohol dehydrogenase, V203 (a residue analogous to I14 in DHFR) was mutated to alanine, to lead to a longer DAD_c.[134,135] The 2° KIEs suggested reduced tunneling effects in the mutant, and the crystal structures of mutants implied an increase in the ground-state DAD_cs, but no temperature effects or fluctuations/distributions of the DAD were examined. Most recently, a study on a thermophilic alcohol dehydrogenase employed a series of active site mutants which led to enormously elevated Arrhenius prefactors below the physiological temperature range.[123] In this case, no clear trend was observed between the size of the active site residue and the size of the Arrhenius prefactors. Moreover, mutations had little effect on activation parameters at physiologically optimal temperatures. Recent studies on morphinone reductase allowed for the examination of DAD modulation by pressure and temperature dependence through the two active-site residues that are in direct contact with the NADH cofactor, N189 and W106.[66,136] For both residues only the alanine mutant was examined.

In the present work, we build upon these previous studies through examination of intrinsic KIEs, and we also expand the study executed by Scrutton and co-workers[66] by systematically examining the correlation between changes in kinetics and the population distribution along the DAD coordinate through the gradual reduction of the size of a residue that directly modulates DAD_e. Careful selection of the residue of interest allowed us to minimize any electrostatic changes in the active site and focus on changes to the DAD. In addition to measuring KIEs, we used MD simulations to assess the fraction of reactive complexes and distribution of DAD_cs. The model system in this work is

dihydrofolate reductase (DHFR) from *E. coli*, an enzyme that has been the subject of extensive experimental and theoretical studies over the years, and is well suited for the study reported here.[6,137] DHFR is a small, flexible, monomeric protein (18 kDa), that catalyzes the conversion of 7,8-dihydrofolate (H_2F) to 5,6,7,8-tetrahydrofolate (H_4F) with the stereospecific transfer of a hydride from the *pro-R* C4 position of the nicotinamide ring to the *si* face of C6 of the dihydropterin ring. The complex kinetic mechanism of DHFR has been determined from equilibrium binding, steady-state, and presteady-state kinetic studies.[6,137]

Previous measurements of intrinsic KIEs and their temperature dependence implied quantum mechanical tunneling of the hydride in the wild-type DHFR (WT DHFR) catalyzed reaction.[83] Kinetic studies of several distal mutants of DHFR indicated an important role of remote residues in modulating the H-tunneling process.[84,103,138] The latter studies supported the hypothesis that a set of equilibrated conformational changes are coupled to the chemical transformation (C-H→C transfer), as predicted by hybrid quantum/classical MD simulations.[18,139] Nonetheless, the long distance and complex relations between these remote residues and the active site prohibited a microscopic explanation of the effect of the mutants on KIEs and on the DAD. Reproducing similar observations via active site mutations, which have more straightforward effects on DAD_e and DAD_c, is critical in rationalizing analogous effects caused by remote mutants or altered conditions.

The focus of the present study is an active site residue, Ile 14, a hydrophobic residue situated behind the nicotinamide ring of the cofactor (NADPH) that keeps the nicotinamide ring, i.e., the H-donor, in close proximity to the pterin ring of the substrate, i.e., the H-acceptor (Figure 3.2). Importantly, this hydrophobic side-chain is typical to many nicotinamide dependent enzymes, which further broadens the application of the current study. Two-dimensional heteronuclear (^1H-^{15}N) magnetic relaxation studies of DHFR demonstrated that this residue exists as two rotamers, about the χ_1 dihedral angle

(χ_1 :N-Cα-Cβ-Cγ1), in solution; the more populated +*gauche* rotamer and smaller but significantly populated *trans* rotamer.[15] However, in both open and occluded crystal structures of WT DHFR, I14 residue is observed as only the +*gauche* rotamer. Modeling suggested that if this residue occupied the *trans* rotameric state, it would clash with the nicotinamide ring. In order for residue 14 to exist as a *trans* rotamer, the nicotinamide ring would be displaced towards the pterin ring. Brook and co-workers[17] computed the free energy surfaces corresponding to the χ_1 dihedral angle of residue 14, along the reaction coordinate, as part of the conformational change of the Met20 loop. They found that the *trans* rotamer population is observed only in the open state and in high-energy conformations leading to the occluded state of that loop. Only the +*gauche* and small amount of –*gauche* populations are present in the closed state; the state in which chemistry takes place. Moreover, they observed that the free energy barriers separating the functional important conformational states of the Met20 loop of DHFR are small and can be populated via thermal fluctuations.[17] These two rotameric populations are of importance in analyzing our MD simulation (see Results and Discussion).

In earlier kinetic studies of residue 14 we found an order of magnitude reduction in the rate of the hydride transfer for I14A relative to the WT DHFR.[140] In a more recent communication we reported the temperature dependence of the intrinsic KIEs of this mutant.[141] Here, we extend these studies to a rigorous and systematic reduction of the side chain volume of I14 without changing its electrostatic properties. We found that the mutation leads to an increase in the magnitude of the KIEs as well as in their temperature dependence, and is also associated with reduction in hydride-transfer rate. In addition, classical MD simulations suggest new populations of DAD_cs, with larger average DAD_c and broader distributions, as well as a smaller population of the active conformers with the similar DAD_cs to WT DHFR. The analysis of all findings establishes a benchmark for the interpretation of KIEs and rates at the molecular level, and has significant applications to DHFRs and other enzymes.

3.2 Materials and Methods

[Ad-^{14}C]-NAD$^+$ (specific radioactivity of >220mCi/mmol) was purchased from Amersham Pharmacia. 7,8-Dihydrofolate (H_2F) was prepared by dithionate reduction of folic acid as described elsewhere.[107] Glucose dehydrogenase from *Bacillus megaterium* (GluDH) was purchased from Affymetrix / USB. All other materials were purchased from Sigma unless otherwise noted.

3.2.1 Synthesis of labeled cofactors for 1˚KIEs

(*R*)-[4-^{3}H]NADPH (680 mCi/mmol) was synthesized by reduction of NADP$^+$ with 2-Deoxy-D-Glucose-^{3}H using glucose dehydrogenase from *Bacillus megaterium* (GluDH), followed by oxidation of the resulting NADPH with acetone using alcohol dehydrogenase from *Thermoanaerobium brockii* (*tb*ADH), and final reduction using GluDH and unlabeled glucose, as described previously.[111] [Ad-^{14}C]-NADPH (50mCi/mmol) was prepared by phosphorylation of [Ad-^{14}C]-NAD$^+$ using NAD$^+$ kinase from chicken liver to produce [Ad-^{14}C]-NADP$^+$, followed by reduction with glucose using GluDH as described elsewhere.[95] (*R*)-[Ad-^{14}C,4-^{2}H]-NADPH (50 mCi/mmol) was prepared from [Ad-^{14}C]-NADP$^+$, which was synthesized as described above, and subsequent reduction with deuterated glucose and GluDH.[142] All synthesized cofactors have been purified by semipreparative reverse-phase HPLC on a Supelco column and stored at -80 ˚C prior to use as discussed elsewhere.[109]

3.2.2 Construction of expression vectors

The sequence of the mutagenic, forward primer (I14V-for) is 5'-GCG-GTA-GAT-CGC-GTT-GTC-GGC-ATG-GAA-AAC-GCC-3', and the sequence of the

mutagenic, reverse primer (I14V-rev) is 5'-GGC-GTT-TTC-CAT-GCC-GAC-AAC-GCG-ATC-TAC-CGC-3', where the site of the mutation is underlined. The sequence of the mutagenic, forward primer (I14G-for) is 5'-GCG-GTA-GAT-CGG-GTT-GGC-GGC-ATG-GAA-AAC-GCC-3', and the sequence of the mutagenic, reverse primer (I14G-rev) is 5`- GGC-GTT-TTC-CAT-GCC-GCC-AAC-GCG-ATC-TAC-CGC-3, where the site of the mutation is underlined. PCR reaction was completed using pET22b-DHFR as a template. The original template was digested with the DpnI restriction enzyme, and the PCR product was transformed into DH5α- cells. Plasmid was extracted from the overnight culture and the sequence was verified by automated DNA sequencing by the University of Iowa DNA facility. Primers were purchased from Integrated DNA Technologies.

3.2.3 Expression and purification of I14V DHFR, I14A DHFR and I14G DHFR

The mutants were expressed, purified and stored as reported for other DHFR mutants.[106]

3.2.4 Competitive and intrinsic primary kinetic isotope effect

For H/T 1˚KIE, *(R)-[4-*^{3}H]NADPH and [Ad-^{14}C]-NADPH, and for D/T 1˚KIE, (*R*)-[4-^{3}H]NADPH and (*R*)-[Ad-^{14}C,4-^{2}H]-NADPH were combined in a radioactivity ratio close to 5:1. Each mixture was co-purified on an analytical reverse-phase HPLC column, divided into aliquots containing 300,000 dpm of ^{14}C, and frozen in liquid nitrogen for short-term storage at -80 ˚C.

All experiments were performed in MTEN buffer (50 mM MES, 25 mM Tris, 25 mM EtOH-NH_2 and 100 mM NaCl) at pH=8.0, over the temperature range of 5-45 ˚C.

H_2F was added to a final concentration of 0.85 mM, which is around a 200-fold excess over NADPH (final concentration of 4 μM). The pH was adjusted to 8.0 at each experimental temperature following the calibration of the pH electrode in appropriate buffers at that temperature. The reaction was quenched by adding an excess of methotrexate (K_d=1 nM), and samples were stored on dry ice prior to HPLC analysis. Before the HPLC-LSC analysis, samples were thawed and bubbled with oxygen to ensure complete oxidation of the product tetrahydrofolate (H_4F). The samples were then separated by reverse-phase HPLC using a method described elsewhere.[109] The observed KIEs were calculated according to ref [29] using the following equation:

$$KIE = \frac{\ln(1-f)}{\ln[1-f(\frac{R_t}{R_\infty})]}$$

where the fractional conversion (f) was determined from the ratio of ^{14}C in the product and reactant, and R_t and R_∞ are the ratio $^3H/^{14}C$ at each time point and at infinite time, respectively.

The intrinsic KIEs were calculated using the modified Northrop equation[35,74]

$$\frac{^T(\frac{V}{K})^{-1}_{H_{obs}} - 1}{^T(\frac{V}{K})^{-1}_{D_{obs}} - 1} = \frac{(k_H/k_T)^{-1} - 1}{(k_H/k_T)^{-1/3.34} - 1}$$

where $^T(V/K)_{Hobs}$ and $^T(V/K)_{Dobs}$ are the observed H/T and D/T KIEs, respectively, and k_H/k_T represents the intrinsic H/T KIE. The intrinsic KIEs were calculated numerically from all possible combinations of observed H/T and D/T values. All intrinsic values were used to fit to the Arrhenius equation in order to determine the isotope effect on the Arrhenius preexponential factors as well as temperature dependence of the KIEs, as described in the main text.

3.2.5 MD simulation

System Setup – The simulations were performed starting from the crystal structure of wild type DHFR, determined at 1.8 Å resolution (PDB entry 1RX2). The crystal structure contains a total of 159 amino acid residues, 153 crystallographic water molecules, and folate and NADP+ as ligands. Missing hydrogens were added to the PDB structure using the leap module of the Amber package.[143,144] The folate and $NADP^+$ ligands were replaced by N5 protonated H_2F and NADPH respectively. The protonation state for all ionizable residues was set for a pH of 7. Thus, histidine residues were modeled as neutral residues with the proton on Nε or Nδ as determined on the basis of possible hydrogen bond interactions deduced from X-ray crystallographic structure. Only His-45 was modeled as charged, based on both NMR[145] and crystallographic[146] studies which indicate a salt bridge between His-45 and the nicotinamide 5'-phosphate of $NADP^+$. Crystallographic studies have also established the existence of a salt bridge between Arg-44 and Adenine 2'-phosphate.[147] The estimated pKa for His-45 determined by PropPKa[148] was 8.83 in accordance with experimental observation. The resulting system has a net charge of -15*e* including N5-protonated- H_2folate (-1) and NADPH(-4).[149] The final protein structure was solvated with a previously equilibrated truncated octahedral box of TIP3P water molecules. The size of the box ensured that all protein atoms were at least 9 Å away from the edges of the box. Overlapping solvent molecules were removed leaving 5879 water molecules. Mutations were performed in silico by changing the corresponding amino acid in the original structure.

Simulation Parameters – All simulations were done at 300 K and 1 bar, regulated with the Berendsen barostat and thermostat,[150] using periodic boundary conditions and Ewald sums for treating long range electrostatic interactions.[151,152] The SHAKE algorithm[153] was used to keep bonds involving hydrogen atoms at their equilibrium length. A 2 fs time step for the integration of Newton's equations was used. Nonbonded interactions had a cutoff radius of 12 Å. The AMBER99 force field[154] parameters were

used for all residues. The $NADP^+$ and NADPH parameters were taken from the Amber parameter database.[155] Gaff force field[156] parameters together with RESP[157] charges calculated at the HF/6-31G* level were used to generate the parameter files for H_2F.

MD runs – All simulations were run with the PMEMD module of the AMBER9 package.[143,144] An equilibration protocol was applied that consists of performing an energy minimization by optimizing the initial structure, followed by a slow heating to the desired temperature using a linear temperature ramp from 100 to 300 K during 80 ps at constant volume and a subsequent 100 ps pressure stabilization run at 300 K and 1 bar . Position frames, which were used for analyzing trajectories, were collected at 2 ps intervals. Production MD simulations consisted of 15 ns simulations: (i) wtDHFR-H_2F-NADPH; (ii) I14V DHFR-H_2F–NADPH, (iii) I14A DHFR-H_2F–NADPH. In the case of (iv) I14G DHFR-H_2F–NADPH, more effective sampling of the conformational space was obtained from multiple short trajectories rather than a single long trajectory. The same sampling methodology was also applied to the (ii) and (iii) mutants in order to compare with the long simulation and between each mutant. A set of ten independent 3 ns simulations for (ii), (iii) and (iv) that differ only in the initial velocities were run. To combine data from different trajectories we have given equal weight to trajectories of equal length. For the (iv) mutant, each trajectory was extended to 6 ns without observing significant changes in the final result. For (ii) and (iii) the distribution of DADs calculated by both methodologies (i.e. long run versus several short runs), was similar, whereas for (iv) it was significantly different, as discussed in the main text. Due to the significant difference of the residue volume in the case of I14G DHFR, the nicotinamide ring is able to sample more space, and in this case the choice of an effective way of sampling is crucial.

MD data analysis – The ptraj module of Amber9 together with a homemade program used to calculate the Phi angle between the planes that fit to the NADPH nicotine amide moiety (C4N, C3N, C2N, N1N, C6N, C5N) and H_2F pterin moiety (C4A,

N5, C6, C4, N3, C2, N1, C8A, N8, C7) were used to analyze the data extracted from the MD simulations. Trajectories were visualized with Visual Molecular Dynamics (VMD).[158] Xmgrace and QtiPlot were used to build the graphics and figures.[159,160] POV-Ray was used for image rendering.[161] DAD distributions were fitted with a combination of Gaussian and split Gaussian functions using the open source software for non linear curve fitting, Fityk.[162]

Gaussian:

$$y(x, a_0, a_1, a_2) = a_0 \exp\left[- \ln(2) \left(\frac{x - a_1}{a_2} \right)^2 \right]$$

where a_0=height, a_1=center, a_2=hwhm (half width at half maximum), and $2 * hwhm = FWHM = 2\sqrt{2 \ln 2}\sigma$, where FWHM is Full Width at Half Maximum.

SplitGaussian:

$$y(x; a_0, a_1, a_2, a_3) = \begin{cases} Gaussian(x; a_0, a_1, a_2), x \le a_1 \\ Gaussian(x, a_0, a_1, a_3), x > a_1 \end{cases}$$

where a_0=height, a_1=center, a_2=hwhm1, a_3=hwhm2

In all the cases the splitGaussians used were only slightly asymmetric, where hwhm1 is a little smaller than hwhm2, so we consider valid the following approximation:

Center=a_1~ mean value

$hwmhl + hwhm2 = FWHM \approx 2\sqrt{2 \ln 2}\sigma$; **hwhm** stands for **h**alf **w**idth at **h**alf **m**aximum, and **FWHM** stands for **F**ull **W**idth at **H**alf **M**aximum

3.2 Presteady-state kinetics

The concentration of the NADPH and H_2F were determined spectrophotometrically by using the extinction coefficients of 6200 M^{-1} cm^{-1} at 340 nm, and 28000 $M^{-1}cm^{-1}$ at 282 nm respectively. Concentration of enzyme was determined spectrophotometrically by using the extinction coefficient of 74600 M^{-1} cm^{-1} at 280 nm,

and by Bradford assay. All the measurements were obtained on a stopped-flow apparatus (Applied Photophysics Ltd., Leatherhead, U.K.), with dead time of 1.6 ms, a 2-mm path length, and a thermally regulated sample cell. The enzyme reaction was monitored by taking advantage of fluorescent resonance energy transfer (FRET) between DHFR and NADPH.[6] Enzyme tryptophans were excited at 290 nm, and FRET results in the strong fluorescence by the reduced cofactor at 450 nm, which is observed through a 390 nm output filter. Since $NADP^+$ is not fluorescent, the chemical step can be monitored by the loss of fluorescence. In the experiment, 20 μM enzyme (either wtDHFR or the relevant mutant) was preincubated with NADPH (10 μM) in MTEN buffer at 25˚C. The reaction was initiated by rapid mixing with 300 μM H_2F. We used the average of five runs for data analysis. All data were analyzed by non-linear least squares fits to single exponential functions using KaleidaGraph 3.5.

3.3 Results and Discussion

3.3.1 Competitive KIEs and Their Temperature Dependence

We determined the temperature dependence of the intrinsic KIEs and hydride transfer rates for a series of DHFR isoforms for which the side-chain that holds the hydride donor (nicotinamide) close to the acceptor (dihydropterin) are systematically reduced from isoleucine to glycine. Figure 3.3 shows Arrhenius plots of the intrinsic H/T 1˚ KIEs for all four enzymes. The same trend was observed for H/D and D/T KIEs as presented in the *SI Text*. Table 3.1 summarizes the volume of these side chains, their hydride transfer rates, the isotope effect on the Arrhenius preexponential factors (A_l/A_h, where l denotes light and h heavy isotope), and the difference in the activation energy between light and heavy isotope ($\Delta E_{ah\text{-}l}=E_{ah}-E_{al}$).

The isotope effects on the preexponential Arrhenius factors (A_H/A_T, A_H/A_D, and A_D/A_T) for the WT DHFR, I14V DHFR and I14A DHFR are larger than unity, and above the semiclassical limit, whereas the values for the I14G DHFR are smaller than unity and below the semiclassical limit. The traditional, semi-classical approach with the Bell correction[43] would suggest that hydride transfer for the first three isozymes involves "extensive tunneling" for both heavy and light isotopes, whereas the hydride transfer for I14G DHFR would be characterized as a case with "moderate tunneling".[27,28] According to the Marcus-like model, A_H/A_T is affected by both the average DAD_e and its distribution, and reveals the difference in the nature of the hydride transfer between these mutants. A longer average DAD_e leads to an increase in the A_l/A_h, whereas a broader distribution of DAD_e-s increases the temperature dependence of the KIEs resulting in a decrease in the A_l/A_h. Because of this ambiguity, a better indicator for the nature of the hydride-transfer is the slope of the Arrhenius plot, (Figure 3.3, i.e., the $\Delta E_{a\ h\text{-}l}$, where h and l are the heavy and light isotopes, respectively) that increases as the distribution of DAD_es broadens. $\Delta E_{a\ h\text{-}l}$ close to zero indicates that the KIEs of WT DHFR exhibits no temperature dependence (within the experimental error), and the larger $\Delta E_{a\ h\text{-}l}$ for the mutants indicates that temperature dependence of the KIEs increases as the size of the hydrophobic residue behind the nicotinamide ring decreases. In terms of the Marcus-like model this means that in the case of the WT DHFR the average DAD_e is optimal for the hydride transfer and has a narrow distribution around the average. The I14V mutant is similar to WT DHFR, but has a slight (but statistically significant) temperature dependence on the intrinsic KIEs. The I14A mutant has the largest intrinsic KIE at 25˚C, but its KIEs' temperature dependence ($\Delta E_{a\ h\text{-}l}$) falls between the I14V and I14G DHFR. This interesting observation supports the earlier examination of distal mutants of DHFR, which concluded that in order to assess the nature of the hydride transfer it is necessary not only to measure the KIE at a single temperature but for the whole temperature range.[84]

According to the Marcus-like model, the inflated temperature dependence of the KIEs in the mutants reflects a broader distribution of DAD_e sampling that is not present in the WT. The average DAD_e in the mutants is too long for efficient tunneling at low temperatures, but at higher temperatures more conformations with a shorter DAD_e are sampled. This affects the rate of transfer by heavy isotopes more than that of protium-transfer because these can only tunnel from the shorter distances, thus leading to temperature dependent KIEs. These observations are in accordance with some of the earlier studies, e.g. a study on the soybean lipoxygenase-1 (SBL-1), which showed that a decrease in the bulk of the active site residue (residue 553, not analogous to I14, not in direct contact with the substrate) was correlated with an increase in the temperature dependence of the 1° KIE.[68] Numerical modeling using a form of equation 1 provided more evidence that these remote mutations led to longer DAD_es. However, in other studies, in particular the one on morphinone reductase, Pudney et al.[66] found an increase in temperature dependence of KIEs with an increase in the size of the active-site residue. In that particular study, the residue of interest was V108, which is not in direct contact with the cofactor NADH; thus the effect of the size of the residue on the DAD_e was hard to assess. The other residue of interest in the same study was W106, which is in direct contact with the cofactor; however, only the alanine mutant was examined and therefore no trends were available. In the pressure-dependence studies on the same enzyme the authors suggested that an increase in the force constant of the compressive mode can lead to an increase in the magnitude of the 1° KIE even as the DAD decreases,[69,163] which became a source of the extensive debate.[164] Our findings are in accordance with the majority of cases where numerical modeling of the temperature dependence of the 1° KIEs using equation 1 results in decreasing temperature dependence with decreasing average DAD_e. From these independent studies it is evident that the relationship between the size of the side chain and the DAD_e might be quite complex, and might go beyond the notion that the smaller size of the residue leads to longer average DAD_e. These results

were the driving force in the experimental approach presented here, where we determined the effect of the DADs' distribution on the nature of the catalyzed H-transfer.

In order to asses the effect of the mutations on the hydride transfer, we measured the single turnover rates at 25 ˚C, pH=7.0, for all mutants and for WT DHFR.[6] Fluorescence Energy Transfer (FRET) decay traces were fitted to single exponential functions with slope. These rates indicate that hydride transfer for the I14V, I14A, and I14G mutants are about 7, 40, and 1000 times slower than WT DHFR, respectively (Table 3.1). There is a clear correlation between the decrease in size of the hydrophobic residue, the rate and the nature of the hydride transfer. We would like to point out that the reduction of the size of this residue is likely to affect the mobility of the M20 loop and consequently affect the fraction of reactive complexes, the pKa of H_2F,[165] the fraction of different M20 loop conformations, and other factors that affect the multisteps reaction's rate, but not the hydride transfer step under study. All these effects are included in the prefactor C(T) in rate eq 1, but do not affect the terms in the integral, including the DAD, its dynamics and distribution. The intrinsic KIEs, on the other hand, probe the hydride transfer step per sé, and not the steps preceding it (such as protonation of N5 position of H_2F, and other isotopically insensitive factors).

3.3.2 MD Simulations on mutants of DHFR

In order to provide a detailed microscopic description of the active site structural change upon mutation of residue 14, we performed MD simulations. One 15 ns simulation was performed for WT DHFR and each mutant, as was previously done for WT DHFR and I14A DHFR.[141] In order to better sample the conformational space for each mutant, we also performed ten independent runs of 3 ns, differing only in initial velocities for each one of them.

A comparison of the conformations is presented in Figure 3.4, which also describes two parameters of interest, DAD_c and Φ. DAD_c is defined as the distance between C4 of NADPH and C6 of H_2F (see Figure 3.4 inset). The relative donor acceptor orientation was measured as the angle (Φ) between the planes that fit the nicotinamide moiety of NADPH and the pterin ring of H_2F (see Figure 3.4 inset). The distribution of DAD_cs and the orientation of donor and acceptor (Φ angle) are displayed in Figure 3.5. The DAD_cs' and Φs' distributions (Figure 3.5, 1D plots on y and x-axis) were fitted to one split Gaussian function or a combination of Gaussian functions and split Gaussian functions (Table 3.2). The correlation is presented as a 2-D plot in Figure 3.5.

The results indicate that reduction in the size of the hydrophobic residue behind the nicotinamide ring leads to an increase in the flexibility of the nicotinamide ring. As a result, the nicotinamide ring can not only explore more orientations at the same DAD_cs, but also this increase in the flexibility leads to an increase in the average DAD_c, a broader DAD_c distributions, as well as new DAD_c populations (Table 3.2 and Figures 3.4-3.5). The different populations are labeled I, II, III, IV and V; the structures that represent these different populations are presented in Figure 3.4 for each mutant, and are overlaid with the average wt-DHFR structure.

The DAD_c distribution for WT DHFR was fitted to one split Gaussian function and the residue I14 was only observed as the +gauche rotamer during the time scale of the simulation. This result agrees well with Brooks's work,[17] where this rotamer represents the major population observed for the closed conformation of WT DHFR. The DAD_c distribution for the I14V mutant was fitted to a combination of one split and one normal Gaussian functions suggesting that there are two populations present during the simulation time. The average structure for the major population is very similar to the WT DHFR (structure I in Figure 3.4), displaying similar DAD_c and Φ distributions, but with a slight increase in the average DAD_c as well as a deviation of the average Φ value found in the WT DHFR. The smaller population (structure III in Figures 3.4 and 3.5) has a

larger average DAD_c with wider distribution, where new Φ values are explored, manifesting themselves as a partial twisting of the nicotinamide ring. In the case of the I14A mutant, the correlation plot (Figure 3.4) shows that the conformational space explored is bigger compared to the I14V mutant. The simulations in this case suggest three populations: (i) the wt-like population; (ii) a new population with similar DAD_c to I, but a different Φ distribution (Structure II); and (iii) the Structure III, equivalent to the one found for the I14V mutant, but with a slightly larger average DAD_c and Φ, which also exhibits broader distributions, indicating more flexibility in the location of the nicotinamide ring (see Figure 3.4 and 3.5). Population III is not expected to contribute to a reactive conformation (average DAD too large), therefore leading to a smaller constant $C_{(T)}$, from the equation 1, which is in accordance with a reduction in rate of the hydride transfer (Table 3.1). On the other hand the new population (II) exhibits the same average DAD_c as the population I, however it is expected to be by far less reactive due to the substantial deviation of the Φ angle from 30˚. As visible in Figure 3.4, the nicotinamide ring of NADPH is almost perpendicular to the pterin ring of H_2F, making the HOMO-LUMO orbital overlap very poor, which has a deleterious effect on the rate.[166] Consequently, population II is not likely to be reactive, but its exact reactivity (if any) is hard to determine without high-level QM/MM calculations that are beyond the scope of this work. Lastly, the hydrogen-bonds (two to residue A7 and one to the backbone of I14) that hold the NADPH amide moiety (see Figure 3.2), show a broader distribution, that is in accord with the elevated flexibility of nicotinamide ring in the I14A mutant relative to I14V and WT DHFR.

MD simulations for the mutant with the smallest side chain, I14G DHFR, suggested all five significant populations. In this case, the three H-bond interactions mentioned before, ((a), (b) and (c) in Figure 3.2) are longer and weaker than in the wt and I14V/ I14A mutants. The last population, V, has one of the H-bonds (c), completely broken, while the other two (a) and (b), are only weakly established (see Figures 3.6-3.7

in the *SI Text*). Once this H-bond is broken the structure remains in conformation V and doesn't return to wt-like or other conformations during the time scale of the simulation (the simulation was extended to 30 ns). The breakage of the H-bonds, particularly the (c) H-bond, results from the diminishment in the side chain of the residue 14, and contributes to the increase in the flexibility over other mutants and the ability to explore a broader conformational space that leads to a non-reactive population (DAD_cs > 6 Å). Finally, Table 3.2 lists the fraction of each population found, which appear to correlate well with the reduced rate of H-transfer. In all the cases, the wt-like population is the predominant one, although its relative contribution decreases in proportion to the size of the side chain, leading to decrease in the C_T term in Eq. 1. A similar effect on rates was obtained in a recent study where modeling of the conformational sampling that lead to elevated Arrhenius prefactors (below the physiologically optimal temperatures) for the thermophilic alcohol dehydrogenase showed an increase in the fractional occupation of catalytically inactive regions of conformational space.[123] More importantly in this work, a correlation was observed between the temperature dependence of the intrinsic KIEs ($\Delta E_{aT\text{-}H}$, Table 3.1) and the DAD_c, its σ values, and the Φ angle (Table 3.2) for the reactive population (I). As the $\Delta E_{aT\text{-}H}$ increases (Table 3.1), the average DAD_c of population I increases and its distribution widens, while the average Φ angle decreases (Table 3.2). This important correlation is also visualized in Figure 3.5, where the reactive population (short DAD_c and $0^\circ < \Phi < 60^\circ$) is larger for the WT (red), smaller and with broader distribution toward longer DADs for I14V (green), and more so for I14A (blue). The population I for I14G is too small to be clearly observed in Figure 3.5, but has the largest DAD_cs distribution (σ) and smallest Φ (Table 3.2).

The MD simulations provide molecular insight and support to the interpretation of the kinetic findings via the Marcus-like model: the smaller side chain acts to broaden the sampling of configurations within the reactive ternary complex along the reaction coordinate. This leads to a steeper temperature dependence of intrinsic KIEs and reduced

hydride transfer rates. The MD simulations also revealed the importance of the donor-acceptor orientation (DAD_c and Φ), and its relative distribution, which affects the overlap between the HOMO and LUMO.[131]

3.4 Conclusions

The relationship between the DAD and its distribution and dynamics to the rate of hydride-transfer and the temperature dependence of intrinsic KIEs has been examined. The model system was DHFR, which like many nicotinamide dependent enzymes has a hydrophobic amino acid behind this cofactor that positions the nicotinamide ring close to its counter substrate. Here we examined the effect of systematic active site mutations that decrease the size of the side chain of this amino acid (I14 to V, A, and G) on the enzyme catalyzed hydride transfer step. The hydride-transfer rates and the temperature dependence of intrinsic KIEs were measured, and the ensemble of ternary complex structures was assessed through MD simulations. These findings suggested that residue I14 participates in the restrictive active-site motions that modulate the DAD. The findings confirm the relations predicted by the Marcus –like model, where longer DADs and broader distributions of DADs lead to a steeper temperature dependence of intrinsic KIEs ($\Delta E_{a\ h\text{-}l}$, determined mostly by the integral in Eq. 1) and the smaller fraction of reactive conformations ($C_{(T)}$ in Eq. 1) contributes to the reduction of the hydride transfer rate. The correlation that was found between DAD distributions and the temperature dependence of the intrinsic KIEs provides a valuable benchmark for understanding the active site dynamics and H-tunneling in DHFR catalyzed reactions, including remote mutations or altered protein scaffolds, for which it has not been trivial to rationalize the kinetic findings at a molecular level. It is also likely to be relevant to C-H→C reactions in other enzymes, as well as non-enzymatic reactions in general, as the correlation found here is

likely to hold whether the DAD_es are imposed by proteins' scaffold or by solvent molecules.

The current findings suggest that this series of DHFR mutants is suitable for more in-depth examination by a broad variety of researchers applying a variety of methods. Future studies of this system may include high-level hybrid classical-quantum mechanical MD simulations,[62,167] structural studies,[4] examination of the systems dynamics at millisecond to nanosecond time scales using NMR relaxation experiments,[121] and femtosecond to picosecond time-scale motions using two-dimensional infrared spectroscopy.[125] Those experiments will allow more in depth examination of possible correlations between structure, dynamics, and the nature of H-transfer in a well-defined environment imposed by the enzyme, and should reflect on C-H→C reactions in general.

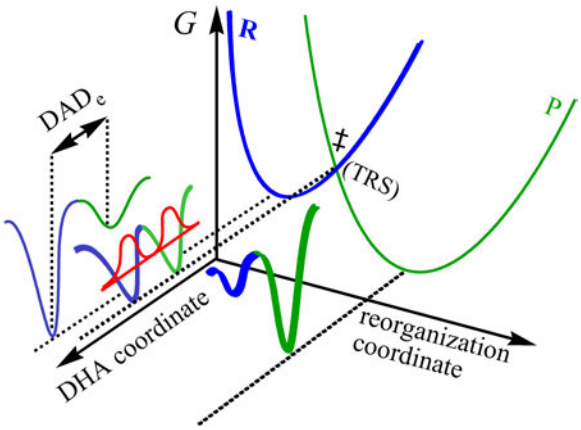

Figure 3.1 Illustration of a Marcus-like model. The reorganization coordinate represents the heavy-atom motions that carry the system to the TRS(‡). The blue and green correspond to the reactant and product states, respectively. The DHA coordinate (donor-hydrogen-acceptor) represents the fluctuations of the DAD_e. The red curve represents the wave functions of the hydrogen nucleus.

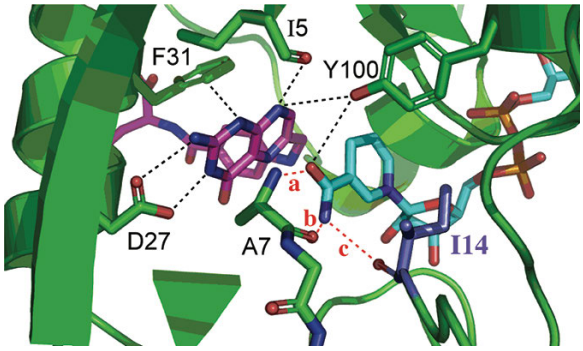

Figure 3.2 The active-site of DHFR from *E. coli* (PDB ID 1RX2) emphasizing the role of Ile14 (metallic blue) as a support of the nicotinamide ring of $NADP^+$. The nicotinamide ring is highlighted in light blue and the folate in magenta. Several other residues that form hydrogen bonding with the amide of NADPH are highlighted as well as I14 and A7. Three distinct hydrogen bonds, labeled in red, are: (a): NADPH(O-amide)-Ala-7(H); (b): NADPH(H_{72})-Ala-7(O); and (c): NADPH(H_{71})-Ile-14(O). The pterin ring is also immobilized in the active site via tight van der Waals interactions with F31, and strong hydrogen bonds to D27 and I5.

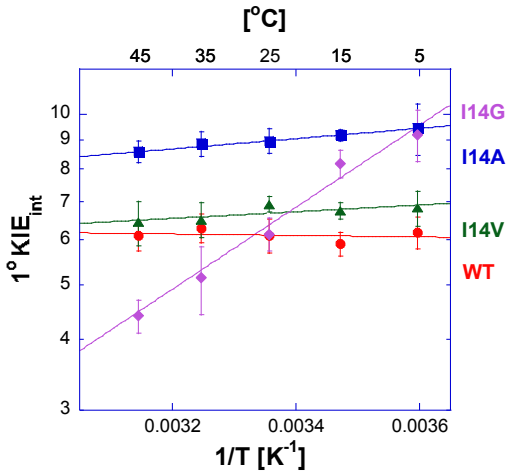

Figure 3.3 Arrhenius plot of intrinsic H/T KIEs (on a log scale) for wild-type (red)[83], I14V DHFR mutant (green), I14A DHFR (blue)[141] and I14G DHFR (purple). The lines represent the nonlinear regression to an exponential equation.

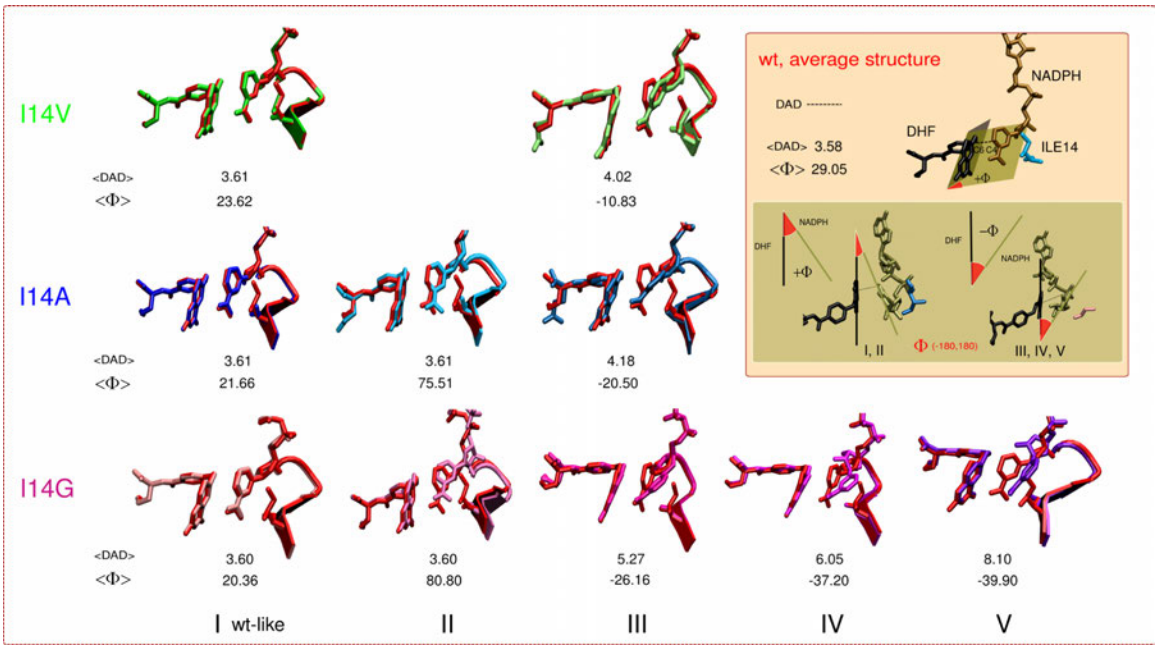

Figure 3.4 Structures comparing WT (red) to the different conformations found for the three mutants (see color code of each mutant on the left) together with the corresponding DAD_c and F average values (DAD in the figure refers to DAD_c). (I) A wt-like conformation; (II) A conformation with almost the same DAD_c average distance as the conformation I, but with the nicotinamide almost perpendicular to the H_2F pterin ring; (III) A conformation where the nicotinamide is partially twisted to the right towards residue 14; (IV) A conformation similar to III but with a broader distribution of distances; and (V) A conformation where the nicotinamide is completely twisted towards residue 14. Inset: definition for DAD_c distance, F angle, and average values found for WT DHFR. Structures I and II display positive values for F, whereas structures III, IV and V (nicotinamide twisted to the right, towards residue 14) display negative values.

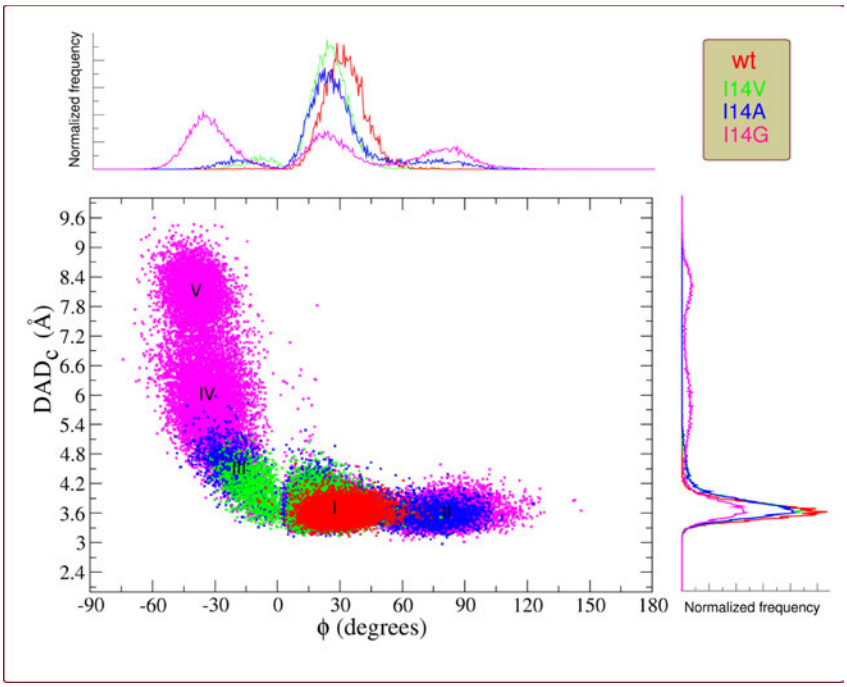

Figure 3.5 Correlation plot between the DAD_c (angstroms) and the relative orientation of donor and acceptor (Φ, degrees) for **WT** DHFR (red), **I14V** (green), **I14A** (blue), **I14G** (magenta). I, II, III, IV and V indicate the different populations identified for each DAD_c and **Φ** values. Overlaid wt and mutants DAD_c and **Φ** distributions are shown on the y and x axis respectively.

Table 3.1 Comparative kinetic parameters of the DHFR I14 mutants.

Parameters	WT	I14V	I14A	I14G
Residue volume[a] ($Å^3$)	124	105	67	48
k_H[b] [s^{-1}]	228 ±8[d]	33.3 ±3.1[f]	5.7 ±0.3[f]	0.22 ±0.04[f]
A_H/A_T[c]	7.0 ±1.5[e]	4.2 ±0.4[f]	4.7 ±0.5[g]	0.024 ±0.003[f]
ΔE_{aT-H}[c], [kcal/mol]	-0.1 ±0.2[e]	0.27 ±0.05[f]	0.39 ±0.06[g]	3.31 ±0.07[f]

a. Side chain volume.[168]

b. Presteady state rates of H transfer at 25˚C and pH 7.

c. Similar trends were observed for H/D and D/T (data not shown).

d. Ref. [169].

e. Ref. [95].

f. This work.

g. Ref. [141].

Table 3.2 Gaussian fitted distributions of DAD_c for the different conformations found along MD simulation (see text).

DHFR Active site conformation		<DAD> (Å)	σ (Å)[c]	<Φ>[d] (degrees)	Fraction	R
wt	I[a]	3.58	0.16	29.0	1	0.9979
I14V	I[a]	3.61	0.17	23.6	0.86	
	III[b]	4.02	0.31	-10.8	0.14	0.9984
I14A	I[a]	3.61	0.17	21.7	0.68	
	II[a]	3.61	0.17	75.5	0.13	0.9980
	III[b]	4.18	0.49	-20.5	0.19	
	I[a]	3.60	0.19	20.4	0.33	
I14G	II[a]	3.60	0.19	80.8	0.26	0.9943
	III[b]	5.27	0.82	-26.2	0.09	
	IV[b]	6.05	0.67	-37.2	0.22	
	V[b]	8.10	0.36	-39.9	0.1	

a. Fitted to a split-Gaussian

b. Fitted to a Gaussian.

c. For split-Gaussian σ is the average of both parts.

d. Φ separately from the DAD_c. See SI for the procedure and parameters (Table S3).

Supplementary Information

Table 3.3 Intrinsic KIEs and their standard errors for I14V DHFR.

Temp. ˚C	**H/T KIE**	**H/D KIE**	**D/T KIE**
45	6.40 ±0.57	3.67 ±0.23	1.74 ±0.05
35	6.49 ±0.46	3.71 ±0.19	1.75 ±0.04
25	6.92 ±0.22	3.88 ±0.08	1.78 ±0.02
15	6.73 ±0.22	3.80 ±0.09	1.77 ±0.02
5	6.80 ±0.50	3.83 ±0.19	1.78 ±0.04

Note: These values are calculated from the observed H/T and D/T KIE data using Northrop's method as described in the Materials and methods. The errors indicate the 95% confidence level.

Table 3.4 Intrinsic KIEs and their standard errors for I14G DHFR.

Temp. ˚C	**H/T KIE**	**H/D KIE**	**D/T KIE**
45	4.39 ±0.30	2.82 ±0.13	1.56 ±0.03
35	5.10 ±0.70	3.13 ±0.30	1.63 ±0.07
25	6.13 ±0.32	3.56 ±0.16	1.72 ±0.03
15	8.17 ±0.27	4.36 ±0.17	1.88 ±0.03
5	9.15 ±0.96	4.72 ±0.34	1.94 ±0.06

Note: These values are calculated from the observed H/T and D/T KIE data using Northrop's method as described in the Materials and methods. The errors indicate the 95% confidence level.

Table 3.5 Fitted Φ˚ angle distribution for wtDHFR and DHFR mutants.

	Center	Area	Height	FWHM	Int. Width	R
wtDHFR						
	29.05	0.995	0.042	22.33	23.77	0.9912
I14V						
I	23.62	0.930	0.045	19.52	20.78	0.9948
III	-10.84	0.063	0.004	15.01	15.97	
I14A						
I	21.66	0.768	0.034	21.03	22.39	0.9893
II	75.51	0.164	0.003	33.40	36.84	
III	-20.50	0.071	0.003	20.76	22.10	
I14G						
I	20.36	0.305	0.013	22.74	24.20	0.9924
II	80.80	0.234	0.007	30.27	32.22	
III	-26.16	0.143	0.006	22.11	23.54	
IV	-37.20	0.189	0.011	16.54	17.60	
V	-39.87	0.13	0.005	21.60	22.99	

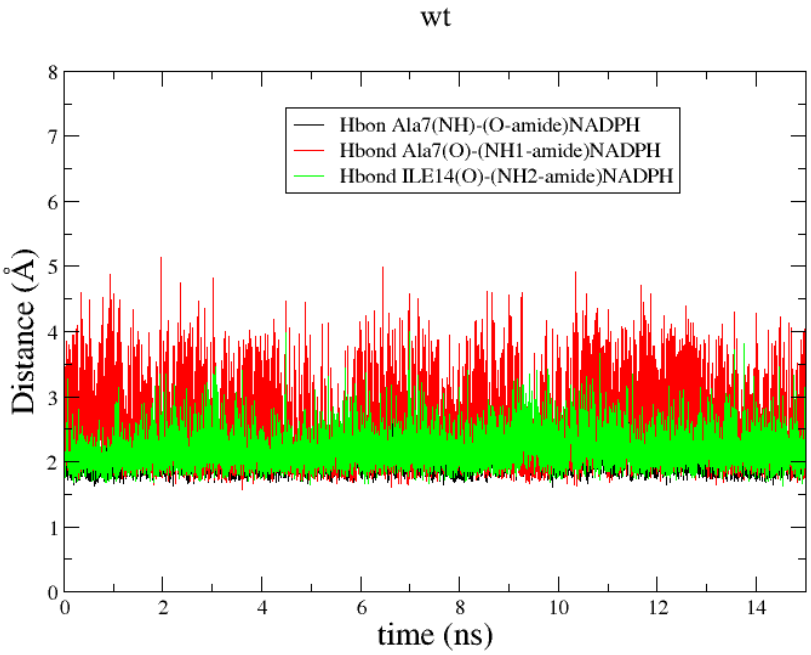

Figure 3.6 Time evolution for several hydrogen bonds between the nicotinamide ring and surrounding residues, for wt DHFR. Average values with the standard deviations presented in the parentheses are: Ala7-NH---O-amide(NADPH): 2.02(0.21); Ala7-O---NH1-amide(NADPH): 2.53(0.62); Ile14-O---NH2-amide(NADPH): 2.17(0.27).

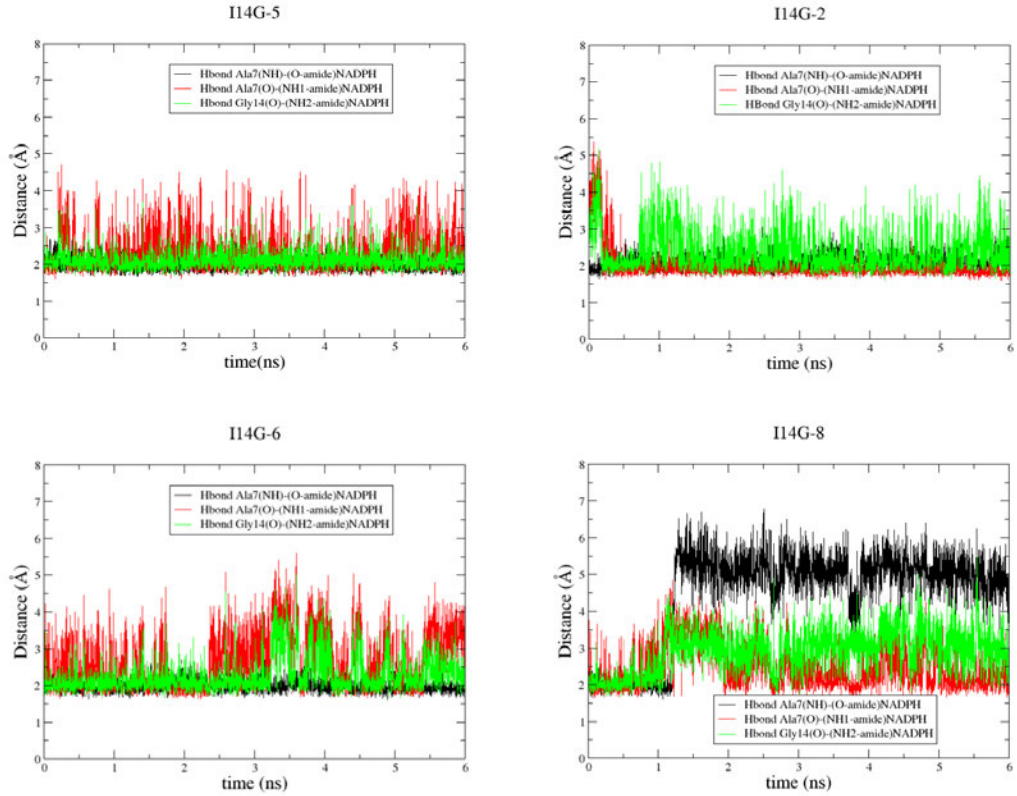

	Run 5: wt-like	Run 2: structure II	Run 6: wt-like and structure III	Run 8: mainly structure V
Ala7-NH---O-amide(NADPH)	2.00(0.18)	2.10(0.19)	1.99(0.17)	4.45(1.33)
Ala7-O---NH1-amide(NADPH):	2.33(0.57)	1.98(0.44)	2.68(0.79)	2.46(0.60)
Ile14-O---NH2-amide(NADPH)	2.11(0.25)	2.38(0.56)	2.27(0.47)	2.90(0.62)

Figure 3.7 Time evolution for several hydrogen bonds between the nicotinamide ring and surrounding residues, for a couple of I14G runs. Average values are presented together with the standard deviations in the following table.

CHAPTER 4.
STRUCTURAL STUDY ON A SERIES OF DIHYDROFOLATE REDUCTASE MUTANTS[iv]

4.1 Introduction

One of the most highly studied enzymes from the structural/dynamic/functional viewpoint is dihydrofolate reductase from *Escherichia coli* (*ec*DHFR; EC 1.5.1.3), an ubiquitous enzyme crucial for biosynthesis of purines, pyrimidines and certain amino acids. This NADPH-dependent oxidoreductase catalyzes a single stereospecific hydride transfer from the pro-*R* C4 position of NADPH to the *re* face of C6 position of 7,8-dihydrofolate (H_2F) producing 5,6,7,8-tetrahydrofolate (H_4F) and $NADP^+$. Both kinetics and catalytic mechanism have been extensively studied,[6,140,170] and numerous structural studies of different enzymatic complexes exposed important conformations, thus providing crucial information regarding the functionality of this enzyme.[4,146,171,172] Study of the temperature dependence of the kinetic isotope effects (KIEs) indicated that the hydride is being transferred through quantum-mechanical tunneling.[83] A phenomenological model,[39,40,44,57,66,73,85,125,127,173-177] addressed here as Marcus-like model, used for the analysis of the temperature dependence of the KIEs suggests that protein motions contribute to the reorganization of the protein, solvent and ligand atoms that assist the structural changes in the active-site as the reaction proceeds from the reactant state to the tunneling ready state (TRS). At the TRS faster motions (femto- to picosecond timescale) control the fluctuations in the donor-acceptor distance (DAD) that affect the H-tunneling probability. Various simulation and computational studies, based on the x-

[iv] This chapter is in preparation to be submitted to the journal *PLOS ONE*.

ray crystal structures, have examined the nature of the hydride transfer in *ec*DHFR and addressed the role of protein motions in catalysis.[17,122,178]

Relating X-ray crystal structures at atomic-resolution to enzyme functionality is not a trivial task. From the structural viewpoint it would be ideal to experimentally observe and follow the whole hydrogen transfer event to atomic detail. However, for most of the H-transfer enzymatic reactions that is unattainable. Nonetheless, high-resolution crystal structures of either mimics of transition state or Michaelis complex can provide information regarding the donor and acceptor groups relevant to the H-transfer reaction. X-ray crystal structures are still static pictures of the enzyme, and present an ensemble and a time-averaged picture of the protein. However, together with temperature factors, kinetic, and computational results can give us important information for establishing the structure-function-dynamic relationship in enzymes.

*Ec*DHFR is a small monomeric protein that consists of central eight-stranded beta-sheets and four alpha helices. The active site cleft divides the enzyme into two structural subdomains: the adenosine binding subdomain and the major subdomain (Figure 4.1a). The adenosine subdomain provides the binding cleft for the adenosine moiety of the cofactor. The major subdomain is much larger and is dominated by the three loops on ligand binding face that surround the active site. Those three loops are: M20 (residues 9-24), F-G (residues 116-132) and G-H (residues 142-150) loops. M20 loop is also referred to as an active-site loop since it lays directly over the active site and protects it from the solvent. Previous X-ray crystallization studies showed that in the crystalline state M20 loop can be observed in the four distinct conformations: open, closed, occluded and disordered.[4] The existence of the occluded and the closed conformations in the solution has been supported by the NMR experiments,[179] and the loop movement between these two conformations was shown to coordinate with different stages of the catalytic cycle.[4,6,180] On the other hand, the open conformation is thought to be an intermediate state between the closed and occluded conformations and has been

observed only in certain crystalline forms where this conformation is stabilized by the certain crystalline lattice contacts.[4,146] In the solution, M20 loop of the apoenzyme exists in the occluded conformation where it protrudes into the active site, blocking it from the solvent and nicotinamide-ribose moiety of the $NADP^+$. Binding of the substrate induces a transformation to a closed form of the enzyme. Closed conformation allows for the positioning of the cofactor and substrate reactive centers in the close proximity within the active site. Large amount of available experimental evidence suggest that flexibility of the M20 loop on a millisecond timescale is relevant to substrate/cofactor binding and product release. However while loop fluctuations prove to be important in the catalytic cycle of DHFR, the M20 loop might also contribute to catalysis through active site compression and stabilization of the transition state.[5,14]

Quantum-mechanical/classical-molecular dynamics (QM/MM) calculations identified a network of coupled motions, spread throughout the protein that may participate in the promoting motions.[11,16,18,181] Promoting motions of the reactive complex were calculated as thermally averaged structural changes that occur as system evolves along the reaction coordinate. This particular simulation identified several residues to be part of the network of promoting motions, including hydrophobic residue I14 located behind the nicotinamide ring of NADPH (Figure 4.1b and 4.1c). Two-dimensional heteronuclear (^1H-^{15}N) magnetic relaxation studies of DHFR demonstrated that this residue exists as two rotamers, about the χ_1 dihedral angle (χ_1 :N-Cα-Cβ-Cγ1), in solution; the more populated +*gauche* rotamer and smaller but significantly populated *trans* rotamer.[15] MD simulations confirmed these results and showed that if the residue occupied the *trans* rotameric state it would clash with nicotinamide ring.[17] This clash could be alleviated only if nicotinamide ring is displaced towards the pterin ring. Previous QM/MM calculations also suggested that motions of certain active-site residues, including I14 (Figure 4.1c), modulated the hydrogen tunneling and dynamic barrier re-crossing.[64] Recently, we tested this hypothesis by measuring the temperature dependence

of KIEs on the series of mutants of residue I14.[41,85] Temperature dependence of the KIEs showed that decrease in the size of this hydrophobic residue leads to an increase in the average DAD and its distribution at the TRS. MD simulations on the ternary E-NADPH-H_2F complex for the series of I14 mutants indicated that decrease in the size of this residue leads to an appearance of the new DAD populations with longer average DAD and broader DAD's distribution. Moreover, mutations also distorted donor-acceptor orientation (orientation between the pterin and nicotinamide rings).[85]

In order to relate the mutations' effect on H-transfer to the mutants' structure we examined the ternary complexes of the *ec*DHFR active site mutants I14V, I14A and I14G using X-ray crystallography. We choose to study the complex with folate and $NADP^+$ since this is a proposed mimic of Michaelis complex, and thus has been previously used as starting point for most published QM/MM and MD simulations. The goal of the study presented here was to determine the structures of the mutants within single crystal packing so that distortions due to crystal-packing effects remain constant for the series of structures. Since crystal packing effects cause small local, and sometimes global, deformations, we also attempted to examine the same complexes in different crystal packings and space groups in order to get a better view of the dynamic behavior of these mutants, as it was previously done for WT *ec*DHFR.[4] Lastly we wanted to see if under different crystallization conditions we would be able to trap different populations of ground state structures that have been suggested by the MD simulations.[85]

4.2 Materials and methods

4.2.1 Preparation of I14V, I14A and I14G DHFR ternary complexes for crystallization

*Ec*DHFR mutants were expressed and purified as described before.[182] Briefly, E. coli ER2566 ΔthyA ΔfolA cells containing the DHFR genes in the pET22b vector were

grown in LB medium in the presence of 50 mg/l thymidine and 100 mg/ml ampicillin at 37 °C to an OD_{600nm} of 0.6-0.8. DHFR expression was induced by the addition of the IPTG to a final concentration of 0.4 mM, and incubation continued at 18 °C overnight. Cells were harvested by centrifugation at 4 ˚C for 30 min. The cell pellet was re-suspended in the lysis buffer (25 mM NaH_2PO_4, pH 7.0, 5 mM EDTA pH 8.0, and 10% v/v glycerol), and lysed as described previously.[182] The supernatant was purified using methotrexate-agarose affinity column, followed by DE52 column.[182] Eluted fractions were tested for protein via UV and Bradford assay, and the purity was assessed using SDS-PAGE gel. Only fractions containing pure protein were pooled, concentrated and dialyzed against storage buffer. Protein was either stored at -80 °C until further use, or loaded onto a Superdex-75 (GE) gel filtration column pre-equilibrated with the buffer containing 20 mM Tris-HCl, pH 7.5. DHFR eluted in a single peak, which was tested for the monodispersity using dynamic light scattering on the NanoStar (Wyatt Technology).

Concentration of the pooled fractions was measured using UV absorbance (ε_{280}=74.6 $mM^{-1}cm^{-1}$) and Bradford assay. Due to low solubility of folate, folate was added to a dilute protein solution at three-fold molar excess relative to the concentration of specific DHFR mutant. The sample was incubated on ice for 30 min, and then filtered using Milipore 0.22 μm filter. The binary complex was concentrated to a final concentration of 12-18 mg/ml (as determined by Bradford assay). $NADP^+$ was added as a solid to the concentrated binary DHFR-Folate complex at a five-fold molar excess to DHFR.

4.2.2 Crystallization conditions

All enzyme-Folate-$NADP^+$ ternary complexes were crystallized via the hanging drop vapor diffusion method by mixing 400 nl well solution and 400 nl of prepared ternary complex using TTP LabTech Mosquito. The only exception is I14G DHFR

ternary complex whose crystals were obtained through macroseeding into 4 µl wells (2 µl well solution and 2 µl of protein complex).

In more detail: I14G-$NADP^+$-Folate crystallized in the $P2_12_12$ space group after macroseeding under the following conditions: 16 mg/ml I14G DHFR, 0.1 M Tris, pH 8.5, 0.9 M LiCl, and 36% w/v PEG 6,000; at 18 °C. Crystals appeared within 7 days after macroseeding.

I14V-$NADP^+$-Folate ternary complex crystallized in the $P2_1$ space group under the following conditions: 16 mg/ml I14V DHFR, 0.1 M Tris, pH 8.5, 0.1 M LiCl, and 34.2% w/v PEG 6,000; at 18 °C, within 2 weeks.

I14A-$NADP^+$-Folate ternary complex was crystallized in $P2_1$ space group under the following conditions: 15 mg/ml I14A DHFR, 0.2 M Lithium acetate, and 20% w/v PEG 3,350; at 18 °C, within 7 days.

4.2.3 Data collection and structure determination

Crystals were flashed-cooled in liquid nitrogen, and data were collected at 100 K at the 4.2.2 synchotron beamline at the Advance Light Source of the Lawrence Berkley National Laboratory. The data were either processed using d*Trek[183] (for I14G) or XDS[184] (for I14V and I14A mutants). All structures were determined by molecular replacement in CCP4[185] (with PHASER[186]), using the coordinates for the refined WT *ec*DHFR structure (PDB 1RX2) with the ligands removed to generate the initial model. Refinement and model building for all structures were done using REFMAC[187] and COOT[188]. Model bias was avoided during the initial refinement by removing the substrate and cofactor from the model. Iterative composite OMIT maps were generated and used where structural features were in doubt. During the early stages of the refinement, hydrogens were included in riding positions, and isotropic temperature factors were refined. In the final stages of the refinement, for the I14A-Folate-

$NADP^+$complex, anisotropic temperature factors for all protein atoms (the ligand atoms were excluded) were refined. All structures were refined with good geometry (rms deviations in bond lengths of 0.015-0.03 Å, rms deviation in bond angles of 1.74-2.54°), with the possible exception of the I14A structure, which showed higher overall temperature factor for molecule B (Figure 4.2). These problems are probably a result of the static disorder. Data and final refinement statistics are given in Table 4.1.

4.2.4 Calculation of the normalized B-factors

Temperature factors for the C_α atoms were either taken from PDB (for WT) or were a result from our refinement procedures. For each protein the B-value of each C_α was normalized by the following equation:

$$B' = \frac{B - B_{ave}}{B_{ave}}$$

where B' is the normalized B-factor and B_{ave} is the average value for a chosen structure.

4.3 Results and Discussion

4.3.1 Crystal structures of the I14A and I14V *ec*DHFR.

Ternary complexes with I14V and I14A mutants crystallized in the $P2_1$ space group, in an open conformation similar to that observed for the WT (PDB ID 1RB2). Difference in crystal growth conditions produced two isomorphous crystals that have very similar though nonisomorphous unit cell parameters to WT, however crystal packing seems to be the same for both the WT and the mutants. There are two crystallographically independent monomers in the asymmetric unit. It has been previously shown that *ec*DHFR always crystallizes as two molecules per asymmetric unit in $P2_1$ space group. The rmsd fit between backbone atoms of the molecule A for single mutants and the

molecule A for the wild type enzyme in its open conformation is 0.29 Å for I14V and 0.33 Å for I14A. Table 4.1 summarizes the X-ray data collection and refinement. The difference in the number of fitted atoms between the two structures is a result of the alternative conformations of few surface residues. The difference in the number of fitted ligand atoms is a result of the disorder observed for the nicotinamide-ribose moiety for $NADP^+$ in the molecule B of I14A mutant.

4.3.1.1 $NADP^+$cofactor binding and the architecture of the active site

Both substrate mimic and the co-factor are present in each molecule. Kinetic and structural studies have shown that during the kinetic cycle NADPH molecule binds to occluded conformation of the protein, in which M20 loop protrudes into the nicotinamide-ribose binding pocket. The initial binding of the NADPH molecule occurs through 2'-phosphate-ADP moiety. The consequent opening of the M20 loop allows for the nicotinamide-ribose moiety to bind in the active site. When this occurs the nicotinamide-ribose moiety forms stabilizing van der Waals contacts and H-bonds with residues that are part of the M20 loop. These interactions favor the closed form of the M20 loop forming a potentially reactive conformation. It has been observed previously that binding of the nicotinamide-ribose moiety is strongly influenced by the presence of pterin ring. When M20 loop is in the open conformation the p-aminobenzoylglutamate binding cleft is widened significantly creating a 8 Å opening to the nicotinamide binding site. This opening allows for the nicotinamide-ribose moiety to be bound in the active-site, as observed in the molecule A, however rotation about the PN-O3 bond can place the nicotinamide-ribose moiety out into the solvent, as in molecule B. Comparison to other ternary structures of WT *ec*DHFR, which crystallized in various crystalline forms but in the open conformation, reveals the same observation.

Figure 4.3a shows the binding of the $NADP^+$ and folate in the active site of I14A *ec*DHFR. Several important active-site residues in direct contact with either the nicotinamide ring of $NADP^+$, or pterin ring of folate are also presented. As indicated by the electron density maps the positions of all the atoms are well-defined. The overlap with WT structure indicates no significant changes in the position of the active-site residues or folate, however it indicates a slight displacement of the nicotinamide ring towards the pterin ring in mutants from the original position in WT structure (Figure 4.3b). This is also evident from an increase in the hydrogen bond between the nicotinamide O7N and I5(N) (Figure 4.4). This displacement in the nicotinamide ring results in the slight difference in donor-acceptor distance (distance between the C4 of nicotinamide ring to C6 of pterin ring) between the WT (3.6 Å) and I14V/I14A (3.2 Å) enzymes.

4.3.1.2 M20 loop conformation

The open conformation is the most frequently occurring conformation crystallographically and is the only conformation that was observed for the I14A and I14V mutants. However, even though it has been shown that closing of the M20 loop is an important step in the catalysis of *ec*DHFR, as the residues in the loop position nicotinamide ring in the close proximity to the pterin ring, replacement of the part of the M20 loop (residues 16-19) with a single glycine residue yields a slow, but nonetheless an active enzyme. The hydride transfer rate is reduced by more than 500-fold, however neither K_m for H_2F or NADPH are significantly affected.[189] This could suggest that even the transient population of the open conformational state may play a role in the catalytic cycle. We attempted to crystallize these mutants in different space groups by varying experimental conditions of crystal growth (temperature, pH, salt content, additives, etc.). Moreover, since I14G mutant crystallized in $P2_12_12$ space group, in which ternary complexes of WT *ec*DHFR crystallize in closed conformation, we attempted both macro

and microseeding of I14A with I14G crystals. Even though we obtained crystals with different cell dimensions and crystal morphologies, all of these crystals crystallized in the $P2_1$ space group. These results could indicate that these mutants do not readily adopt the closed conformational ensemble, as it was recently suggested for G121V mutant.[190] This could provide some explanation for the reduction in the hydride transfer rate constant for these mutants.

Reduction in the DAD observed for the mutants in comparison to WT is contradictory to the predictions based on our kinetic and MD results. There we observed that the reduction in the size of this hydrophobic residue results in the formation of the "steric" hole that allows for the nicotinamide ring to relax towards the residue 14, leading to longer DADs for the mutants. However, MD simulations also indicated that nicotinamide ring samples larger conformational space in the mutant structures, which reflected itself in an increase in the H-bond distance between the nicotinamide O7N and I5(N), which is consistent with the x-ray crystal structures (Figure 4.4). However, the decrease in the DAD that we observe for the mutant structures could be a result of the nicotinamide ring being able to sample larger conformational space, as it is not as tightly constrained in the active site.

4.3.1.3 Analysis of the normalized B-factors

One way to extract dynamic information from static picture of an X-ray structure is to calculate the temperature factor (B-factor) details that contain specifics regarding the electron density distribution around a particular atom and is associated with thermal motions present in the crystal before and after flash - freeze. However, B-factor distribution needs to be analyzed with care, as errors in the model could also lead to high B-factors. Rapid cooling of the crystals in the liquid nitrogen can trap different conformational states of the protein that exist at physiological temperature. Since data collection for the WT enzyme was performed at room temperature, WT structure shows

overall higher B-factors than mutant structures. WT structural model was subjected to isotropic B-factor refinement, while high-resolution for I14A mutant allowed for the anisotropic refinement of all non-hydrogen atoms of protein, while ligand atoms and solvent were subjected to isotropic B-factor refinement. I14V model was subjected to isotropic B factor refinement, however in order to generate the best structural model (lowest R factors), TLS parameters were used to model anisotropic displacements in the final rounds of the refinement.

We normalized the B-factors for the different enzymes because the data collection was performed at different temperatures, and since B-factors for each enzyme may be on different scales owing to the application of different refinement procedures. Comparison of the temperature factors of C_α atoms between the I14A and WT ternary structures indicates that same areas exhibit similar amount of disorder in both structures (flexible loops – M20, F-G, G-H; Figure 4.5), despite the collection at different temperature. In order to examine any possible differences in the flexibility of the $NADP^+$ molecule, especially in its nicotinamide-ribose moiety, we calculated normalized B-factors for every atom belonging to the molecule (Figure 4.5). The details regarding the normalization procedure are presented in Materials and Methods section.

Normalized B-factors of the $NADP^+$ molecule for I14A and I14V were compared only to open WT conformation (1RB2; Figure 4.5). No correlation between the size of the residue 14 and an increase in the normalized B-factors of the nicotinamide-ribose moiety is observed. Comparison of the normalized B-factors for all the protein atoms of molecule A between these three structures indicate that F-G loop exhibits higher flexibility in the mutants than in the WT (Figure 4.2 and Figure 4.7-4.8).

4.3.2 Crystal structure of the I14G *ec*DHFR.

Ternary complex with I14G *ec*DHFR crystallized in the $P2_12_12$ space group with a single monomer in the asymmetric unit. Comparable WT crystal structure (PDB ID 1RX2) crystallized in the same space group, $P2_12_12_1$, with the nonisomorphous unit cell parameters to I14G. In $P2_12_12_1$ space group WT crystallizes in the closed conformation, which has been proposed to be the representation of the reactive conformation. The rmsd fit between backbone atoms of I14G mutant and the wild type enzyme in its closed conformation is 0.28 Å. Table 4.1 summarizes the X-ray data collection and refinement. The difference in the number of fitted atoms between the two structures is a result of the alternative conformations observed for few surface residues. Moreover, parts of the F-G loop for I14G mutant were not modeled in due to sporadic electron density in those regions. OMIT maps were used when such structural features were in doubt.

4.3.2.1 $NADP^+$ cofactor binding, the architecture of the active site and the M20 loop conformation

Analysis of the F_o-F_c maps of the cofactor-binding region for the I14G mutant, after molecular replacement (with ligands removed), indicated that $NADP^+$ is bound. However, poor electron density for the nicotinamide-ribose moiety could not indicate if it is disordered in the active site, or if it is bound out of the active site and disordered in the solvent, or both (we modeled $NADP^+$ molecule in the active site; Figure 4.9). We generated iterative composite OMIT map in order to resolve this structure feature. The map suggests that there is no electron density either in the active site or outside of it that could be assigned to the nicotinamide ribose moiety (Figure 4.10). We also observed poor electron density for the M20 and F-G loops, two loops that are in direct contact with each other. Parts of the loops have been modeled in as suggested by iterative composite OMIT map (Figure 4.10). Previous structural studies on WT *ec*DHFR showed that the mobility of the M20 loop depends on the freedom of movement of the F-G loop. Detail

analysis of the isotropic temperature factors for different X-ray crystal structures of WT *ec*DHFR suggest changes in the protein flexibility during the catalytic cycle. More specifically, a variation between these structures is mostly in the M20 and F-G loops, which exhibit low B-factors when M20 loop is in the closed conformations, and higher B-factors in the occluded complexes. In the apo-enzyme crystal structure, poor electron density is observed for the M20 loop implying high motion of the loop. The disordered conformation of M20 loop has been observed only in the binary complex of the *ec*DHFR with MTX in $P2_12_12_1$ space group, and observed disorder probably results from time-averaged fluctuations between the occluded and closed conformations.[4] However, in neither structure F-G loop is disordered, as is the case for I14G ternary complex.

4.3.2.2 Analysis of the normalized B-factors

Analysis of the normalized B-factors for C_α atoms of the cofactor between the I14G and WT ternary structures indicates the high flexibility of the nicotinamide ring of $NADP^+$ (Figure 4.6). Recent kinetic and MD simulation results suggested that the decrease in the size of the residue 14 leads to new DAD populations with longer average DADs and wider distributions. This was most prominently observed for I14G mutant. Analysis of the normalized B-factors for three active site residues (D27, F31, I5) that are in direct contact with pterin ring indicates that mutations bared no effect on the environment around the pterin ring (Figure 4.11). This supports our initial hypothesis that the reduction in the size of the residue 14 will bear minimal effect on the environment around pterin ring. Analysis of the normalized B-factors for the three residues in direct contact with the nicotinamide ring (Y100, residue 14, A7) shows a correlation between the size of the normalized B-factors, for residue 14 and A7, and the size of the "steric hole" behind the nicotinamide ring (Figure 4.11). This is in accord with the MD simulation results that showed that the hydrogen bond between nicotinamide(O7N) and A7(N) increases with a decrease in the size of the residue 14, and in one of the

populations observed for I14G mutant it is completely broken. This loss in rigidity is reflected in higher normalized B-factors for A7.

4.4 Conclusion

The kinetic analysis on the series of active site mutants of residue 14 (i.e., I14V, A, G) shows a change in the DAD population distribution at TRS for mutants.[85] MD simulation data indicated that mutations affect the enzyme's ability to organize the active site for hydride transfer. High-resolution structures for series of active-site mutants suggest some perturbations in ground state geometry and motions of certain active-site residues as well as two flexible loops. Moreover, the removal of steric bulk at position 14 could also lead to an increase in the flexibility of the nicotinamide ring. This has been previously observed for mutants of analogous residue in horse-liver alcohol dehydrogenase.[191] Inability to obtain closed conformation of the mutants could be a direct result of the mutations, which led to a shift in the relative populations of open and closed forms. This shift in the relative populations of open and closed forms may contribute to the reduced activity seen for the mutants. The high-resolution *ec*DHFR structures obtained for these mutants could be used for future simulation of hydride tunneling in *ec*DHFR by QM/MM computational methods.

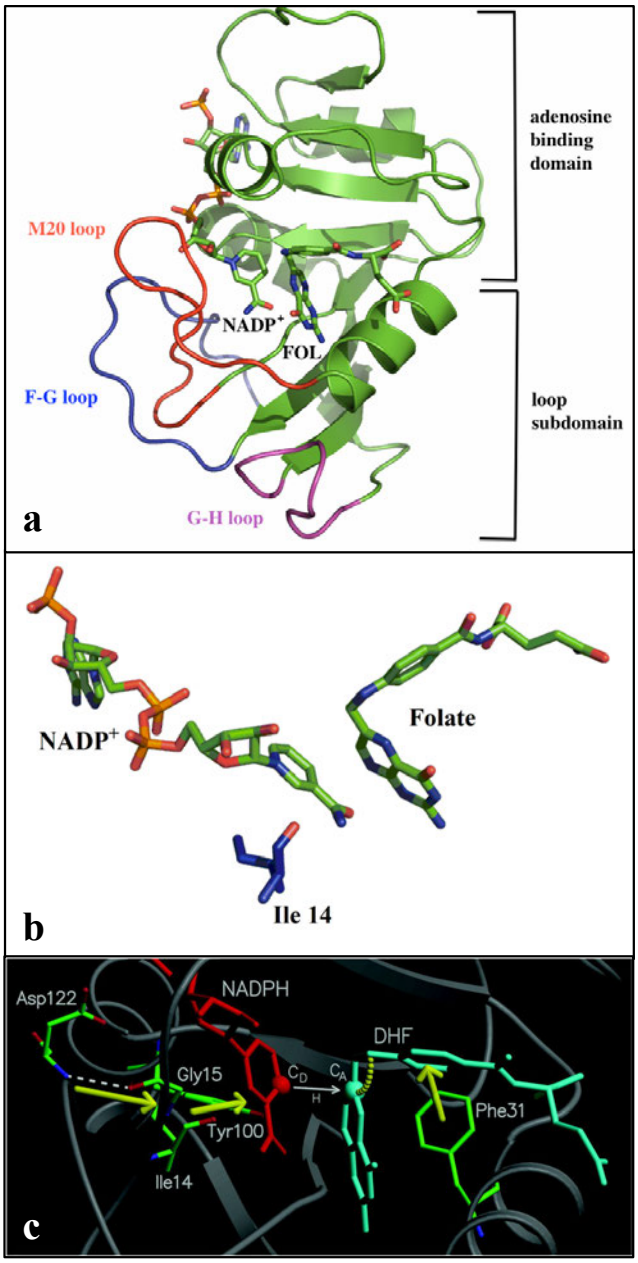

Figure 4.1 Structural details of *ec*DHFR. a) Structure of *ec*DHFR in complex with $NADP^+$ and folate crystallized in $P2_12_12_1$ space group (PDB ID 1RX2). Two subdomains are labeled together with three flexible loops. b) A graphic representation of the active site for WT *ec*DHFR with bound $NADP^+$ and folate (PDB ID 1RX2). The hydrophobic residue of interest is presented as sticks. c) Active site of DHFR with bound $NADP^+$ and folate. Several residues that have been identified as being part of the network of coupled promoting motions in *ec*DHFR are presented as sticks. The yellow arc and arrows indicate the coupled promoting motions. The figure is from ref [181].

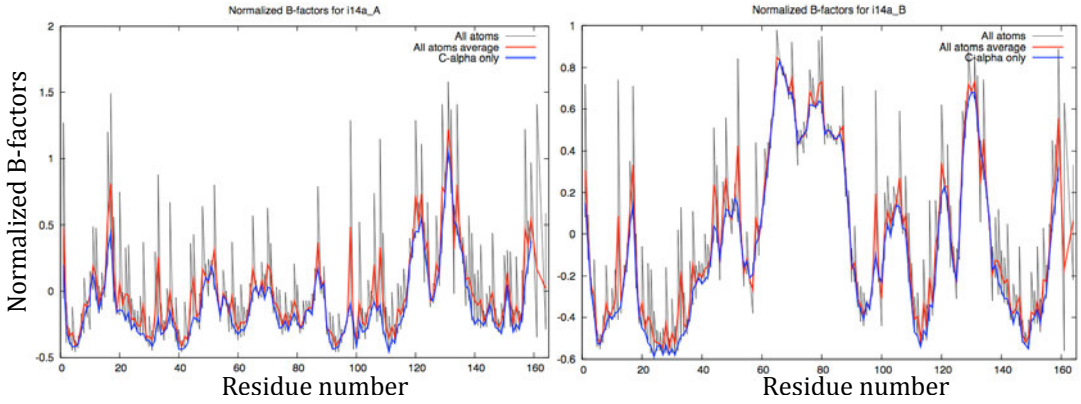

Figure 4.2 Comparison of the normalized B-factors for all the non-hydrogen atoms belonging to residues of the open I14A *ec*DHFR conformation. Residues of molecule A are presented on the left, and residues of molecule B are presented on the right.

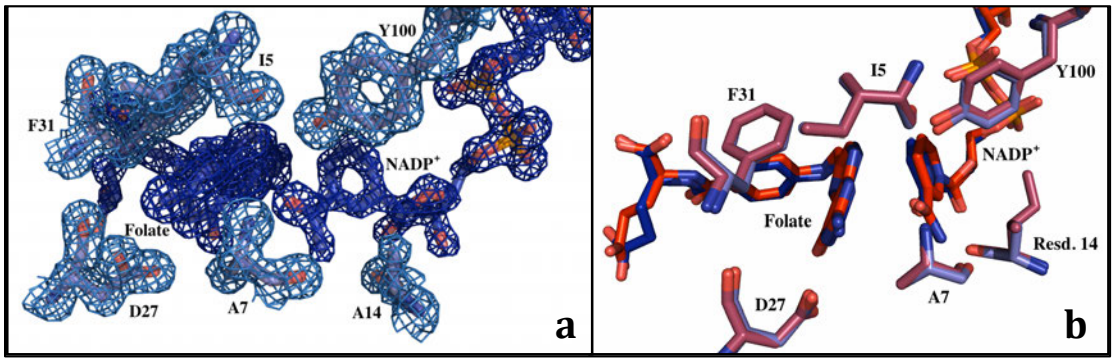

Figure 4.3 Structure of the active site for I14A *ec*DHFR. a) The $2F_o$-F_c maps of the substrate and cofactor binding regions of the I14A *ec*DHFR. The density corresponding to the bound folate, $NADP^+$ and several active-site residues is shown in dark blue and light blue, respectively. The maps are contoured at 1.5σ levels. b) Comparison of the active site structures of WT (PDB ID 1RB2; red) and I14A (blue) enzymes.

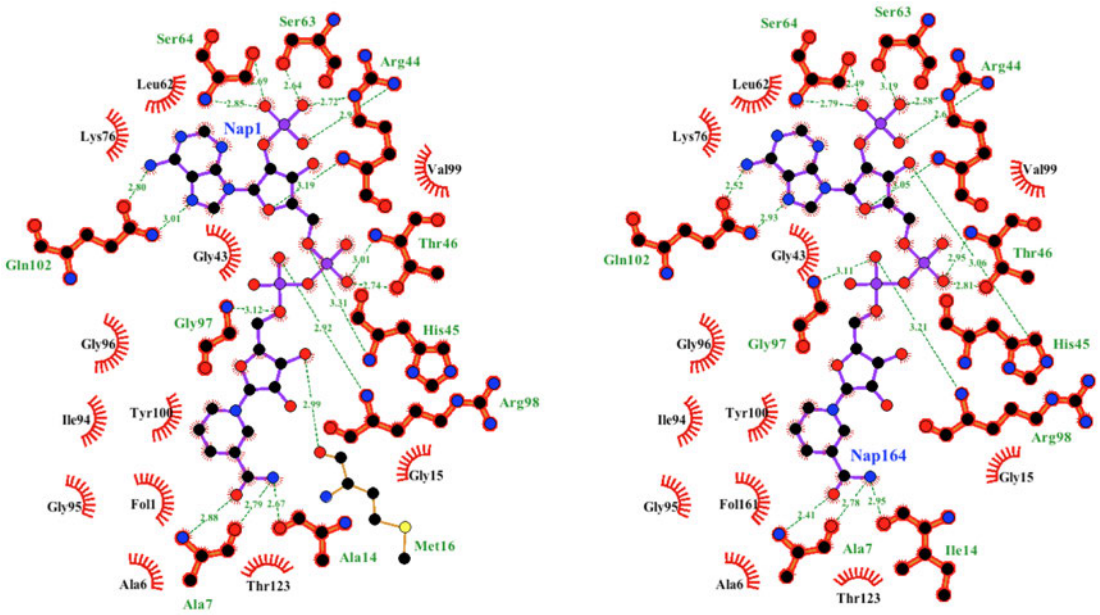

Figure 4.4 Interactions of $NADP^+$ with active site residues in I14A mutant (left) and WT (PDB ID 1RB2, right). Hydrogen bonds with their respective values are shown as dotted lines. The overlapping residues are highlighted. The figure was generated using LigPlus.

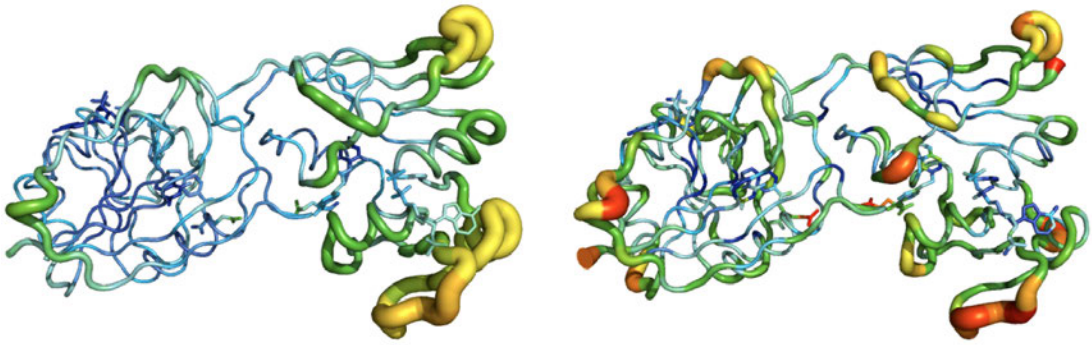

Figure 4.5 Putty cartoon of B-factor variation on the I14A (left) and WT (right) ternary structures, colored from low to high (blue to red).

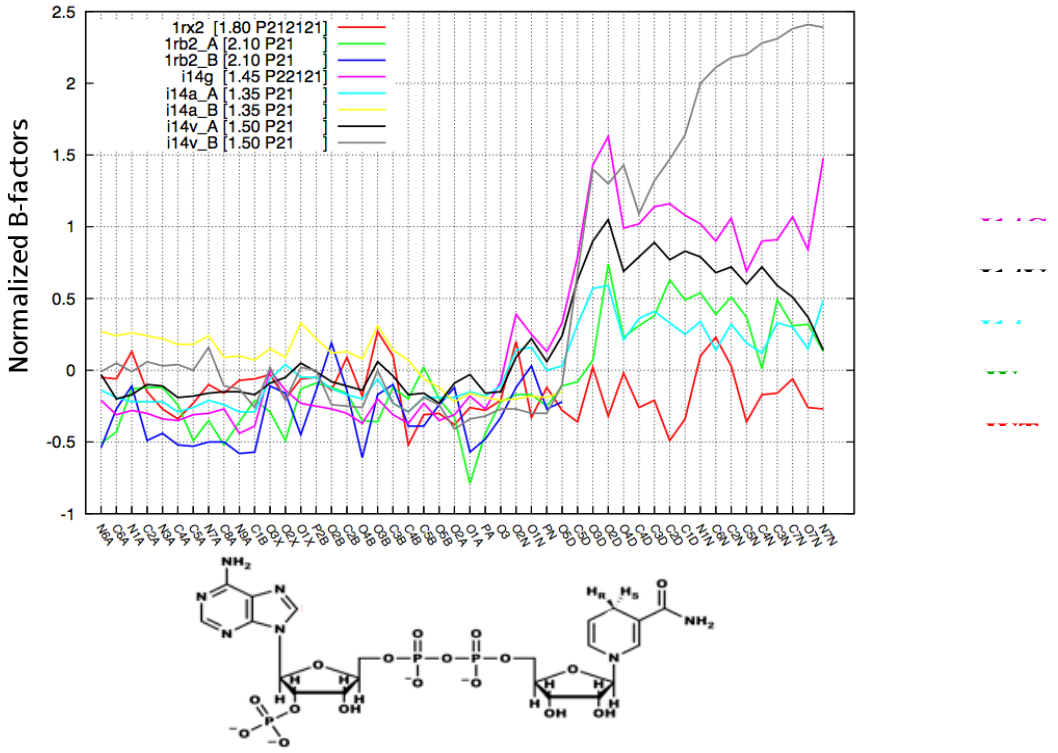

Figure 4.6 Comparison of the normalized B-factors for all the non-hydrogen atoms in the $NADP^+$ molecule starting from the adenine ring to the nicotinamide ring. Details about the normalization of the B-factors are presented in the materials and methods. Different colors are representation of normalized B-factors for different crystal structures in the following order: 1RX2 (WT *ec*DHFR, $P2_12_12_1$; red), 1RB2 (WT *ec*DHFR, $P2_1$; molecule A – green; molecule B – blue), I14A (molecule A - light blue; molecule B - yellow), I14V (molecule A – black; molecule B – grey), and I14G (purple). Since I14V and I14A crystallize as two molecules per asymmetric unit, we present the normalized B-factors for molecule A in which the nicotinamide ring of $NADP^+$ is bound in the active site.

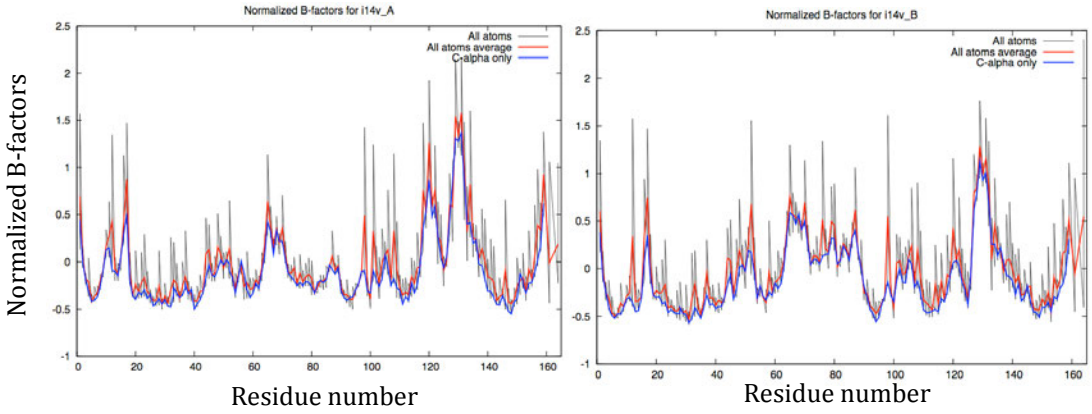

Figure 4.7 Comparison of the normalized B-factors for all the non-hydrogen atoms belonging to residues of the open I14V *ec*DHFR conformation. Residues of molecule A are presented on the left, and residues of molecule B are presented on the right.

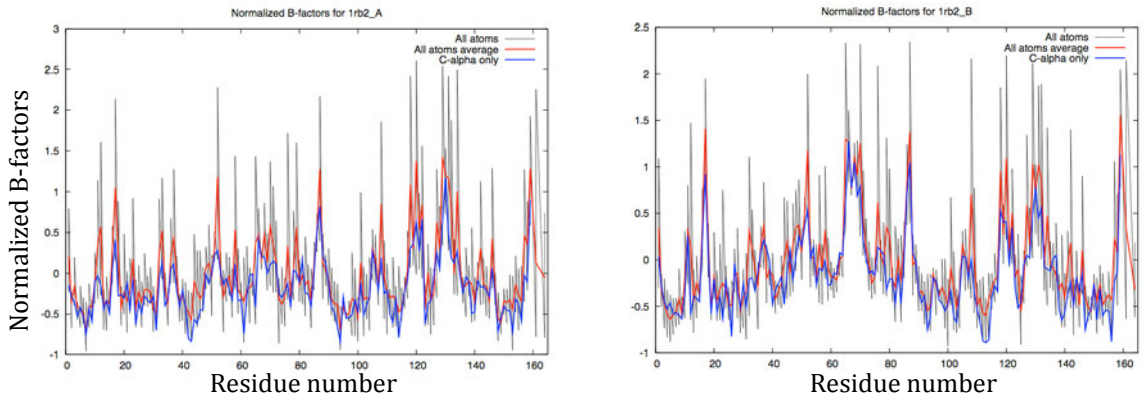

Figure 4.8 Comparison of the normalized B-factors for all the non-hydrogen atoms belonging to residues of the open WT *ec*DHFR conformation (PDB ID 1RB2). Residues of molecule A are presented on the left, and residues of molecule B are presented on the right.

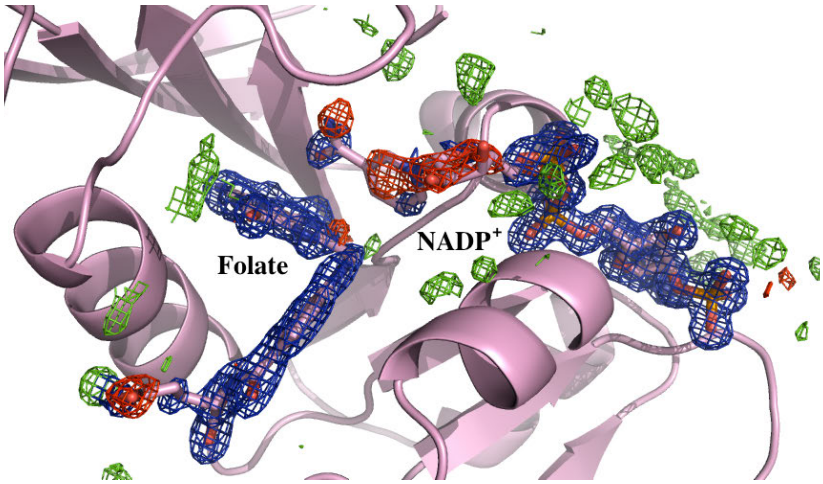

Figure 4.9 The $2F_o$-F_c maps of the substrate and cofactor binding regions of the I14G *ec*DHFR complexed with $NADP^+$ and folate. Maps are contoured in blue at 1.5σ levels. Difference maps are contoured in green and red at 3σ levels. Ligand models and protein backbone are shown in pink.

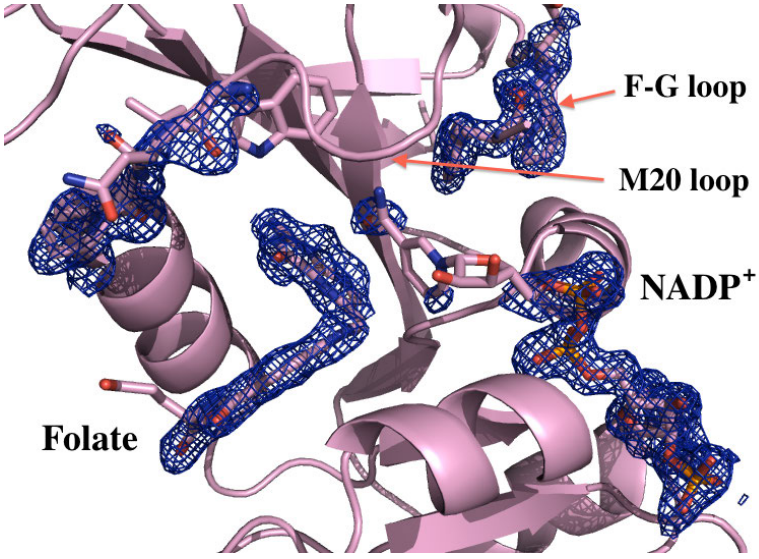

Figure 4.10 $2F_o$-F_c OMIT Fourier map for the I14G-Folate-$NADP^+$ ternary complex. The map is contoured at 1σ within 1.6 Å from the ligands and residues of M20 and F-G loop. No electron density is observed for either the side chains or backbone of residues A9-P20.

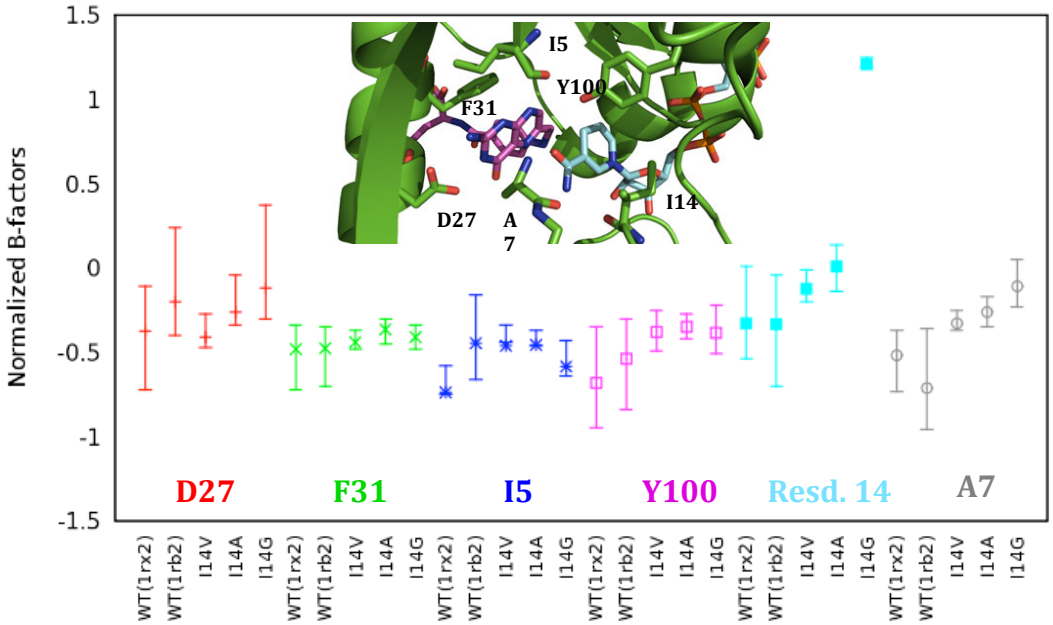

Figure 4.11 Comparison of normalized B-factors for several active-site residues in direct contact with either pterin ring of folate or nicotinamide ring of $NADP^+$. The inserted figure of the active site indicates the residues of interest. Their respective normalized B-factors are presented in the clockwise manner starting with D27. Correlation between an increase in the normalized B-factors and the reduction in the size of the residue 14 is clearly observed for A7, and is implied for Y100.

Table 4.1 Data collection and refinement statistics for I14V, I14A and I14G *ec*DHFR mutants.

	I14V DHFR	I14A DHFR	I14G DHFR
PDB ID	XXX	XXX	XXX
Data collection			
Source	ALS (LBNL) BeamLine 4.2.2		
Temperature (K)	100	100	100
Wavelenght (Å)	1.000	0.855	1.000
Space group	$P2_1$	$P2_1$	$P2_12_12$
Cell Dimensions			
a, b, c (Å)	35.08 60.25 74.18	35.12 59.51 74.23	33.49 34.44 134.25
a, b, g (˚)	90.00 95.97 90.00	90.00 95.53 90.00	90.00 90.00 90.00
Resolution (Å)	1.5	1.35	1.45
R_{merge}	0.040 (0.166)	0.031 (0.565)	0.048 (0.372)
<I/s(I)>	17.3 (3.6)	21.2 (2.3)	21.8 (3.6)
Completeness (%)	95.6 (89.7)	99.7 (100)	97.3 (84.3)
Multiplicity	3.86 (3.75)	3.7 (3.7)	6.5 (4.0)
Mosaicity (˚)	0.57	0.178	0.191
B factor from Wilson plot ($Å^2$)	17.9	13.8	12.2
Refinement			
Resolution Range (Å)	73.78-1.50	73.88-1.35	67.13-1.45
No. reflections	44649	63230	26211
No. unique reflections			
R_{work}/R_{free}	17.41/23.11	16.42/19.88	16.67/21.91
No. atoms			
Protein	2601	2630	1221
Ligand/ion	160	143	80
Water	496	352	162
B-factors			
Protein	22.50	20.6	18.5

Table 4.1 Continued

Ligand/ion	27.6	20.3	28.9
Water	19.8	30.6	30.6
R.m.s. deviations			
Bond lengths (Å)	0.029	0.015	0.025
Bond angles (°)	2.537	1.738	2.196
Ramachandran plot			
Favored (%)	98.76	100.00	98.03
Allowed (%)	1.24	0.00	1.97
Disallowed (%)	0.00	0.00	0.00

CHAPTER 5.
LOOKING ON THE OTHER SIDE: ROLE OF THE RESIDUE F31 IN THE DHFR CATALYZED HYDRIDE-TRANSFER[v]

5.1 Introduction

The role of the dynamical effects in assisting enzymatic reactions is quite complex and therefore still widely debated. It is now generally accepted that enzyme motions can play a significant role in different parts of reaction cycle such as substrate binding, product release, and large conformational changes necessary for the stabilization of the intermediates. These dynamical changes occur over different timescales ranging from the domain motions (seconds) to bond vibrations (femtoseconds). Due to complexity of enzyme dynamics, it is quite challenging to examine the dynamic contributions to the enzyme catalyzed reaction. Subpicosecond vibrational modes that may cause transient compression along the reaction coordinate in H-transfer reactions have been studied on different enzymatic systems such as: morphinone reductase,[66,163,192] dihydrofolate reductase,[1,84,85,193] yeast alcohol dehydrogenase,[72,194] horse-liver alcohol dehydrogenase,[39,195] formate dehydrogenase,[87] and more. Such motions are believed to compress the reaction barrier and lead to degeneration of the donor and acceptor's energy levels, therefore enhancing both quantum mechanical (QM) tunneling probability of the transferred hydrogen, and over-the-barrier transfer. Due to experimental limitations in probing such motions, their role has been usually inferred indirectly through measurement of pressure/temperature dependence of kinetic isotope effects (KIEs), by molecular dynamic (MD) simulations, or by quantum-mechanical/molecular mechanics (QM/MM) calculations. However, recent advances in the two-dimensional infrared

[v] This chapter is in preparation to be submitted to the journal of *Biochemistry*

spectroscopy (2D-IR) allowed for an experimental way to measure the femto- to picosecond timescale motions;[125] ^{1}H-^{15}N heteronuclear NOE can also provide some information about these fast timescale motions.[1,5,179]

The analysis of the temperature dependence motivated the development of various phenomenological models denoted here as Marcus-like models. For more in-depth discussion on these models please refer to following publications: [39,44,57,65,66,73,85,89,125,127,173-177,196]. In short, according to this model, after the formation of the reactive complex (a process sometimes referred to as preorganization), heavy-atom motions are necessary to bring the system to a point where donor and acceptor wells are degenerate and hydrogen tunneling is plausible (i.e. tunneling ready state, TRS).[39,58,62,72,74,116,118,120,127,174] This process is often referred to as reorganization, as it assists the structural changes in the substrate that occur as the reaction proceeds from ground state to TRS. At the TRS, fluctuations in the donor-acceptor distance (DAD_e) [vi] affect the tunneling probability, and therefore will be a determinant factor of the magnitude and the temperature dependence of the KIEs. Certain QM/MM calculations support this view and suggest that temperature dependence/independence of the intrinsic KIEs mainly reflects the temperature dependence of DAD.[51,59,197,198] According to Marcus-like models, temperature independent KIEs observed for majority of the wild-type (WT) enzymes[68,83,87,120,123,199-201] indicate systems wherein the active-site at the TRS is optimal for H-tunneling with a short average DAD_e and narrow DAD distribution. These models suggest that shorter DAD_e decreases the KIE, and broader DAD_e distribution (lower DAD_e-fluctuations frequency) leads to elevated ΔE_a (more temperature dependent KIEs). However, certain experimental and computational studies have also shown that compression of DAD_c

[vi] DAD_e here refers to the distance from the H-reactant state to the H-product state, rather than to the distance between two carbons - donor and acceptor distance (DAD_c). The first directly reflects the kinetic and energetic effects of the H-transfer, while the second reflects the heavy atoms conformation as observed in the x-ray crystal structures and MD simulations. For example, for a linear C-H-C transfer $DAD_c = DAD_e + 2$ x C-H distance.

alone might not increase the hydride transfer rate and/or decrease the barrier height, or that a decrease in the DAD_c needs to necessarily lead to a decrease in tunneling.[200,202-204]

Here, we report kinetic, structural and MD simulation studies on the impact of the active-site mutation on the hydride transfer reaction in dihydrofolate reductase from *Escherichia coli* (*ec*DHFR). *Ec*DHFR is a small, monomeric enzyme that catalyzes the transfer of the pro-*R*-hydride from the C4 position of NADPH to the *re*-face of C6 position on 7,8-dihydrofolate (H_2F) to produce *S*-5,6,7,8-tertrahydrofolate (H_4F). The hydride transfer in *ec*DHFR has been well characterized, with both experimental and computational studies suggesting that thermally activated fluctuations of the DAD are important in assisting hydride transfer.[63,83-85,198,205]The study on a series of active site mutants of residue 14, situated behind the nicotinamide ring, showed an increase in the temperature dependence of the KIEs (ΔE_a) with a decrease in the size of this active site residue.[85] One of roles of this highly conserved residue was suggested to be in assisting the hydride transfer by keeping the nicotinamide ring in the close proximity to the pterin ring, i.e., restricting the DAD to short and narrow conformational space in the WT enzyme. Another residue of similar interest is F31, a strictly conserved hydrophobic residue,[206] located behind the pterin ring of H_2F (H-acceptor), opposite from residue 14 (Figure 5.1). It interacts with the pteroyl moiety of H_2F through van der Waals contacts with the edge of the phenyl ring toward faces of both the pterin ring and p-aminobenzoyl group.[207] As evident from the Figure 1, in contrast to I14, which only interacts with the nicotinamide ring of $NADP^+$, folate is "wrapped around" F31, which seems to anchor all three moieties of the substrate (pteryl, *p*-aminobenzoyl, and glutamyl). Residue F31 has been shown to be very important for both the binding of the H_2F as well as catalyzed reaction.[208] The importance of hydrophobic interactions in binding of drugs, such as methotrexate (MTX) and 2,4-diamino-6,7-dimethylpteridine (DAM), has been shown previously, where F31V mutation lead to 140-fold decrease in the binding constant for

MTX,[207] as well as 30-fold decrease in the binding constant of the H_2F (Table 5.1 and refs [207-209]).

QM/MM calculations suggested that residue F31 belongs to a network of coupled promoting motions.[18,181] More specifically, it was shown that as reaction evolves from the reactant to the transition state, residue 31 moves closer to the substrate, while the angle between the acceptor carbon and the methylene amino linkage in H_2F increases and the DAD_c decreases. Based on these experimental and computational studies on *ec*DHFR, as well as relevant studies of active site mutants in other enzymes,[66,123,134,210] we decided to extend our initial study on the residue I14 to F31V mutant. We examined the effect of this mutation on the nature of the hydride transfer by measuring the temperature dependence of the intrinsic KIEs, by obtaining X-ray crystal structures of the relevant ternary complex, and by performing MD simulations.

5.2 Materials and methods

5.2.1 Construction of expression vector.

The sequence of the mutagenic, forward primer (F31V-Fwrd) is 5'- GCC-GAT-CTC-GCC-TGG-GTT-AAA-CGC-AAC-ACC-3', and the sequence of the mutagenic, reverse primer (F31V-Rev) is 5'- GGT-GTT-GCG-TTT-AAC-CCA-GGC-GAG-ATC-GGC-3', where the site of the mutation is underlined. Site-directed mutagenesis was completed using pET22b-WT*ec*DHFR as a template and following the protocol provided in the Stratagene instruction manual. The sequence of the final plasmid, containing the desired mutation, was verified with automated DNA sequencing through the DNA facility-University of Iowa. Primers were purchased from Integrated DNA Technologies.

Expression and Purification of F31V DHFR. The mutant was expressed in the E.coli strain ER2566, which contains a deletion of the DHFR gene (folA) and thymidylate synthase (thyA), and was a generous gift from S. J. Benkovic at the Penn

State University (University Park, PA). The enzyme was purified and stored as reported for other DHFR mutants.[106]

5.2.2 Preparation of F31V DHFR ternary complexes for crystallization.

Purified protein was either stored at -80°C until further use, or loaded onto a Superdex-75 (GE) gel filtration column pre-equilibrated with the buffer containing 20 mM Tris-HCl, pH 7.5. DHFR eluted in a single peak, which was tested for the monodispersity using dynamic light scattering on the NanoStar (Wyatt Technology).

Concentration of the pooled fractions was measured using UV absorbance (ε_{280}=74.6 $mM^{-1}cm^{-1}$) and Bradford assay. Due to the low solubility of folate and ~20-fold higher $K_{d(folate)}$ for F31V DHFR than for the WT *ec*DHFR, folate was added to a dilute protein solution at ~10 fold molar excess relative to F31V DHFR mutant. The sample was then incubated on ice for at least 1 hour, and afterwards filtered using Milipore 0.22um filter. Lastly, the binary complex was concentrated to a final concentration of ~15 mg/ml (as determined by Bradford assay). $NADP^+$ was added as a solid to the concentrated binary DHFR-Folate complex at a five-fold molar excess to enzyme. Preparation of ternary complex with MTX and $NADP^+$ was performed in the same manner as for the enzyme-Folate-$NADP^+$ complex, however no filtering was done prior to concentrating the enzyme-MTX binary complex.

5.2.3 Crystallization conditions.

Both enzyme-Folate-$NADP^+$ and enzyme-MTX-$NADP^+$ ternary complexes were crystallized via the hanging drop vapor diffusion method by mixing 400 nl well solution and 400 nl of prepared ternary complex using TTP LabTech Mosquito. In more detail:

F31V-$NADP^+$-Folate ternary complex crystallized in the $P2_1$ space group with two molecules in the asymmetric unit, under the following conditions: 15 mg/ml F31V DHFR, 0.1M Tris pH 8.5, 0.5M LiCl and 30.5% w/v PEG 6,000; at 18°C.

F31V-$NADP^+$ binary complex crystallized in the $P2_1$ space group with two molecules in the asymmetric unit, under the following conditions: 13.5 mg/ml F31V DHFR, 0.1 M HEPES pH 7.5, 25% w/v PEG 6,000; at 18˚C. This crystal was a result of the failed attempt to obtain the ternary F31V-$NADP^+$-Folate complex.

F31V-$NADP^+$-MTX ternary complex crystallized in the $P2_12_12_1$ space group with two molecules in the asymmetric unit, under the following conditions: 16 mg/ml F31V DHFR, 0.1 M Bis-Tris propane pH 6.5, 20% w/v PEG 3,350, 0.2 M sodium acetate anhydrous; at 18˚C. Crystal initially appeared after 10 days, but was harvested after 3 weeks.

5.2.4 Data collection and structure determination.

Crystals were flashed-cooled in liquid nitrogen, and data were collected at 100 K at the 4.2.2 synchotron beamline at the Advance Light Source of the Lawrence Berkley National Laboratory. The data were either processed using d*Trek (for F31V-MTX-$NADP^+$),[183] mosflm (for F31V-$NADP^+$),[211] or XDS (for F31V-Folate-$NADP^+$).[184] We faced initial difficulties in processing the data for the F31V-MTX-$NADP^+$ complex due to multiple lattices being present in the crystal (partially reflected in the mosaicity; Table 5.3), and the twinning of the crystal. Initial refinement indicated $P4_32_12$ space group, with single molecule present in the asymmetric unit; however, further rounds of refinement did not yield a model with desirable statistics for a structure of this resolution. Analysis of the data with Xtriage indicated significant twinning and Zanuda suggested $P2_12_12_1$ space group, whose unit cell parameters are very similar and close to be considered as $P4_32_12$ space group.

The structures were determined by molecular replacement in CCP4[185] (with PHASER[186]), using the coordinates for the refined WT *ec*DHFR structure (PDB 1RX2) with ligands removed to generate the initial model. Refinement and model building were done using REFMAC[187] and COOT[188]. Model bias was avoided during the initial refinement by removing the substrate and cofactor from the model. Moreover, iterative composite OMIT maps were used for the F31V-MTX-$NADP^+$ complex where structure features were in doubt. In all structures hydrogens were included in riding positions, and isotopic temperature factors were refined. Alternative conformations of amino acids and cofactor were assigned on the basis of the visual evidence such as divergent electron densities at the $+1\sigma$ level above the average in $2|F_o|-|F_c|$ maps, and from either simple composite OMIT maps or iterative composite OMIT maps. The final models were well described by the electron density maps. However, side chains of the certain residues situated on the surface of the protein (in most cases lysine, arginine and glutamic acid residues) were not well described by density. These side chains were not deleted, but were left with their occupancies equal to one, with temperature factors reflecting their disorder. Final structures were checked with MolProbity.[212] All residues have favored or allowed backbone conformational angles. Several residues occupy unusual rotameric states, however, clear and strong electron densities are in support of such positions. Data and final refinement statistics are given in Table 5.3.

5.2.5 Synthesis of Labeled Cofactors for 1˚KIEs.

[Ad-^{14}C]-NAD^+ (specific radioactivity of >220mCi/mmol) was purchased from Amersham Pharmacia, glucose dehydrogenase from *Bacillus megaterium* (GluDH) was obtained from Affymetrix/USB, while all the other compounds were purchased from Sigma. Synthesis, purification and storage of the labeled cofactors have been presented in detail before.[95,111] Briefly: (*R*)-[4-^{3}H]NADPH (680 mCi/mmol) was synthesized by

reduction of $NADP^+$ with 2-Deoxy-D-Glucose-^3H using glucose dehydrogenase from *Bacillus megaterium* (GluDH), followed by oxidation of the resulting NADPH with acetone using alcohol dehydrogenase from *Thermoanaerobium brockii* (*tb*ADH), and final reduction using GluDH and unlabeled glucose, as described previously.[111] [Ad-^{14}C]-NADPH (50mCi/mmol) was prepared by phosphorylation of [Ad-^{14}C]-NAD^+ using NAD^+ kinase from chicken liver to produce [Ad-^{14}C]-$NADP^+$, followed by reduction with glucose using GluDH as described elsewhere.[95] (*R*)-[Ad-^{14}C,4-^2H]-NADPH (50 mCi/mmol) was prepared from [Ad-^{14}C]-$NADP^+$, which was synthesized as described above, and subsequent reduction with deuterated glucose and GluDH.[142] All synthesized cofactors have been purified by semipreparative reverse-phase HPLC on a Supelco column and stored at -80 ˚C prior to use as discussed elsewhere.[109]

5.2.6 Kinetic isotope effect measurements and determination of the intrinsic KIEs.

(*R*)-[4-^3H]NADPH and [Ad-^{14}C]-NADPH, and, (*R*)-[4-^3H]NADPH and (*R*)-[Ad-^{14}C,4-^2H]-NADPH were combined in the 5:1 radioactivity ratio in order to measure H/T and D/T 1˚KIEs, respectively. Each mixture was co-purified on an analytical reverse-phase HPLC column, divided into aliquots containing 300,000 dpm of ^{14}C, and frozen in liquid nitrogen for short-term storage at -80 ˚C. All experiments were performed in MTEN buffer (50 mM MES, 25 mM Tris, 25 mM ethanolamine and 100 mM NaCl) at pH=9.0 over the 5-45 ˚C temperature range. All reaction mixtures contained around 400-fold excess of H_2F (1.7 mM) over NADPH (4 μM). The reactions were quenched by adding an excess of methotrexate (K_d=1 nM), and samples were stored on dry ice prior to HPLC analysis[103]. Before the HPLC-LSC analysis, samples were thawed and bubbled with oxygen to ensure complete oxidation of the product H_4F. The samples were then

separated by reverse-phase HPLC using a method described elsewhere.[109] The observed KIEs were calculated according to ref. [29] using the following equation:

$$KIE = \frac{\ln(1 - f)}{\ln[1 - f(\frac{R_t}{R_\infty})]}$$

where the fractional conversion (f) was determined from the ratio of ^{14}C in the product and reactant, and R_t and R_∞ are the ratio $^3H/^{14}C$ at each time point and at infinite time, respectively. The intrinsic KIEs were calculated using the modified Northrop equation[35,74]

$$\frac{^T(\frac{V}{K})^{-1}_{H_{obs}} - 1}{^T(\frac{V}{K})^{-1}_{D_{obs}} - 1} = \frac{(k_H / k_T)^{-1} - 1}{(k_H / k_T)^{-1/3.34} - 1}$$

where $^T(V/K)_{Hobs}$ and $^T(V/K)_{Dobs}$ are the observed H/T and D/T KIEs, respectively, and k_H/k_T represents the intrinsic H/T KIE. The intrinsic KIEs were calculated numerically from all possible combinations of observed H/T and D/T values. The isotope effects on the activation parameters for the intrinsic KIEs were calculated by a nonlinear fit of all intrinsic values to the Arrhenius equation for KIEs:

$$k_l / k_h = A_l / A_h \bullet e^{\Delta E_{a_{h-l}}/RT}$$

where k_l and k_h are the rate constants for light and heavy isotopes, respectively, A_l/A_h is the isotope effect on the Arrhenius preexponential factor, $\Delta E_{a\ h\text{-}l}$ is the difference in energy of activation between the two isotopic reactions, R is the gas constant and T is the absolute temperature.

5.2.7 Presteady-state kinetics.

All kinetic measurements were obtained on a stopped-flow apparatus (Applied Photophysics Ltd., Leatherhead, U.K.), with dead time of 1.6 ms, a 2-mm path length,

and a thermally regulated sample cell. The enzyme reaction was monitored by taking advantage of fluorescent resonance energy transfer (FRET) between DHFR and NADPH.[6] Enzyme tryptophans were excited at 290 nm, and FRET results in the strong fluorescence by the reduced cofactor at 450 nm, which is observed through a 390 nm output filter. All experiments were carried out at 25˚C and pH=7 in a 1x MTEN buffer. The concentrations of substrates were determined spectrophotometrically by using the extinction coefficients of 6200 M^{-1} cm^{-1} at 340 nm (for NADPH), and 28000 $M^{-1}cm^{-1}$ at 282 nm (for H_2F). In the experiment, 20 μM enzyme (either wtDHFR or the F31V mutant) was preincubated with NADPH (10 μM) in MTEN buffer at 25˚C. The reaction was initiated by rapid mixing with 300 μM H_2F. We used the average of at least five runs from three independent experiments for data analysis. All data were analyzed by non-linear least squares fits to single exponential function using KaleidaGraph 3.5.

5.2.8 Determination of temperature stability using dynamic light scattering (DLS)

Melting temperatures (T_m) were determined for each of the enzyme-folate complexes. WT and F31V *ec*DHFRs were purified using previously published protocol,[137] concentrated to ~ 10-15 mg/ml and stored either as an apoenzyme at -80 °C or as a binary complex with folate at -20 °C. Prior to T_m measurements, ~2ml of either sample was thawed on ice. Sample was purified on the Superdex-75 (GE) gel filtration column pre-equilibrated with the buffer containing 20 mM Tris-HCl, pH 7.5. Fractions containing pure enzyme were pooled together, concentrated to ~1-10 mg/ml, spun down for 10 min at 10,000 rpm and 4 ˚C, and filtered using 0.02 μm Whatman filter. The final concentration was determined spectrophotometrically (ε_{280nm} = 74.6 $mM^{-1}cm^{-1}$) and was at least 1.0 mg/ml, equivalent to 55 μM as a monomer. The measurements were performed at temperatures from 35 to 80˚C at a scan rate of 1.0 ˚C/min. Size distributions

were measured with a Dynapro Nanostar (Wyatt Technology Malvern Instruments, USA), based on DLS. The particle distribution from DLS measurements was derived by deconvolution of the measured intensity autocorrelation function of the sample. Generally, deconvolution was accomplished using a non-negatively constrained least squares (NNLS) fitting algorithm included in the Dynamics software. The z-average molecular "size" in terms of the hydrodynamic diameter (d_H) in solution was determined. The viscosity of the buffer used was calculated using a solvent builder interface and takes the effects of buffer salts into account. For both F31V mutant and the WT *ec*DHFR the hydrodynamic radii exhibited a sigmoid relationship as a function of temperature. We used Dynamics program for fitting in order to obtain temperature and radius at the inflection point of the sigmoidal curve.

5.2.9 Numerical modeling

The numerical modeling was based on the Kuznetsov and Ulstrup model for adiabatic H-transfer reactions,[57] but with significant modifications relative to other attempts to implement this type of model. The model and its implementation have been described previously,[73] and a simple program that can fit and explain any level of temperature dependence of KIE is available free of charge at http://chemmath.chem.uiowa.edu/webMathematica/kohen/marcuslikemodel.html

5.2.10 MD simulations.

MD simulations on F31V DHFR were performed using the Amber9 package[213], as it was previously done for active site mutants of residue I14.[85] Details regarding the system setup, ligand parameterization, MD runs, data fitting and analysis are presented in ref [85]. Briefly, all ten 6 ns simulations were run starting from the crystal structure of wtDHFR in complex with folate and $NADP^+$ (PDB entry 1RX2).[144,213] The folate and

$NADP^+$ ligands were replaced by N5 protonated 7,8-dihydrofolate (H_2F) and NADPH respectively. The protonation state for all ionizable residues was set corresponding to pH 7, and the final protein structure was solvated with a previously equilibrated truncated octahedron box of TIP3P water molecules. The size of the box ensures that all protein atoms are at least 9 Å away from the edges of the box. Subsequent mutations were performed *in silico* by changing the corresponding amino acid in the original structure. During the simulations AMBER99 force field[154] parameters were used for all residues. The $NADP^+$ and NADPH parameters were taken from the Amber parameter database.[155] Gaff force field[156] parameters together with RESP[157] charges calculated at the HF/6-31G* level were used to generate the parameter files for H_2F. All simulations were run with the PMEMD module of the AMBER9 package.[144,213] An equilibration protocol was applied that consists of performing an initial energy minimization, followed by a slow heating to the desired temperature using a linear temperature ramp from 100 to 300 K during 80 ps at constant volume and a subsequent pressure stabilization run at 300 K and 1 bar over 100 ps. Position frames, which were used for analyzing trajectories, were collected at 2 ps intervals. The ptraj module of Amber9 was used to analyze the data extracted from the MD simulations. Data from the DAD_c distribution were fitted with a combination of Gaussian and Split Gaussian functions using the open source software for non linear curve fitting, Fityk.[162] For the equations and procedures used for the fitting please refer to the Chapter 3.

5.3 Results and Discussion

5.3.1 Temperature dependence of intrinsic KIEs for F31V DHFR; isotope effects on activation Arrhenius parameters and thermal stability of F31V vs. WT

We measured 1˚ H/T and D/T KIEs on the second order rate constant, k_{cat}/K_M, with F31V *ec*DHFR in 5-45 ˚C temperature range as previously described for WT[83] and other *ec*DHFR's mutants. [85,103,141] The intrinsic values were calculated using modified Northrop equation,[20,104] and fitted to the Arrhenius equation in order to obtain the isotope effect on the activation energy and the Arrhenius pre-exponential factors (Figure 5.2A). Table 5.1 summarizes kinetic and binding parameters for the WT *ec*DHFR and relevant active site mutants, i.e., I14 and F31.

The KIE on the hydride transfer of F31V shows a biphasic behavior, which suggests an intrinsic phase transition at 35 ˚C or a change in mechanism. A break in the temperature dependence of the intrinsic KIEs has not been previously observed for mutants of *ec*DHFR, however it has been observed for several thermophilic enzymes,[90,210] as well as for certain mutants of mesophilic enzymes such as thymidylate synthase.[201] Due to this break in the temperature dependence of intrinsic KIEs for F31V, the data were fitted in temperature ranges 45-35 ˚C and 35-5 ˚C independently. Above the 35 ˚C, KIEs are temperature-independent with a larger magnitude in comparison to WT enzyme, resulting in also a larger isotope effect on the Arrhenius pre-exponential parameter, suggesting that F31V-catalyzed hydride transfer occurs predominately via quantum mechanical tunneling, as it is the case for WT (Figure 5.2A).[83] According to Marcus-like models, this trend would suggest that the average DAD (DAD_{ave}) at the TRS, above 35˚C, is longer than for the WT, reflecting itself in the size of the intrinsic KIEs. However, reorganization of the active site still allows the system to reach a well-

defined TRS, which is characterized by a short and narrow DAD distribution, as evident from the temperature independent KIEs.

In contrast, below 35 ˚C, intrinsic KIEs were temperature-dependent, and as a consequence the isotope effect on the Arrhenius pre-exponential factor was inverse and below the semi-classical limit.[29] Such a steep temperature dependence of KIEs resemble that of I14G *ec*DHFR,[85] suggesting that the structural and dynamic properties of F31V (*i.e.*, the DAD distribution at the TRS) reflect those of I14G. In other words, the heavy atom reorganization does not bring the system to an optimal TRS, and therefore thermally activated fluctuations allow the system to sample shorter DADs at higher temperatures, resulting in temperature dependent KIEs.

In order to quantitatively link the size and temperature dependence of the KIEs to the population distribution along the DAD coordinate, we fitted the data to a simple phenomenological model with two adjustable parameters, which is equivalent to number of parameters one obtains from fitting to Arrhenius equation.[73] These parameters are, in our minds, more physically meaningful than Arrhenius parameters, since the data are described in the terms of the distribution of the DADs. This simple fitting model has been recently used to explain the temperature-dependence of KIEs for various enzymatic systems, including DHFR.[73] It is important to note that similar procedures for fitting experimental data to Marcus-like models have been developed by others,[66-68,123] however those models were more complex, system specific and required larger number of parameters and thus fitted data with lower statistical confidence. The model used here for comparison of various *ec*DHFRs assumes adiabatic hydrogen tunneling.[73] In this model, 1˚ KIEs are presented by the following ratio of integrals:

$$KIE = \frac{k_L}{k_H} = \frac{\int_0^\infty \gamma(m_L, DAD_e) e^{E(DAD_e)/k_B T}\, dDAD_e}{\int_0^\infty \gamma(m_H, DAD_e) e^{E(DAD_e)/k_B T}\, dDAD_e} \qquad [1]$$

where the first factor in the integral represents the probability of tunneling as a function of the DAD_e and the mass of the particle (m_L and m_H represent the mass of the light and heavy isotope respectively). The second integrated term represents a Boltzmann distribution of DAD_e. The whole expression is integrated over all possible DADs. For more details please refer to ref [73]. For systems that exhibit either little or moderate temperature dependence of the KIEs, the data are fitted to a model with a single DAD population, where the DAD_{ave} and force constant of the corresponding harmonic DAD potential are adjustable fitting parameters. For F31V, this type of distribution is suitable to describe KIE data above 35 ˚C (Table 5.2). This simple distribution fails in the case of the steep temperature dependence of KIEs, *i.e.* below 35 ˚C for F31V, as it was the case for the I14G *ec*DHFR. Therefore, in the situation where donor and acceptor are not well constrained at the TRS, a model with two distinct populations, describing a broader DAD's distribution, is implemented to fit the experimental data. For that model, the first population is not isotopically sensitive since it is centered at some arbitrary short DAD where the zero point energies for all the isotopes are above the barrier. Due to the short distance, below van der Walls radius, that ensemble of conformations is of high energy and quite small. A second, lower-energy population, centered at the longer DAD_c (first fitting parameter), is more stable and populated and where H-tunneling depends on the mass of the isotope. These two populations are in thermal equilibrium (Boltzmann distribution), and the difference in free energy between the two populations is the second parameter of the regression, ΔG. This model provides a good fit to the KIE data below the 35 ˚C. Table 5.2 summarizes all the fitting parameters for F31V mutant as well as for active site mutants of I14 and the WT. The results of the single population above the 35 ˚C suggest that even though DAD_{ave} for the F31V mutant is just slightly larger than for the WT, the force constant for the DAD potential is smaller suggesting a larger DAD distribution at TRS. However, the mutation from the large phenylalanine to valine could create a "steric hole" opening behind the dihydropterin ring of the H_2F allowing for the

substrate to adopt different conformations. The large temperature dependence of the KIEs below 35 ˚C suggest that at lower temperatures F31V is trapped in the conformational space where most of the DAD_c conformations are much longer that above 35 ˚C. The fitting to the two-population model suggests that the average DAD_c is significantly longer for the F31V in comparison to WT. For temperatures below 35 ˚C, a comparison between F31V and I14G reveals smaller ΔG and shorter average DAD_c for F31V mutant, which is in accordance with its smaller ΔE_a (as reflected in its lower temperature dependence of KIEs).

Similar biphasic behavior of the intrinsic KIEs has been previously reported for several enzymatic systems, which also exhibited faster rate constants at higher temperatures.[90,201] In contrast, for F31V we observed an estimated 4 fold reduction in enzyme activity above 35 ˚C. It is quite possible that the rate of the hydride transfer might be faster at 40 ˚C than at 35 ˚C, however temperature instability of the mutant protein could result in smaller fraction of reactive enzyme. However, despite the reduction in the total amount of the reactive enzyme that population appears to be well oriented for H-tunneling. In order to test this hypothesis we measured the melting temperature (T_m) using dynamic light scattering (DLS) technique.[214] The T_m determined for the enzyme-Folate binary complex was slightly lower for F31V than for the WT (52.0±0.2 and 55.8±0.3, respectively). The Dynamics program was used for data fitting in order to obtain temperature at the inflection point of the sigmoidal curve. These data are in accordance with the hypothesis that the F31V mutation has destabilizing effect on the enzyme, which may explain its behavior above 35 ˚C.

5.3.2 Commitment on the second order rate constant, k_{cat}/K_M

In most organic and enzymatic reactions, observed KIEs are smaller than their respective intrinsic values, since chemical step (bond cleavage) is not rate-limiting. As a consequence the chemical step is masked by other isotopically insensitive steps (i.e. substrates binding, product release, conformation changes, protonation changes, etc.), a term noted as kinetic complexity. This kinetic complexity for the KIEs obtained by competitive method, can be described by the following equation[102]

$$KIE_{obs} = \frac{KIE_{\text{int}} + C_f + C_r * EIE}{1 + C_f + C_r} \qquad (2)$$

where KIE_{obs} is the observed KIE, KIE_{int} is the intrinsic KIE, EIE is the equilibrium isotope effect, and C_f and C_r are the forward and reverse commitments, respectively. Under the experimental conditions of the DHFR reaction in the KIE experiment, $C_r \approx 0$ and EIE is close to unity so the equation 2 can be simplified to following equation:

$$KIE_{obs} = \frac{KIE_{\text{int}} + C_f}{1 + C_f} \qquad (3)$$

where C_f represent the sum of the ratios between the rate of the forward isotopically sensitive hydride-transfer step and each of the rate constants of the preceding backward isotopically insensitive steps.[102] We calculated the C_f values from all the possible combinations between the intrinsic and observed KIE values, and present their averages and standard deviations in the Figure 5.2B. Interestingly, in contrast to the WT, the forward commitment for F31V exhibits similar trend to that of its intrinsic KIEs, which explains why the observed KIEs presented the same breaking point but opposite temperature dependence under 35 ˚C (Table 5.4). Below the 35 ˚C, forward commitments follow a linear trend suggesting that in contrast to the WT, a single kinetic step might be

responsible for much of the forward commitment. Since F31V mutation has a significant effect on the binding of the H_2F (Table 5.1), it is plausible to suggest that binding of H_2F (which binds after the labeled NADPH)[6] is contributing significantly to the forward commitment under k_{cat}/K_M conditions.

5.3.3 Structural effects of the F31V mutation.

In order to resolve the effect of the mutation on the protein structure we determined the x-ray crystal structure of the F31V in a ternary complex with folate and $NADP^+$, as was previously done for WT *ec*DHFR.[4] We chose that particular ternary complex since it is considered to represent the Michaelis complex, as both compounds mimic the substrate and cofactor, respectively. Another ternary complex of interest was enzyme-MTX-$NADP^+$ complex. It was suggested on several different occasions that although MTX, the tightest inhibitor of *ec*DHFR, does not resemble the transition state itself, its binding geometry in the E:MTX:$NADP^+$ complex allows for the stabilization of the sub van der Waals contacts between the hydride donor and acceptor, by allowing the nicotinamide ring of the $NADP^+$ to further protrude in the active site towards the acceptor carbon.[4,190]

Extensive crystallographic and NMR studies showed that WT *ec*DHFR displays significant conformational flexibility in different stages of the kinetic cycle. One of the most prominent components of this flexibility is loop movements (of M20, F-G and G-H loops) and subdomain rotation. M20 loop is also referred to as the active site loop, since it forms direct contact with the nicotinamide ring of the $NADP^+$. Extensive X-ray studies on the WT *ec*DHFR showed that M20 loop assumes several different conformations in the crystalline state, denoted as open, closed and occluded.[4] The closed and the occluded conformations have been also observed in solution NMR experiments,[179] which suggested that M20 loop exists in the closed conformation prior to hydride transfer.

However, transient population of the open conformational state may play a role in catalytic cycle since: (i) the open conformation facilitates both substrate binding and product release; and (ii) replacement of the part of the M20 loop (residues 16-19) with glycine still yields an enzyme that exhibits some catalytic activity.[189] The open M20 loop conformation has been observed only in certain crystalline forms and it seems to be stabilized by crystal lattice contacts, *i.e.* when *ec*DHFR:Fol:$NADP^+$ ternary complex crystallizes in $P2_1$ space group M20 loop is always in the open conformational state.[4] Our goal was to determine two ternary complexes' structures within the same crystalline form as for the WT. This way any possible structural changes could be attributed to the mutation rather than to differences in crystal-packing forces. We also attempted to obtain these ternary structures in what is considered a representation of the reactive complex (where the M20 loop is in the closed conformation).

We were able to obtain and solve three x-ray crystal structures of F31V DHFR: F31V:Fol:$NADP^+$, F31V:MTX:$NADP^+$, and F31V:$NADP^+$ binary complex. All structures were solved using molecular replacement (MR) modeling with *ec*DHFR:$NADP^+$:Fol as the MR model (PDB ID 1RX2). Table 5.3 summarizes all the statistics pertaining the processing of the data and refinement. F31V:Fol:$NADP^+$ and F31V:$NADP^+$ binary complex were solved in the $P2_1$ space group, while F31V:MTX:$NADP^+$ ternary complex was obtained in the $P2_12_12_1$ space group. In all three X-ray crystal structures M20 loop is in the open conformation. It has been shown that regardless of the ligated state, when *ec*DHFR crystallized in $P2_1$ space group, M20 loop is always in the open conformation as this conformation seems to be stabilized by the crystal lattice contacts. Therefore, F31V:Fol:$NADP^+$ has been compared to equivalent WT crystal structure with same ligands (PDB ID 1RB2). Another characteristic of the $P2_1$ crystalline form is that *ec*DHFR seems to always crystallize as two crystallographically independent monomers in the asymmetric unit. For the WT[4] and series of I14 mutants,[215] we observed that in the molecule A both folate and $NADP^+$ are bound, and the

nicotinamide-ribose moiety of $NADP^+$ is rotated into the active site. On the other hand, in the molecule B, even though both substrate and cofactor are bound, the nicotinamide-ribose moiety is rotated out of the binding pocket and in most cases disordered in the solvent. These two positions of the nicotinamide ring could represent the two significant *ec*DHFR populations in the solution, since it is has been shown that the NADPH molecule initially binds through the 2'-phosphate-ADP moiety, before nicotinamide-ribose moiety "flips" into the active site, which is associated with closing of the M20 loop.

Comparison between the F31V:Fol:$NADP^+$ complex and the WT shows that the secondary structure of the F31V is the same as for the WT indicating that mutation bears no effect on the overall structure of the mutant. In the molecule A of the F31V complex both substrate and $NADP^+$ are bound, however nicotinamide ring is rotated out of the active site. On the other hand, in the molecule B only $NADP^+$ is bound and lack of any other unassigned electron density in the active site indicates that no folate is bound. Even though folate was added in the excess of the enzyme, and left to equilibrate with enzyme for long period of time, no folate bound in the molecule B is probably the result of an increase in the K_d for folate by ~20 fold due to the mutation (Table 5.1). In the molecule A, we noticed a slight rotation of the p-amino-benzoyl and pterin moieties since the size of the residue 31 is significantly reduced and allows for such motion (Figure 5.3B).

We attempted to obtain F31V:Fol:$NADP^+$ complex in a different space group (i.e. $P2_12_12_1$) where M20 loop is in a closed conformation by varying temperature of the crystal growth, pH of the mother liquid, type of salt and participate. We observed new crystals under completely different experimental conditions and pH (analysis of the all available *ec*DHFR crystal structures in PDB showed that $P2_12_12_1$ space group usually occurs near physiological conditions). The pH of the mother liquid in which these crystals appeared is 7.5 and the crystals contained only $NADP^+$ bound to the enzyme. This binary complex crystallized in the $P2_1$ space group, again with two molecules per

asymmetric unit. Due to lower folate solubility at lower pH together with poor binding constant it is not fully unexpected that we observed no folate bound. In both molecules the nicotinamide ring is rotated out into the solvent, as expected for the apo-enzyme *ec*DHFR complex.[4]

Finally, we crystallized and solved the structure of F31V:MTX:$NADP^+$ complex and compared it to the equivalent WT crystal structure (PDB ID 1RX3, and 1RB3). In this space group ($P2_12_12_1$), WT crystallizes as a single molecule per asymmetric unit (PDB ID 1RX3), however, F31V crystallized with two molecules per asymmetric unit. Significant electron density indicates that both MTX and $NADP^+$ are bound in both molecules, M20 loop is in the open conformation and nicotinamide-adenosyl moiety of $NADP^+$ occupies two populations in both molecules. It is both rotated in and out of the binding pocket, as confirmed by the iterative composite OMIT maps (Figure 5.4). The WT crystal structure used for comparison crystallized in different space group, with two molecules per asymmetric unit, but with M20 loop also in the open conformation (B-factor putty (PyMol) comparison shows no significant difference in the thermal flexibility between structures; Figure 5.5. The small difference in binding of the MTX between the mutant and the WT is presented in Figure 5.3D and Figure 5.6. MTX is well resolved in the crystal structure (Figure 5.3C), and in comparison to MTX bound in the WT we see a slight rotation of the pterin ring of MTX towards the residue 31 that is more obvious from analysis of specific H-bonds between the pterin ring and the active-site residues that are shorter in the mutant (Figure 5.6).

The lack of significant change in the orientation of the pterin ring of folate/MTX between F31V and the WT, may suggest that the altered nature of H-transfer is mainly a change in the dynamic behavior (i.e. DAD distribution) of the F31V mutant. In other words, F31V mutation could affect the enzyme's ability to form both the reactive complex (as observed from the reduction in k_H), as well as optimal TRS (as evident from temperature dependence of the intrinsic KIEs).

5.3.4 Molecular dynamic simulations

In order to obtain the molecular description of the active site caused by the mutation of the residue F31, since we could not obtain the X-ray crystal structure in the closed "reactive" conformation, we performed MD simulations at 25 ˚C (298 K) as previously done for the WT and a series of I14 mutants.[85] We started from the structure of the WT *ec*DHFR (PDB ID 1RX2), and performed mutation *in silico*. Moreover, we performed ten independent 6 ns runs, differing only in the initial velocities, in order to adequately sample the conformational landscape. The comparison of resulting conformation is presented in Figure 5.7, where two parameters of interest are described, DAD_c and Φ. The relative donor acceptor orientation was measured as the angle (Φ) between the planes that fit the nicotinamide moiety of NADPH and the pterin ring of H_2F. The DAD_cs' and Φs' distributions for F31V (Figure 5.7, 1D plots on y and x-axis) were fitted as described in ref.[85] (Table 5.5). The correlation is presented as a 2-D plot in Figure 5.7.

As evident from the Table 5.5, and Figure 5.7, the average DAD_c is slightly larger for the F31V mutant with wider distribution, however the relative orientation between the nicotinamide and pterin rings deviate significantly from the values observed for WT-like population (Table 5.5, population I). For this mutant we observe two distinct populations for the Φ angle, where both populations (VI and VII) deviate significantly from the optimal 30 degrees observed for WT. What is more interesting is that both pterin ring and the p-amino benzoyl group of H_2F rotate towards the residue 31 (Figure 5.7), which is in accord with the X-ray crystal structures discussed above. What was initially surprising is that nicotinamide ring moves towards the pterin ring, probably due to strong van der Waals interactions between two rings, which results in the same average DAD_c that is found in the WT *ec*DHFR, however with the slightly larger distribution. Even though average DAD_cs for F31V and the WT are similar, the angle Φ is greatly affected and deviates significantly from the optimal value found in the WT *ec*DHFR structure, as

noticeable in the Figure 5.7. The average DAD_c for both populations, VI and VII, remains the same due to rotation of the nicotinamide ring towards the pterin ring. This has not been observed for I14 mutants, where the mutations only affected the motion of the nicotinamide ring with which residue 14 forms a direct contact. On the other hand, it seems that the effects of F31V mutation are more comprehensive. Rotation of the pterin ring of H_2F away from the nicotinamide ring of NADPH affects the HOMO-LUMO orbital overlap, a phenomenon that has been observed previously for the population II (Chapter 3).[85] This deviation of Φ from the optimal value has a detrimental effect on the DAD_e at the TRS and the rate.[166] Consequently, we can asses that population VII contributes little to reactivity. A more quantitative assessment of the reactivity of either populations would require high-level QM/MM calculations, which are beyond the scope of this work. In the Figure 5.7 we framed the probable reactive conformation with a "black box". This approach is similar to the near-attack-conformation presented previously,[216] but is only presented as a simple visual tool to emphasize the decrease in the F31V population that would have a favorable DAD_c and Φ angle.

Lastly, we have also monitored several hydrogen bonds formed between pterin/nicotinamide rings and few active site residues. The one that showed significant deviation from the values observed for the WT is the H-bond between the backbone of Ala 7 and the amide of the nicotinamide ring. It seems that one of the bonds becomes significantly shorter for the mutant locking nicotinamide ring in the unfavorable orientation in comparison to pterin ring. Another interesting observation was the higher atomic rmsd values for the residues belonging to M20 loop (residues 15-35) and residues 40-60 (Figure 5.8) of F31V mutant in comparison to WT.

The MD simulation provides molecular insight and therefore an assessment of the effect of the mutation on the DAD_c (average distance, distribution of populations, and their dynamics) and provides insight on effects on DAD_e (donor-acceptor orbitals overlap deducted from the angel Φ). The MD simulation results obtain here support the

interpretation of the kinetic findings via the Marcus-like model. Like the previous study on the residue 14, it seems that the smaller side chain "relaxes" the active-site leading to broadening of configurational sampling within the reactive ternary complex.

5.4 Conclusion

The current study extends our understanding of the structure-dynamics-activity relations in enzyme-catalyzed reactions. Since active site residues are in the direct contact with either the substrate or the cofactor, studies of the active site mutants aid in rationalizing the relationship between the active site structure, motions, and the catalyzed chemical reaction. Temperature dependence of the intrinsic KIEs has been used to assess the extent of the specific mutation on the chemical step (bond formation/dissociation). Here, we extended our initial study on active-site residue I14,[85,141] to the opposite side of the active site, applying similar tools. The break in the temperature dependence of the intrinsic KIEs for F31V is associated with the reduced protein stability, providing possible rational to the phase transition or change in mechanism observed at 35℃. Both fitting of the KIE data to the Marcus-like model and MD simulation data suggest that longer DADs with broader distributions contribute to the steep temperature dependence of KIEs observed below 35℃ for F31V. Moreover, MD simulation data as well as X-ray crystal structures indicate that mutation worsens the protein's ability to organize the active site for efficient hydride transfer. Even though these structures and simulations are representation of the ground-state structure, it seems that deviations in the position of the substrate and the cofactor in F31V affect the ability of the heavy atoms to reorganize and bring the system to an "optimal" TRS. Together these findings suggest that in the WT *ec*DHFR residue F31 participates in the restrictive active-site motions that modulate the DAD by "pushing" the donor and acceptor closer to each other. We hope that these results will entice further investigations such as high-level QM/MM calculations and

examination of the systems dynamics at millisecond to picosecond timescale motions using NMR relaxation experiments[121] and two-dimensional infrared spectroscopy.[125]

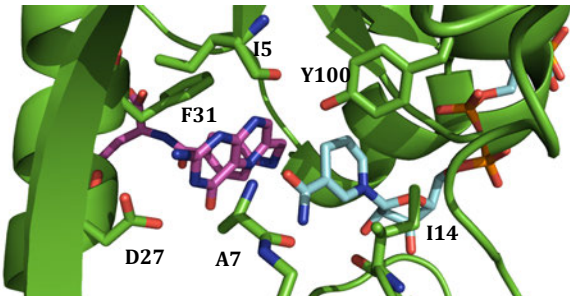

Figure 5.1 The active-site of *ec*DHFR emphasizing the role of F31 as a support of the pterin ring of H_2F. The nicotinamide ring is highlighted in light blue, and the folate in magenta. Several other residues that form important hydrogen bonds with either nicotinamide ring or pterin ring are highlighted.

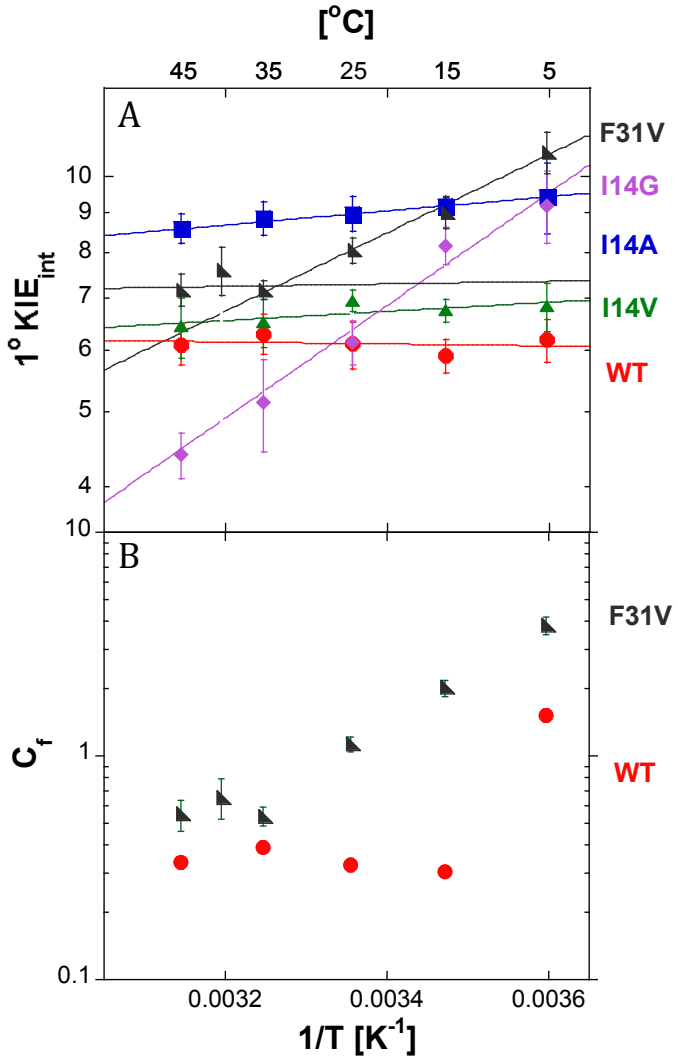

Figure 5.2 Temperature dependence of intrinsic KIEs and commitments. Panel A presents Arrhenius plot of intrinsic H/T KIEs on the hydride transfer catalyzed by WT *ec*DHFR (red),[83] series of I14 mutants,[85] and F31V *ec*DHFR (grey). The KIEs are presented as average values and standard deviations, and the lines are the nonlinear fittings of all intrinsic-KIEs to the Arrhenius equation. Panel B presents Arrhenius plot of the forward commitment (C_f) to catalysis on k_{cat}/K_M for WT and F31V DHFR. The figure presents the data as average values with standard deviations.

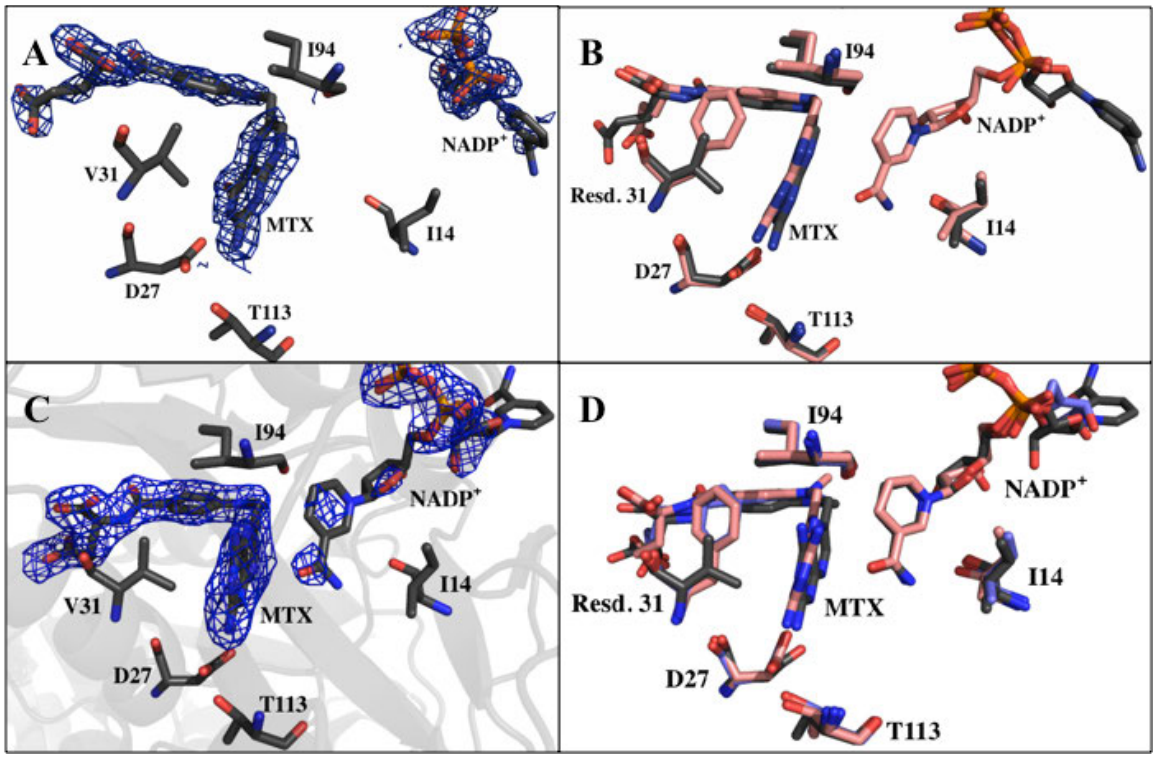

Figure 5.3 F31V mutant in comparison to WT *ec*DHFR. A) Active site structure of F31V-Folate-$NADP^+$ ternary complex illustrating the binding of the folate in the relation to D27, I94, and T113. The folate is presented with electron density $2F_o$-F_c map contoured at 1.5 σ within 1.6 Å of the ligand, and shown in blue. For better visibility of the folate we omitted showing residue I5 that also forms an important H-bond with pterin ring, and residue 31. B) Structural comparison of the active site of F31V-Folate-$NADP^+$ (grey) and WT-Folate-$NADP^+$ (pink; 1RB2). Several active site residues are shown as sticks together with both folate and $NADP^+$. Structures have been aligned in PyMol (residues exhibiting low B-factors: 1-45, 90-100, 109-116; this alignment gave lowest RMS value). Slight rotation of the *p*-amino-benzoyl moiety towards the residue 31 is observed. C) Active site structure of F31V-MTX-$NADP^+$ ternary complex illustrating the binding of the MTX and $NADP^+$ in the relation to D27, I94, and T113. MTX and $NADP^+$ are presented with electron density $2F_o$-F_c map contoured at 1.2 σ within 1.6 Å of the ligand with several active site residues. $NADP^+$ is bound in a dual conformation. D) Structural comparison of the active site of F31V-MTX-$NADP^+$ (grey) and WT-MTX-$NADP^+$ (pink-1RB3; purple-1RX3). Several active site residues are shown as sticks together with MTX and $NADP^+$. Structures have been aligned in PyMol as described in panel B.

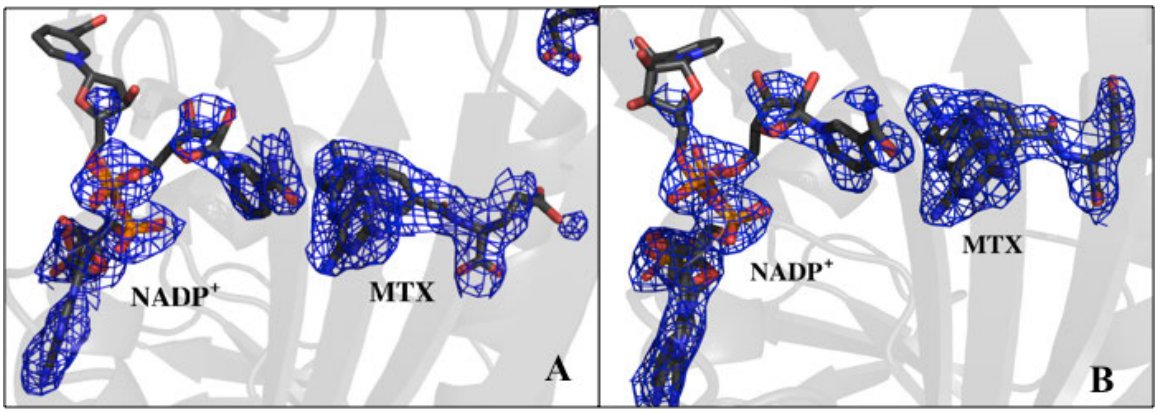

Figure 5.4 $2F_o$-F_c OMIT Fourier map for the F31V-MTX-$NADP^+$ ternary complex contoured at 1σ within 1.6 Å from the ligands for the molecule A (left) and molecule B (right).

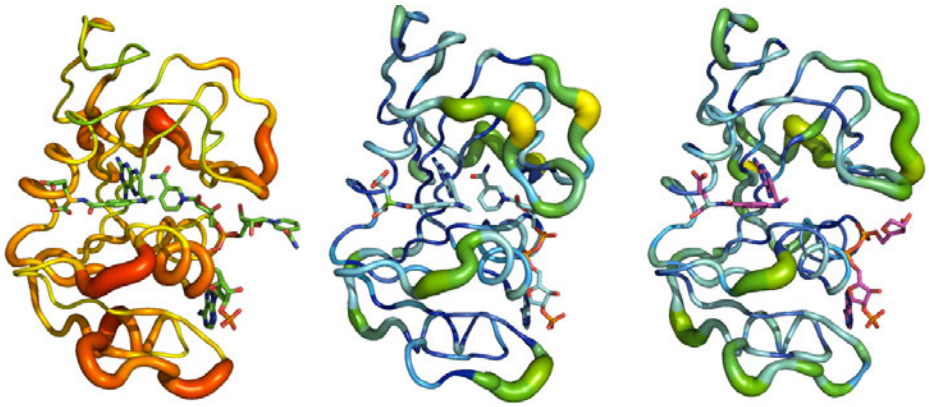

Figure 5.5 B-factor putty (PyMol) comparison between the molecule A of F31V-MTX-$NADP^+$ (left panel), WT (PDB ID 1RX3; middle panel), and molecule A of WT (PDB ID 1RB3; right panel).

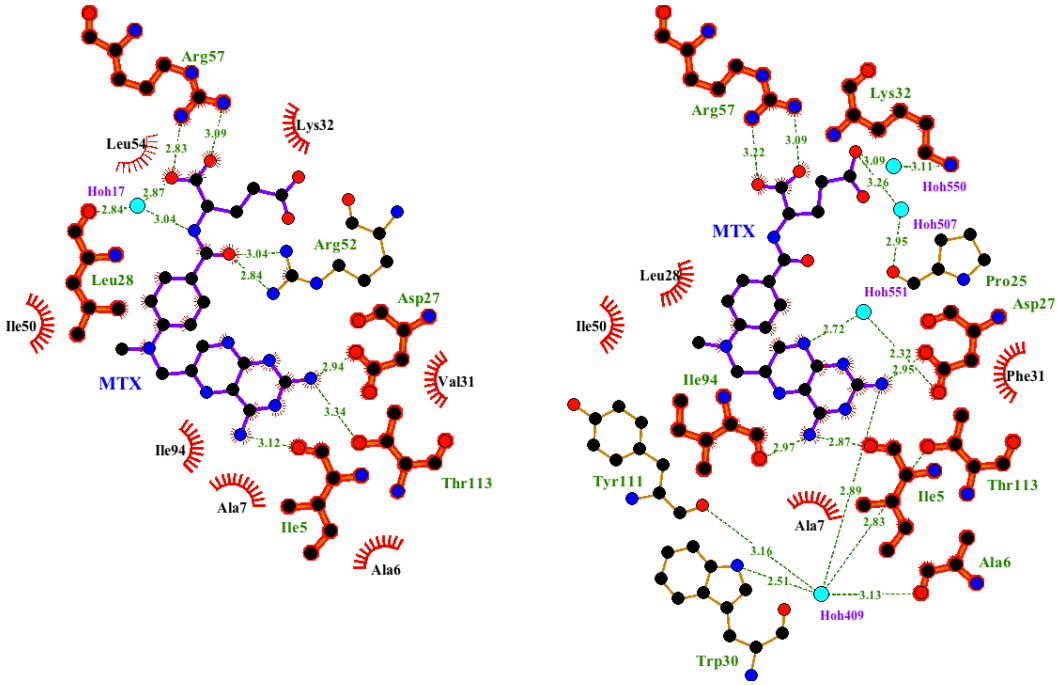

Figure 5.6 A 2D representation of the MTX bound in the active site of molecule A of F31V-NADP$^+$ (left panel), and WT-NADP$^+$ (PDB ID 1RB3; right panel) generated from the LigPlot+ analysis.[217] Most interactions are preserved between the mutant and the WT; the major difference is an increase in the two H-bonds between MTX and residues I94 and I5 in F31V complex, due to rotation of the pterin ring. Several H-bonds are conserved such as between the pterin ring of MTX and residues Asp27, and glutamyl moiety and Arg57.

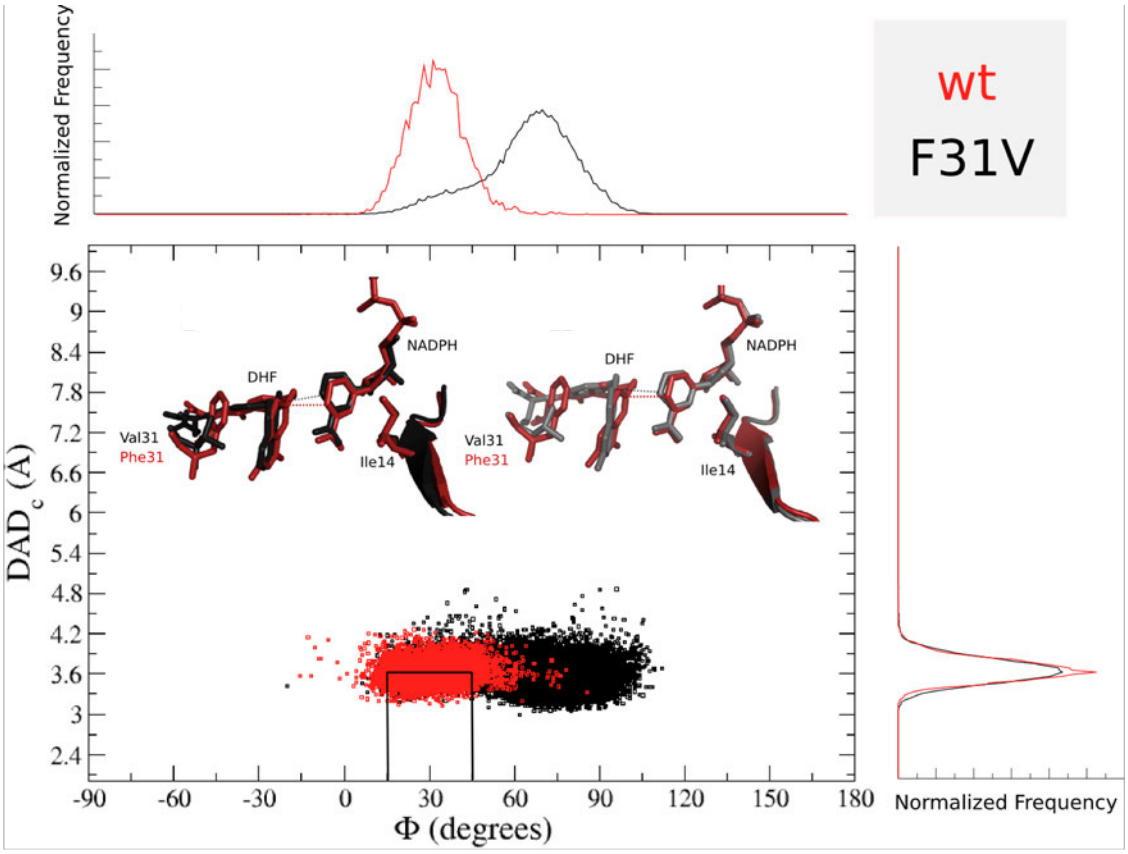

Figure 5.7 MD studies of the relative orientation of the H-donor and acceptor. Correlation plot between DAD_c and the relative orientation of donor and acceptor (ϕ) for WT (red) and F31V (black). Overlaid WT and F31V DAD_c and ϕ distributions are shown on the y and x-axis respectively. Inset represents the comparison of the average structures for the WT and F31V. For F31V mutant we observe two distinct populations that both have slightly longer DAD_c and where pterin ring is twisted towards the residue 31 (for detail definition of populations I-V and DAD_c and ϕ please refer to Figure 3.4). The black box (ϕ-value between 15°-45° and DAD_c below 3.5 Å) encapsulates the estimated 90% of the reactive conformers. That box is analogues to the "Near Attack Conformation" concept,[216] and while it does not represent a meaningful energetic or kinetic space of states, it illustrates the geometrical bottleneck through which reactive conformation have to pass on their way to the TRS. Larger population of ground states in that box indicates larger fraction of reactive states.

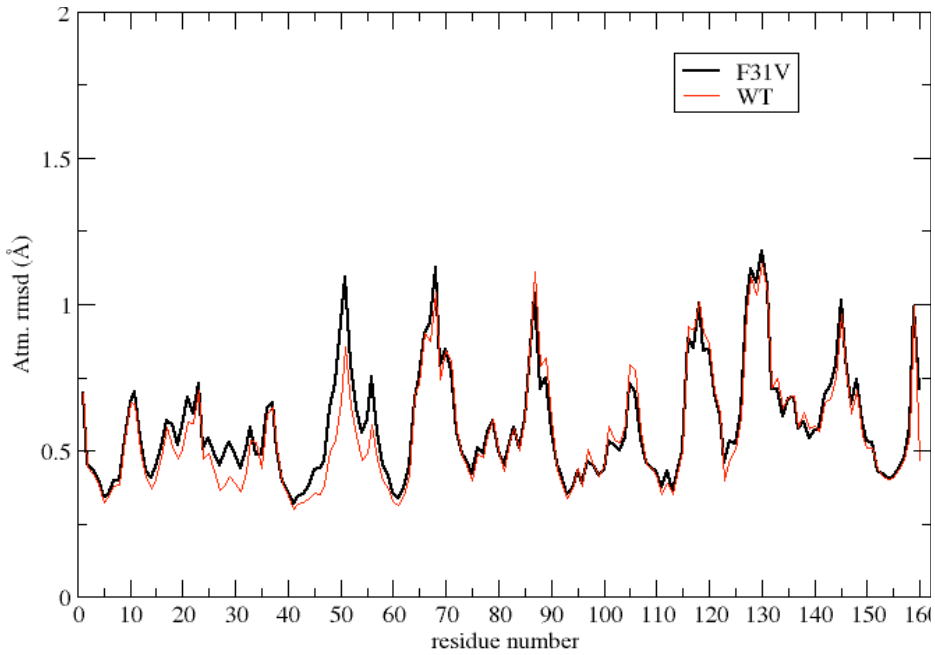

Figure 5.8 RMS fluctuation for all residues of wtDHFR, presented in black, and average of ten 6 ns runs for F31V shown in red.

Table 5.1 Reaction rates, binding constants and isotope effects on Arrhenius activation parameters for several active site mutants of *ec*DHFR.

DHFR / Parameters	WT	I14V	I14A	I14G	F31V	
k_{cat} [s^{-1}]	12.3 ±0.7[c]	ND	15 ±1.7[g]	ND	26 ±10[d]	
k_H[a][s-1]	228 ±8[c]	33.3 ±3.1[f]	5.7 ±0.3[f]	0.22 ±0.04[f]	17.7 ±0.1[i]	
$K_{d\ (H2F)}$ [μM][b]	0.21 ±0.03[d]	ND	0.22 ±0.07[g]	ND	6.6 ±0.5[d]	
$K_{d\ (NADPH)}$ [μM][b]	0.38±0.04[d]	ND	1.4 ±0.1[g]	ND	0.22 ±0.02[d]	
AH/AT	7.0 ±1.5[e]	4.2 ±0.4[f]	4.7 ±0.5[h]	0.024±0.003[f]	6.42 ±1.28[i]	0.165±0.012[i]
Δ*E*a(T-H), [kcal/mol]	-0.1 ±0.2[e]	0.27 ±0.05[f]	0.39 ±0.06[h]	3.31 ±0.07[f]	0.08 ±0.10[i]	2.30 ±0.04[i]

a. Pre-steady state rate constants of hydride transfer at 25˚C and pH 7.0

b. Thermodynamic dissociation constants determined at 25˚C and pH 7.0.

c. Ref. [6]

d. Ref. [207]

e. Ref. [83]

f. Ref. [85]

g. Ref. [140]

h. Ref. [141]

i. This work.

ND = not determined

Table 5.2 Experimental ΔE_a (from Table 1) and regression parameters for WT *ec*DHFR and the active site mutants studied to date.

Enzyme	**ΔE_a (kcal/mol)**	**Fitting Parameters**				**Reference**
		1 Population		**2 Populations**		
		DAD_c	***f***	**DAD_c**	**ΔG**	
WT	-0.1 ±0.2	3.06	>250	3.06	>2.5	[73,83]
I14V	0.27 ±0.05	3.08	200	3.06	2.3	[73,85]
I14A	0.39 ±0.06	3.09	190	3.07	2.4	[73,85]
I14G	3.31 ±0.07	NA	NA	3.31	3.8	[73,85]
F31V (>35˚)	0.08 ±0.10	3.07	144	3.06	3.5	
F31V (<35˚)	2.30 ±0.04	NA	NA	3.23	2.61	

Table 5.3 Data-collection and refinement statistics.

Identification	Feb_1_3	Sep_4_3 -#38	Sep_5_6 - #37
Ternary complex	F31V:Folate:$NADP^+$	F31V:$NADP^+$	F31V:MTX:$NADP^+$
Data collection			
Source	ALS (LBNL) BeamLine 4.2.2		
Temperature (K)	100	100	100
Wavelength (Å)	0.976	1.000	1.000
Space group	$P2_1$	$P2_1$	$P2_12_12_1$
Unit cell parameters			
a (Å)	41.13	38.46	64.84
b (Å)	74.13	59.126	64.86
c (Å)	58.64	71.090	139.90
b (°)	98.76	102.563	90
Resolution range (Å)	32.35 – 2.07	37.54-1.55	32.64 – 2.20
No. total reflections	20969	84182	216110
R_{merge}	0.039 (0.145)	0.056 (0.557)	0.110 (0.648)
<I/s(I)>	18.6 (7.3)	13.4 (2.4)	8.7 (2.0)
Completeness (%)	98.6 (99.6)	97.6 (95.4)	100 (100)
Multiplicity	3.6 (3.7)	3.7 (3.6)	7.02 (8.86)
Mosaicity (˚)	0.401	0.25	0.90
Refinement			
R_{work}/R_{free}	18.67/25.07	19.56/22.71	23.05/25.50
No. atoms			
Protein	2539	2598	2528
Ligand/ion	128	96	258
Water	256	278	14
B-factors			
Protein	18.7	16.7	45.0
Ligand/ion	20.8	18.7	47.5
Water	22.1	24.3	33.1
R.m.s. deviations			
Bond lengths (Å)	0.015	0.015	0.015

Table 5.3 Continued

Bond angles (˚)	1.547	2.011	1.888
Ramachandran plot, residues in			
Most favored regions (%)	97.78	99.69	94.90
Allowed regions (%)	2.22	0.31	5.10
Disallowed (%)	0.00	0.00	0.00

Note: Values in parentheses are for the highest resolution shell

Table 5.4 Observed KIEs and their standard deviations for F31V DHFR.

Temp. ˚C	H/T KIE	D/T KIE
45	4.985 ± 0.042	1.706 ± 0.012
40	4.990 ± 0.025	1.721 ± 0.019
35	5.008 ± 0.017	1.707 ± 0.007
25	4.306 ± 0.011	1.687 ± 0.009
15	3.657 ± 0.023	1.650 ± 0.010
5	3.011 ± 0.019	1.599 ± 0.010

Table 5.5 DAD_c distributions for the different conformations found along MD simulation obtained from Gaussian analysis (see text).

DHFR Active site conformation		<DAD> (Å)	σ (Å)[c]	<F>[d] (degrees)	Fraction	R
wt	I[a]	3.58	0.16	29.0	1	0.9979
I14V	I[a]	3.61	0.17	23.6	0.86	
	III[b]	4.02	0.31	-10.8	0.14	0.9984
I14A	I[a]	3.61	0.17	21.7	0.68	
	II[a]	3.61	0.17	75.5	0.13	0.9980
	III[b]	4.18	0.49	-20.5	0.19	
	I[a]	3.60	0.19	20.4	0.33	
I14G	II[a]	3.60	0.19	80.8	0.26	0.9943
	III[b]	5.27	0.82	-26.2	0.09	
	IV[b]	6.05	0.67	-37.2	0.22	
	V[b]	8.10	0.36	39.9	0.1	
F31V	VI[a]	3.60	0.21	40.0	0.22	0.9975
	VII[a]	3.60	0.21	70.3	0.78	

a. Fitted to a split-Gaussian,

b. Fitted to a Gaussian.

c. For split-Gaussian σ is the average of both parts. σ is the standard deviation of the DAD_c.

d. Φ separately from the DAD_c.

CHAPTER 6.
EVIDENCE THAT A 'DYNAMIC KNOCKOUT' IN ESCHERICHIA COLI DIHYDROFOLATE REDUCTASE DOES AFFECT THE CHEMICAL STEP OF CATALYSIS[vii]

6.1 Introduction

One of the contemporary questions in enzymology is the link between protein dynamics and function. Significant advancements have been achieved toward characterizing protein motions across wide-ranging timescales from seconds to femtoseconds and investigating their functional relevance. For instance, the importance of protein motions on the milli- to microsecond timescale has been recognized to be crucial to both substrate binding and product release, often contributing to the rate-limiting step in the catalytic turnover. However, the precise role of the protein motions in assisting chemical transformation has remained unclear and is still source of a heated debate. Elucidating the role of the protein motions is crucial to understanding enzyme mechanisms, as this knowledge will greatly assist in widening their applicability in industrial and medicinal settings. Previous kinetic and computational studies on the model enzyme in question, dihydrofolate reductase from *Escherichia coli* (*ec*DHFR), suggest that protein fluctuations responsible for the reorganization of the heavy atoms in the active site and the conformational sampling of the donor - acceptor distance (DAD) are crucial to facilitating H-transfer.[8,18,84,85,139,197,198,218-221] While none of the experimental data indicated involvement of non-statistical dynamics[viii] in catalysis, and

[vii] This chapter has been submitted to the journal of *Nature Chemistry.*

[viii] Non-statistical dynamics: molecular motions that are not in thermal equilibrium with their environment. Their role in enzymology has been matter of on-going debate(Hay, S. & Scrutton, N.S. Good vibrations in enzyme-catalyzed reactions. *Nat. Chem*. **4**, 161-168 (2012); Glowacki, D.R., Harvey, J.N. & Mulholland, A.J. Taking Ockham's razor to enzyme dynamics

none of the calculations (besides one exception[222]) required non-statistical dynamics, researchers presented different opinions regarding the role of dynamics in catalyzing the chemical step.

The effect of protein dynamics on the chemical coordinate of the reaction has been indirectly investigated through the examination of the temperature dependence of KIEs and by computational methods. The advantage of this experimental method is that the temperature dependence of KIEs is highly sensitive to the changes in DAD, which can modulate the degree of the wavefunction overlap between the donor and acceptor states. As suggested by several phenomenological models, denoted here as Marcus-like models (presented later in more detail), if the conformational fluctuations assist the chemical transfer through modulation of the DAD and the wave-function overlap, then that will manifest in an increase in the temperature dependence of the KIEs.[39,40,42,125] In such analysis, however, extraction of the intrinsic KIEs is challenging, as the chemical step in most enzymatic systems is not rate-limiting and is therefore masked by other, isotopically insensitive steps when the reactive C-H bond is isotopically labeled. This kinetic complexity masks the intrinsic KIEs and leads to the observed KIEs that are smaller than their intrinsic value. In single-turnover experiments, as conducted in refs [1,193], the kinetic complexity is commonly associated with conformational changes and changes in protonation that occur prior to the formation of the reactive ternary complex.

One of the most widely used enzymatic models for the structure/function/dynamic relationship is *ec*DHFR. *Ec*DHFR is a small, flexible protein that catalyzes the reduction of 7,8-dihydrofolate (H_2F) to 5,6,7,8-tetrahydrofolate (H_4F), with the stereospecific transfer of a pro-*R* hydride from the C4 position of the reduced nicotinamide adenine dinucleotide phosphate (NADPH) to the C6 of the dihydropterin ring of H_2F, which is

---

and catalysis. *Nature Chem.* **141**, 169-176 (2012); Editorial. Of polemics and progress. *Nature Chem*. **4**, 141 (2012))

already protonated at its N5 position prior to hydride transfer occurring (Figure 6.1).[7,9,193,223] *Ec*DHFR has an α/β structure consisting of a central eight-stranded β sheet and four α-helices connected with several loop regions. One of the loops is a flexible active-site loop, the M20 loop (residues 9-24), which undergoes large conformational changes between the Michaelis complex and the product complex.[4,224] Extensive X-ray studies showed that the M20 loop can adopt four characteristic conformations and its movement is coordinated with different stages of the catalytic cycle.[4] In the solution it exists in two dominant conformations: closed, where the loop packs closely against the nicotinamide ring, and the occluded, where the loop protrudes into the active site, sterically blocking the nicotinamide binding pocket.[5] Alignment of human DHFR and *ec*DHFR sequences suggested that the occluded conformation in the human DHFR is destabilized due to a biproline sequence at the end of the M20 loop, leading to an increase in the rigidity of the loop in comparison to the one in *ec*DHFR.[1]

In 2011, Bhaba *et al*[1] studied the possible correlation between millisecond M20-loop motions (examined *via* NMR relaxation experiments) and the apparent hydride-transfer rate (examined *via* single-turnover measurement) using three mutants of *ec*DHFR: N23PP, S148A and N23PP-S148A. The double mutant N23PP-S148A,[ix] and N23PP (S148A mutation seems to have little or no effect) were named "dynamic knockout" mutants, as their respective flexible M20 loops rigidified, resembling the rigidity of the M20 loop in human DHFR. NMR results suggested that millisecond-timescale fluctuations in the active site of WT *ec*DHFR are equally abrogated in the

[ix] Bhaba et al.(Bhabha, G. et al. A dynamic knockout reveals that conformational fluctuations influence the chemical step of enzyme catalysis. *Science* **332**, 234-238 (2011)) showed that addition of the bi-proline sequence in N23PP and N23PP-S148A mutants is responsible for the suppression of the mili- to microsecond timescale motions of the M20 loop in the Michaelis complex having also a significant effect on khyd measured by FRET-stopped-flow. On the other hand, while S148A mutation affects the mili- to microsecond timescale motions of M20 loop, it has no significant effect on khyd. Therefore, the kinetic study here is performed on the N23PP ecDHFR instead on the double mutant.

N23PP as in the double mutant, while the x-ray structure of the relevant ternary complex of the double mutant suggested that mutation barred no effect on the structure of the active site. Moreover, the addition of the bi-proline sequence significantly reduced the single-turnover rate (k_{hyd}) relative to the WT. Although the observed H/D KIEs at 25 ˚C were the same as for the WT, the authors suggested that the altered millisecond-timescale motions modified the chemical step (as evident from reduced apparent k_{hyd}) and thus might be directly coupled to the H-transfer. This dramatic conclusion was followed by theoretical[225] and experimental[193] studies that challenged this interpretation. Importantly, EVB calculations[225] implied that the depressed catalytic effects in the mutants are due to changes in reorganization energy. It is vital to note that while motions along the slow conformational coordinate, which were examined by the NMR relaxation experiments, have a substantial effect on the rate of the turnover and the rate constant for the apparent hydride transfer, they might not be coupled to the much faster chemical step (dissociation of the C-H bond at femto- picosecond time scale[219]). Experimental studies of the temperature dependence of KIEs in a variety of enzymatic systems[39,74,125,176,226] indirectly indicate the existence of the fast motions, proposed to occur at the femto- to picosecond timescale, and their possible coupling to the reaction coordinate. Therefore, Allemann and coworkers, [193] using the same experimental method as ref [1] for examining the rate of H-transfer and its KIEs, assessed the temperature dependence of KIEs for the N23PP-S148A *ec*DHFR. Their observed single-turnover KIEs were the same as for the WT *ec*DHFR throughout the temperature range, and the authors concluded that there is no detectable dynamic coupling of protein motions to the hydride transfer.[193]

In the current paper, we report the temperature dependence of the intrinsic KIEs and hence allow for new assessment of the effect of the N23PP mutation on the chemical step in *ec*DHFR. Our findings indicate that the temperature dependence of the kinetic complexity in the stopped-flow measurements[1,193] masked the differences between the WT and mutant, as the intrinsic KIEs and their temperature dependence are actually quite

different (*vide infra*). These findings invert the conclusions of ref [193], and indirectly imply that motions faster than the millisecond motions examined by NMR[1] are also altered and affect the chemical step in question (C-H→C).

6.2 Materials and methods

Chemicals. [Ad-^{14}C]-NAD$^+$ (specific radioactivity of >220mCi/mmol) was purchased from Perkin Elmer. H_2F was prepared by dithionate reduction of folic acid as described previously.[107] Glucose dehydrogenase from *Bacillus megaterium* (*bm*GluDH) was purchased from Affymetrix/USB. All other materials were purchased from Sigma. (*R*)-[4-^{3}H]-NADPH was synthesized through a 3-step synthesis as described before. [111] [Ad-^{14}C]-NADPH was prepared from [Ad-^{14}C]-NAD$^+$ using NAD$^+$ kinase from chicken liver, followed by reduction with glucose using *bm*GluDH.[95] (*R*)-[Ad-^{14}C,4-^{2}H]-NADPH was synthesized through the reduction of [Ad-^{14}C]-NADP$^+$ with deuterated glucose and *bm*GluDH.[142] All synthesized materials were purified and stored as described previously.[109] N23PP *ec*DHFR was expressed and purified as described before.[1]

Kinetic isotope effect measurements. KIEs with N23PP *ec*DHFR were measured as described before for the WT and numerous DHFR mutants.[84,85,104] In short, we combined (*R*)-[4-^{3}H]-NADPH and [Ad-^{14}C]-NADPH, and, (*R*)-[4-^{3}H]-NADPH and (*R*)-[Ad-^{14}C,4-^{2}H]-NADPH in the 5:1 radioactivity ratio in order to measure H/T and D/T 1˚KIEs, respectively. Each mixture was co-purified on an analytical reverse-phase HPLC column, divided into aliquots containing 300,000 dpm of ^{14}C, and frozen in liquid nitrogen for short-term storage at -80 ˚C. All experiments were performed in MTEN buffer (50 mM MES, 25 mM Tris, 25 mM EtOH-NH_2 and 100 mM NaCl) at pH=9.0 over the 5-45 ˚C temperature range. All reaction mixtures contained around 200-fold excess of H_2F (0.85 mM) over NADPH (4 μM). The reactions were quenched by adding an excess of methotrexate (K_d=1 nM), and samples were stored on dry ice prior to HPLC

analysis.[84,104] Before the HPLC-LSC analysis, samples were thawed and bubbled with oxygen to ensure complete oxidation of the product H_4F. The samples were then separated by reverse-phase HPLC using a method described elsewhere.[109] The observed KIEs were calculated using the following equation[29]:

$$KIE = \frac{\ln(1-f)}{\ln[1-f*(R_t/R_\infty)]} \qquad (3)$$

where the ratio of ^{14}C in the product and reactant determined the fractional conversion (f), and R_t and R_∞ are the ratio of $^3H/^{14}C$ at each time point and at infinite time, respectively.

Determination of the intrinsic KIEs. The intrinsic KIEs were calculated as described in details elsewhere,[84,85,104] using a numerical solution of the Northrop equation modified for tritium as the reference isotope[74,104]

$$\frac{{}^T(V/K)^{-1}_{H_{obs}} - 1}{{}^T(V/K)^{-1}_{D_{obs}} - 1} = \frac{(k_H/k_T)^{-1} - 1}{(k_H/k_T)^{-1/3.34} - 1} \qquad (4)$$

where ${}^T(V/K)_{Hobs}$ and ${}^T(V/K)_{Dobs}$ are the observed H/T and D/T KIEs, respectively, and k_H/k_T represents the intrinsic H/T KIE. The intrinsic KIEs were calculated numerically from all possible combinations of observed H/T and D/T values. The isotope effects on the activation parameters for the intrinsic KIEs were calculated by a nonlinear fit of all intrinsic values to the Arrhenius/Eyring equation for KIEs:

$$k_l/k_h = A_l/A_h \cdot e^{\Delta E_{a_{h-l}}/RT} \qquad (5)$$

where k_l and k_h are the rates for light and heavy isotopes, respectively, A_l/A_h is the isotope effect on the Arrhenius pre-exponential factor, $\Delta E_{a\ h\text{-}l}$ is the difference in energy of activation between the two isotopes, R is the gas constant and T is the absolute temperature.

6.3 Results and Discussion

6.3.1 Temperature dependence of the KIEs

Pre-steady-state kinetic measurements (under single-turnover conditions) indicated that both dynamically altered mutations (N23PP and N23PP/S148A) reduced single-turnover rate to the same extent (~15 fold), [1] while the observed H/D KIEs and their temperature dependence for the double mutant coincided with the values obtained for WT *ec*DHFR (Table 1 in ref [193]). However, under single-turnover conditions the chemistry in *ec*DHFR is not rate-limiting,[6,84] resulting in smaller observed KIEs. More specifically, under the pre-steady-state conditions used in refs,[1,193] the rate measured includes at least three kinetic steps: the isotopically insensitive flip of the nicotinamide ring in and out of the active site, the closing of the M20 loop, the protonation of H_2F, and the hydride transfer itself.[64,84] This raised concern that both studies of N23PP DHFR mutants[1,193] might have captured not only the effects on the chemical step (C-H→C transfer) but also a more complex process that involves the preparation of the system prior to the tunneling-ready state (TRS; see below) at which chemistry (H-transfer) occurs.

The current work measures H/T and D/T KIEs on the second-order rate constant (k_{cat}/K_M or V/K) under competitive conditions. The combination of these two observed KIEs affords assessment of their intrinsic values as described before.[104] In short, we measured competitive H/T and D/T KIEs with WT[83] and N23PP *ec*DHFR under the same conditions using mixtures of [4R-^{3}H]-NADPH with [Ad-^{14}C]-NADPH and mixtures of [Ad-^{14}C, 4R-^{2}H]-NADPH and [4R-^{3}H]-NADPH for H/T and D/T KIE measurements, respectively. Intrinsic KIEs were extracted from the observed values using the modified Northrop equation.[104] and were fitted to the Arrhenius equation (Figure 6.2; also see Table 6.1 and Table 6.2) as previously described.[84,104] Table 1 compares the isotope effects on the Arrhenius activation parameters for the WT and N23PP *ec*DHFRs. Using

the same logic as Loweridge *et al* in a recently published paper in this journal,[193] we see that the addition of the biproline at the end of the M20 loop results in the alteration of the nature of the hydride-transfer step as indicated by larger and more temperature-dependent intrinsic KIEs (see Figure 6.2 and Table 6.3). These findings reveal that other isotopically insensitive steps, besides the chemical step, affect the KIE data presented in refs [1] and [193]; however, this does not mean that the millisecond dynamics measured in ref [1] are coupled to the chemistry. As indicated in refs [225] and [219], it is more likely that dynamics on the faster timescale are also altered by mutation and affect the H-transfer step.

In accordance with ref [193] and most other studies of the temperature dependence of KIEs, the KIE data serve as an indicator of the nature of the H-transfer. The Marcus-like model (also addressed as environmentally coupled tunneling, rate-promoting vibrations, vibrationally enhanced tunneling, etc.[39,58,62,72,74,116,118,120,127,174]) is often used to correlate the KIE data with protein dynamics for enzyme-catalyzed H-transfer reactions. According to this model, after the formation of the reactive complex (a process sometimes referred to as pre-organization), heavy-atom motions are necessary to bring the system to a point where donor and acceptor wells are degenerate and hydrogen tunneling is plausible (i.e. tunneling ready state, TRS).[39,58,62,72,74,116,118,127,174] Based on the theoretical studies of various enzymatic systems,[48,64,65] it appears that "promoting modes" of the enzyme affect the search through the conformational space to efficiently find those modes that decrease both barrier height and width, and as a result, increase the probability of reaching an "optimal" TRS. Furthermore, QM/MM calculations on *ec*DHFR have suggested that temperature dependence/independence of the intrinsic KIEs mainly reflects the temperature dependence of DAD.[49,197] Therefore, according to Marcus-like models, the findings in ref [193] would have suggested no effect of the N23PP mutation on the chemistry. On the other hand, the new observation of larger and temperature-dependent KIEs for the mutant in comparison to temperature-independent KIEs for the WT *ec*DHFR indicates a longer average DAD with broader fluctuations for

the mutant. Similar effects of mutations on the intrinsic KIEs have been analyzed by QM/MM calculations,[197] which indicated that the mutations perturbed the orientation and relative dynamics of the DAD. These altered fluctuations probably occur at a faster timescales (fs-ns) than the ones examined in ref [1] (on the ms timescale), suggesting that the N23PP mutation probably alters a broad range of dynamics, from ms to fs timescales.

Overall, the x-ray crystal structure obtained for N23PP/S148A was very similar to the WT *ec*DHFR structure (for the same ternary complex). One of the only differences was a decrease in the average distance between the donor and acceptor carbons from the 3.3 to 2.9 Å (note that the DAD used in the Marcus-like models is not that of the carbons but rather from H-reactant state to H-product state). Some studies deemed this change insignificant;[1] however, it could be quite significant if relevant to the reactive conformation.[225] It is important to note that crystal structures are representations of the ground-state structures, and DAD at the TRS might differ significantly from the population most likely to crystallize. While the ground state in the crystal structures[1] indicated shorter distance for the mutant, its average DAD and its distribution at the TRS are probably longer, as the difference in the temperature dependence of the KIEs suggests.

6.3.2 Kinetic complexity.

The main goal of this paper is the same as that of refs [1,193]: to examine possible dynamic coupling of protein motions to the hydride transfer step in *ec*DHFR. However, examinations of observed and intrinsic KIEs ultimately led to opposing conclusions. Therefore, it is important to comprehend the difference in nature of the KIE experiment performed here and done formerly[1,193] in order to understand why no significant differences in KIEs between WT and N23PP mutants of *ec*DHFR were previously

observed. The explanation lies in the kinetic complexity still masking the intrinsic KIEs when measuring pre-steady state rates.

In most enzymatic and organic reactions, observed KIEs on bond cleavage are generally smaller than their intrinsic values, due to kinetic complexity (i.e. substrates binding, product release, conformation changes, protonation changes, etc.) that masks the intrinsic KIE values. The following equation presents this kinetic complexity:

$$KIE_{obs} = \frac{KIE_{\text{int}} + C_f + C_r * EIE}{C_f + C_r + 1} \qquad (1)$$

where KIE_{obs} is the observed KIE, KIE_{int} is the intrinsic KIE, EIE is the equilibrium isotope effect, and C_f and C_r are the forward and reverse commitments to catalysis, respectively. For the hydride transfer reaction catalyzed by *ec*DHFR, the $C_r \approx 0$ and the EIE is close to unity because the reaction is very exothermic and the H-isotope is bound to sp^3 carbon in both reactant and product states. Therefore, we can simplify equation (1) to equation (2):

$$KIE_{obs} = \frac{KIE_{\text{int}} + C}{1 + C} \qquad (2)$$

where the commitment C is the sum of the ratios between the rate of the forward isotopically sensitive hydride-transfer step and each of the rates of the preceding backward isotopically insensitive steps.[102] Consequently, we can calculate C from the observed and intrinsic KIEs at each temperature. Figure 6.3 presents the commitment plotted on a logarithmic scale against the inverse absolute temperature. The C on either *V/K* or single-turnover KIEs was calculated from their respective observed values and the intrinsic values (obtained here) using equation (2).

The observed KIE on *V/K* involves microscopic rate constants for all the kinetic steps from binding of the labeled substrate (NADPH) to the first irreversible step. The observed KIEs measured under single-turnover conditions include steps from the binding of H_2F to the enzyme-NADPH complex to the hydride-transfer step (*i.e.* the flip of the

nicotinamide ring in and out of the active site, the closing of the M20 loop, the protonation of H_2F, and the hydride transfer itself). Therefore, the C for *V/K* measurements is always larger than that for single-turnover measurements under the same conditions. As reported before,[6] the chemical step is less rate-limiting at pH 7, thus C is always larger at the pH 7 than at pH 9 (note in Figure 6.3A). We observe similar correlations for the N23PP mutant (Figure 6.3B). Another indication that the KIEs measured by single turnover are not commitment-free is the significant pH dependence of both observed KIEs as well as their commitments (Figure 6.3 in ref [193] and Figure 6.3A). Allemann and co-workers[193] calculated[7,9] and demonstrated experimentally for WT *ec*DHFR that the protonation of N5 position on H_2F precedes the hydride transfer. Consequently, protonation constitutes one of the microscopic rate constants that are included in the pH-dependent C for the single-turnover measurement.

Interestingly, comparison of the C determined for the WT and the mutant, under the same experimental conditions, provides us with some information regarding the effect of the mutation on the function. Unlike for WT *ec*DHFR, where C has two phases at high and low temperatures, we observe a linear trend (see the blue data in Figure 6.3A vs.6. 3B) in the case of N23PP, which could indicate a single step as responsible for most of the commitment. Since the addition of the biproline sequence at the end of the M20 loop restricts the motion of that loop,[1] the opening of the M20 loop and flipping-out of the nicotinamide ring of NADPH from the active site are now possibly slower at the lower temperature (a consequence of the higher E_a for these ms conformational fluctuations), contributing significantly to this commitment. Also, C under either *V/K* or single-turnover conditions is always larger for the mutant, as evidenced by Figure 6.3. This supports the idea that altered dynamics on a slower timescale affect the pre- and reorganization processes, which occur prior to the catalyzed chemical transformation (C-H→C), for both sets of microscopic rate constants (i.e., those involved with *V/K* and the smaller set involved in single-turnover measurement).

Most importantly, the difference in the temperature dependences of the C for the single-turnover measurements for the WT *vs*. the mutant explains the similarity in the observed KIEs for these enzymes as reported in ref [193]. The C values for the mutant are larger across the temperature range and are more temperature dependent than for the WT. Similar correlation in the temperature dependence of the intrinsic KIEs between the mutant and the WT is observed (Figure 6.2) leading to compensation of the mutation effect on C and on the intrinsic KIE.

6.4 Conclusions

Here we have shown that in contrast to previous reports in *Science* and this journal,[1,193] restriction in the flexibility of the M20 loop in the N23PP *ec*DHFR led in fact to a change in the nature of the hydride-transfer step, as indicated by the change in the temperature dependence of the intrinsic KIEs. Moreover, the new findings indicate that the mutation altered a broad range of motions (from ms to fs timescales). These include ms-μs motions examined in ref [1], which impaired the ability of the enzyme to achieve optimal TRS, resulting in larger kinetic complexity. Additionally, alteration of much faster dynamics affected the isotopically sensitive chemical step (C-H→C), resulting in temperature-dependent intrinsic KIEs. To gain more insight into which motions contribute to chemistry of *ec*DHFR, attempts to probe femto-picosecond dynamics of the wild type and mutant are underway using vibrational spectroscopy (e.g., 2D-IR[125]). Lastly, the dynamic-knockout mutant was created in order to resemble the dynamic of the M20 loop in human DHFR. It would be of interest to undergo similar analysis presented here in order to probe the nature of the hydride transfer in human DHFR.

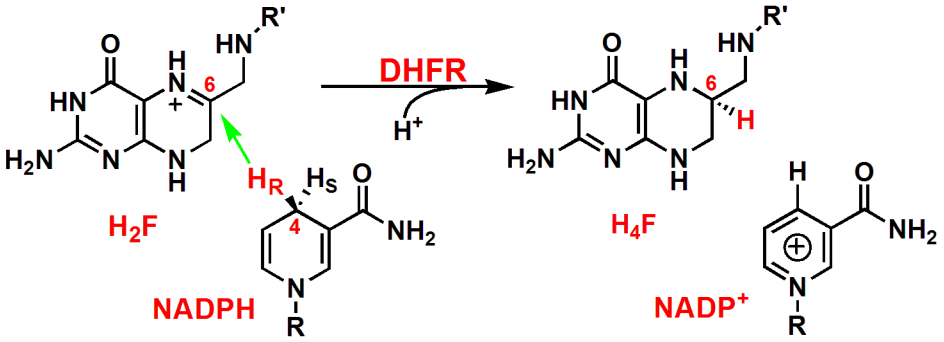

Figure 6.1 The reaction catalyzed by DHFR. R = adenine dinucleotide 2' phosphate and R' = (p-aminobenzoyl) glutamate. It was shown previously that the protonation of the N5 position occurs prior to hydride transfer.[7,9,193,223]

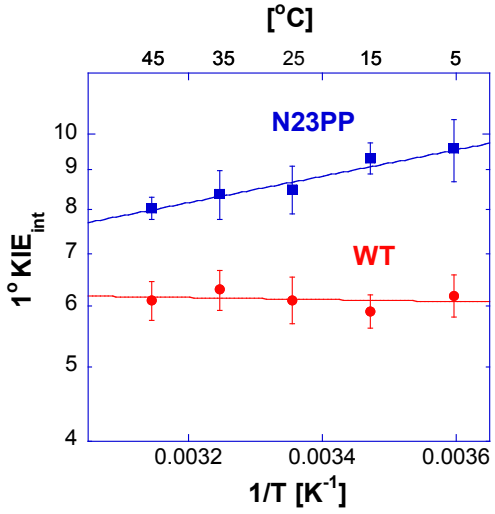

Figure 6.2 Arrhenius plot of intrinsic H/T KIEs on the hydride transfer catalyzed by WT *ec*DHFR (red)[83] and N23PP DHFR (blue). The figure shows the KIEs as average values and standard deviations, and the lines are the nonlinear fittings of all calculated intrinsic KIEs to the Arrhenius equation.

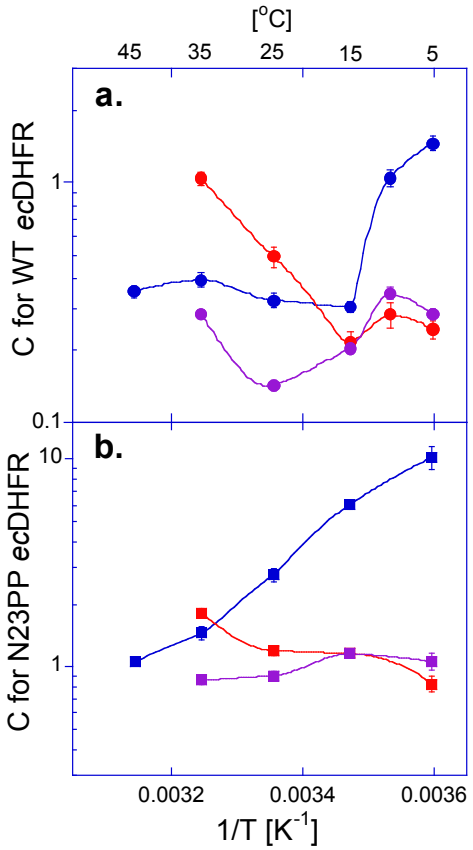

Figure 6.3 Comparison of the Arrhenius plot of C. a) C for WT *ec*DHFR determined for the observed *V/K* KIEs at pH 9 (blue circles),[83] and observed KIEs obtained under single turnover conditions at pH 7 (red circles) and at pH 9 (purple circles).[193] b) C for N23PP determined for the observed *V/K* KIEs at pH 9 (blue squares), and observed KIEs obtained under single turnover conditions at pH 7 (red squares) and at pH 9 (purple squares).[193] The figure presents the data as average values with standard deviations. The lines are an interpolation of the data and do not represent any fitting.

Table 6.1 Observed KIEs and their standard deviations for N23PP DHFR.

Temp. ˚C	H/T KIE	D/T KIE
45	4.402 ± 0.048	1.694 ± 0.007
35	3.995 ± 0.046	1.668 ± 0.016
25	2.984 ± 0.031	1.554 ± 0.012
15	2.181 ± 0.012	1.420 ± 0.005
5	1.765 ± 0.019	1.312 ± 0.008

Table 6.2 Intrinsic KIEs and their standard deviations for N23PP DHFR.

Temp. ˚C	H/T KIE	H/D KIE	D/T KIE
45	8.025 ± 0.266	4.302 ± 0.099	1.865 ± 0.019
35	8.360 ± 0.602	4.427 ± 0.223	1.888 ± 0.041
25	8.479 ± 0.608	4.471 ± 0.223	1.896 ± 0.041
15	9.313 ± 0.426	4.775 ± 0.152	1.950 ± 0.027
5	9.571 ± 0.880	4.867 ± 0.337	1.966 ± 0.058

Note: These values are calculated from the observed H/T and D/T KIE data using Northrop's method as described in the Materials and methods. The errors indicate the 95% confidence level.

Table 6.3 Comparative kinetic parameters of the WT and N23PP *ec*DHFRs.

Parameters	**WT**	**N23PP**
$\boldsymbol{k_{cat}}$ **[s^{-1}]**	12[a]	2.5 ± 1[c]
$\boldsymbol{k_H}$ **[s^{-1}]**	220 ± 10[a]	14.2 ± 1[c]
$\mathbf{A_H/A_T}$	7.0 ± 1.5[b]	2.31 ± 0.16[d]
$\boldsymbol{\Delta E_{aT\text{-}H}}$**, [kcal/mol]**	-0.1 ± 0.2[b]	0.78 ± 0.04[d]

Note: The two rates k_{cat} and k_H are the observed values determined at pH 7 and 25 ˚C. The two isotopic activation parameters A_H/A_T and $\Delta E_{a\ T\text{-}H}$ are obtained from the fitting of the intrinsic KIEs to the Arrhenius equation.

[a] Ref. [6].

[b] Ref. [83].

[c] Ref. [1].

[d] This work.

CHAPTER 7.
SUMMARY, IMPACT AND FUTURE DIRECTIONS

The central motivation for the research in this thesis is to better understand the role of dynamics and the extent of hydrogen tunneling in enzymatic system. Contemporary theories such as Marcus-like models propose that enzymes with temperature independent KIEs (*i.e.*, most wild type enzymes, like WT *ec*DHFR), have optimally organized active-site structure. Perturbations—such as deviations from the physiological temperature/pressure or certain mutations—can lead to temperature dependent KIEs. According to Marcus-like models, temperature dependence of KIEs mostly reflects the deviation of the donor-acceptor distance (DAD) from the optimal value, which is modulated by certain motions in the active site. To further investigate this hypothesis we studied the physical features of a C-H→C transfer by vigorously perturbing the DAD. Experiments completed and discussed in Chapters 3 and 5 were designed to alter the DAD and its dynamics *via* systematic reduction in the size of the two hydrophobic active site residues. The major goal of the study was to examine some basic assumptions in physical chemistry and enzymology and provide a benchmark for the C-H→C transfer reactions, not just enzymatic reactions, but also give some implications for solution reactions in general. The role of the dynamics in the enzymatic reaction was examined indirectly via temperature dependence of KIEs, and not by actually characterizing the active site fluctuations (*i.e.*, spectroscopically or otherwise) that might be on the same timescale as the reaction and therefore relevant to the chemistry.

Prior to conducting the KIEs, it was necessary to obtain pure isotopically labeled reagents. As those are not commercially available we had to develop appropriate synthetic methodologies. Certain synthetic and analytical procedures were already

available, however, due to the commercial unavailability of the required starting material we developed new, faster and cheaper synthetic methods for the isotopically labeled nicotinamides (Chapter 2). These compounds can be used for kinetic and KIE measurements of all nicotinamide cofactor dependent enzymes and are of great general importance in the field of mechanistic enzymology.

Subsequently, the KIE experiments were measured under competitive conditions as it was previously done for WT *ec*DHFR and other distal mutants. Initial work focused on examining the nature of the hydride transfer in the WT *ec*DHFR—one of the first enzymes in which it was shown that the hydride transfer occurs through quantum mechanical tunneling. This work was followed by the study on distal mutants which tackled the question of the existence of the global network of residues in *ec*DHFR whose motions collectively contribute to the hydride transfer reaction in the active site. Mutations of those residues led to temperature dependent KIEs which in the view of Marcus-like models suggested deviation of the average DAD from the optimal value and alteration of its dynamics. In order to further test that hypothesis we completed experiments where the DAD and its dynamics were altered in a more controlled manner, by reducing the size of the two hydrophobic residues, I14 and F31, which are situated behind the cofactor and substrate respectively. Since both residues are hydrophobic and were systematically reduced to smaller hydrophobic amino acids, this experimental design allowed for a controlled change with minimal alteration of the active-site electrostatics, enabling us to establish a correlation between the size of the residue and observed kinetics. Such a controlled structure-function-dynamics study is an extremely difficult task to achieve. Molecular dynamic (MD) simulations were performed on these mutants in order to provide detailed microscopic description of the active site structural changes upon mutation. Since MD simulations suggested that distribution of the DADs at the ground state changes for different mutants, we decided to obtain the X-ray crystal structures of the proposed Michaelis complex for each of the mutants as presented in

Chapter 4. The initial goal was to determine crystal structures for all mutants in the ternary complex with $NADP^+$ and folate within single crystal packing so that distortions due to crystal-packing effects remained constant for the series of structures. Yet, that proved to be quite challenging and currently unattainable for I14A and I14V mutants (whose crystal structures were obtained in the "inactive" form of the ternary Michaelis complex). However, it was attainable for the "most extreme" mutant, I14G, whose X-ray crystal structure indicated that the mutation led to a significant disorder of one of the crucial flexible loops as well as of the nicotinamide ring of the $NADP^+$. Efforts are currently underway to improve both the quality of the crystals as well as to obtain crystals of different crystal morphologies. The long-term goal is to collect X-ray diffraction data on high-quality crystals (<1.3Å) at 100 and 273 K in order to determine the temperature dependence of the anisotropic B-factors for each of the mutants.

The last project focused on N23PP mutant, which was coined in the field as a dynamic knockout mutant since certain mili-microsecond timescale motions in the active site were abrogated due to mutation. This enzyme was examined by measuring the temperature dependence of KIEs in order to determine if the mutation affects also the nature of the hydride transfer. By showing that N23PP mutant exhibits temperature dependent KIEs unlike WT *ec*DHFR, we were able to abate the controversy in the field regarding the effect of this mutation on the chemical step (breaking and forming of the chemical bond). According to the Marcus-like model, these results indirectly suggest that mutation affects the dynamics occurring on the same timescale as the chemical step, similarly as it was observed for the series of I14 mutants, but to a different extent.

Several independent studies examined the nature of the H-transfers in the enzymatic systems and implemented Marcus-like models to rationalize the experimental results, however the enzyme motions that were suggested to be coupled to H-transfer were not measured. Future studies therefore will focus on measurements of relevant dynamics to identify whether the dynamics predicted by the Marcus-like models, or MD

and QM/MM/MD simulations correlate with kinetic findings. A broad timescale (femto – millisecond) of dynamics will be examined for all the mutants using both vibrational and NMR spectroscopies, as well as QM/MM calculations. More specifically, fast dynamics at the active site will be measured by two-dimensional infrared spectroscopy (2D-IR), as it was previously done for the formate dehydrogenase.[125] As these experiments require development of necessary IR probes, current efforts are focused in that direction, with two IR probes under testing.

On the other hand, NMR relaxation experiments will be implemented to obtain detailed site-specific information about protein dynamics at timescales ranging from nanoseconds to milliseconds (ns-ms), through examination of relaxation parameters such as the general order parameter (S^2), effective correlation time for internal motion (τ_ε), contribution to spin-spin relaxation through ^{15}N exchange broadening (*R*ex), and other methods which have been previously applied to *ec*DHFR. In addition to the more common α-^{13}C and ^{15}N-amide labeling NMR relaxation studies will also use labeled side chains, which could be even more relevant in elucidating dynamic effects that are coupled to the chemical step. Different NMR studies will focus on DAD using NOEs between ligands and spin relaxation of sites within the ligands. Such studies will yield information regarding the average DAD and ns-ms dynamics of the donor and acceptor environment. The MD studies of DHFR (Chapter 3), suggest that the differences in average DADs for I, A, and G in position 14 should be well within NOE detection and resolution limits. Lastly, we will also extend our efforts to other active site residues, such as I94, that is in contact with pterin ring of H_2F and was recently suggested to also contribute in keeping the donor and acceptor in close proximity.[17] Initially the I94A mutant will be examined followed by the double mutant I14A/I94A using the same methodologies. We believe that the dynamic picture that will emerge from these combined computational, kinetic and spectroscopic experiments will indicate which

dynamics correlate to effects on the hydride transfer and, ultimately, will yield a more comprehensive picture of enzyme reactivity.

BIBLIOGRAPHY

(1) Bhabha, G.; Lee, J.; Ekiert, D. C.; Gam, J.; Wilson, I. A.; Dyson, H. J.; Benkovic, S. J.; Wright, P. E. A dynamic knockout reveals that conformational fluctuations influence the chemical step of enzyme catalysis. *Science* **2011**, *332*, 234-238.

(2) Warlick, C. A.; Sweeney, C. L.; McIvor, R. S. Maintenance of differential methoxtrexate toxicity between cells expressing drug-resistant and wild-type dihydrofolate reductase activities in the presence of nucleosides through nucleoside transport inhibition. *Biochem. Pharmacol.* **2000**, *59*, 141-151.

(3) Lee, J.; Natarajan, M.; Nashine, V. C.; Socolich, M.; Vo, T.; Russ, W. P.; Benkovic, S. J.; Ranganathan, R. Surface Sites for Engineering Allosteric Control in Proteins. *Scince* **2008**, *322*, 438-442.

(4) Sawaya, M. R.; Kraut, J. Loop and subdomain movements in the mechanism of *Escherichia coli* dihydrofolate reductase: crystallographic evidence. *Biochemistry* **1997**, *36*, 586-603.

(5) Boehr, D. D.; McElheny, D.; Dyson, H. J.; Wright, P. E. The dynamic energy landscape of dihydrofolate reductase catalysis. *Science* **2006**, *313*, 1638-1642.

(6) Fierke, C. A.; Johnson, K. A.; Benkovic, S. J. Construction and evaluation of the kinetic scheme associated with dihydrofolate reductase from *Escherichia coli*. *Biochemistry* **1987**, *26*, 4085-4092.

(7) Miller, G. P.; Benkovic, S. J. Stretching exercises--flexibility in dihydrofolate reductase catalysis. *Chem. Biol.* **1998**, *5*, R105-R113.

(8) Castillo, R.; Andrés, J.; V., M. Catalytic mechanism of dihydrofolate reductase enzyme. A combined quantum-mechanical/molecular-mechanical characterization of transition state structure for the hydride transfer step. *J. Am. Chem. Soc.* **1999**, *121*, 12140–12147.

(9) Ferrer, S.; Silla, E.; Martı, S.; Moliner, V. Catalytic mechanism of dihydrofolate reductase enzyme. A combined quantum-mechanical/molecular-mechanical characterization of the N5 protonation step. *J. Phys. Chem. B.* **2003**, *107*, 14036–14041.

(10) Loveridge, E. J.; Allemann, R. K. Effect of pH on hydride transfer by Escherichia coli dihydrofolate reductase. *ChemBioChem* **2011**, *12*, 1258–1262.

(11) Rod, T. H.; Radkiewicz, J. L.; Brooks, C. L. Correlated motion and the effect of distal mutations in dihydrofolate reductase. *Proc. Natl. Acad. Sci. U.S.A.* **2003**, *100*, 6980-6985.

(12) Chen, Y. Q.; Kraut, J.; Blakley, R. L. C., R. Determination by Raman spectroscopy of the pK_a of N5 of dihydrofolate bound to dihydrofolate reductase: mechanistic implications. *Biochemistry* **1994**, *33*, 7021-7026.

(13) Falzone, C. J.; Wright, P. E.; Benkovic, S. J. Dynamics of a flexible loop in dihydrofolate reductase from Escherichia coli and its implication for catalysis. *Biochemistry* **1994**, *33*, 439-442.

(14) Cannon, W. R.; Garrison, B. J.; Benkovic, S. J. Electrostatic characterization of enzyme complexes: evaluation of the mechanism of catalysis of dihydrofolate reductase. *J. Am. Chem. Soc.* **1997**, *119*, 2386-2395.

(15) Schnell, J. R.; Dyson, H. J.; Wright, P. E. Effect of cofactor binding and loop conformation on side chain methyl dynamics in Dihydrofolate Reductase. *Biochemistry* **2004**, *43*, 374–383.

(16) Radkiewicz, J. L.; Brooks III, C. L. Protein dynamics in enzymatic catalysis: exploration of dihydrofolate reductase. *J. Am. Chem. Soc.* **2000**, *122*, 225-231.

(17) Arora, K.; Brooks, C. L. I. Functionally important conformations of the Met20 loop in dihydrofolate reductase are populated by rapid thermal fluctuations. *J. Am. Chem. Soc.* **2009**, *131*, 5642-5647.

(18) Wong, K. F.; Selzer, T.; Benkovic, S. J.; Hammes-Schiffer, S. Chemical theory and computation special feature: impact of distal mutations on the network of coupled motions correlated to hydride transfer in dihydrofolate reductase. *Proc. Natl. Acad. Sci. U.S.A.* **2005**, *102*, 6807-6812.

(19) Agarwal, P. K.; Webb, S. P.; Hammes-Schiffer, S. Computational studies of the mechanism for proton and hydride transfer in liver alcohol dehydrogenase. *J. Am. Chem. Soc.* **2000**, *122*, 4803-4812.

(20) Cook, P. F. *Enzyme Mechanism from Isotope Effects*; CRC Press: Boca Raton, Fl., 1991.

(21) Cleland, W. W. Measurement of isotope effects by the equilibrium perturbation technique. *Methods in Enzymol.* **1980**, *64*, 104-125.

(22) Huskey, W. P.; Schowen, R. L. Reaction-coordinate tunneling in hydride transfer reactions. *J. Am. Chem. Soc.* **1983**, *105*, 5704-5706.

(23) Kohen, A.; Jensen, J. H. Boundary conditions for the Swain-Schaad relationship as a criterion for hydrogen tunneling. *J. Am. Chem. Soc.* **2002**, *124*, 3858-3864.

(24) Cha, Y.; Murray, C. J.; Klinman, J. P. Hydrogen tunneling in enzyme reactions. *Science* **1989**, *243*, 1325-1330.

(25) Kohen, A. Kinetic isotope effects as probes for hydrogen tunneling, coupled motion and dynamics contributions to enzyme catalysis. *Prog. React. Kin. Mech.* **2003**, *28*, 119-156.

(26) Klinman, J. P. Quantum mechanical effects in enzyme-catalyzed hydrogen transfer reaction. *Trends Biochem. Sci.* **1989**, *14*, 368-373.

(27) Kohen, A.; Klinman, J. P. Enzyme catalysis: beyond classical paradigms. *Acc. Chem. Res.* **1998**, *31*, 397-404.

(28) Kohen, A.; Klinman, J. P. Hydrogen tunneling in biology. *Chem. Biol.* **1999**, *6*, R191-198.

(29) Melander, L.; Saunders, W. H. *Reaction rates of isotopic molecules*; 4th ed.; Krieger, R.E.: Malabar, FL, 1987.

(30) Swain, C. G.; Stivers, E. C.; Reuwer, J. F.; Schaad, L. J. Swain Schaad relationship. *J. Am. Chem. Soc.* **1958**, *80*, 5885.

(31) Saunders, W. H. The Swain Schaad relationship in elimination reactions. *J. Am. Chem. Soc.* **1985**, *107*, 164-169.

(32) Huskey, W. P. Origin of apparent Swain-Schaad deviations in criteria for tunneling. *J. Phys. Org. Chem.* **1991**, *4*, 361-366.

(33) Bigeleisen, J.; Wolfsberg, M. Theoretical and experimental aspects of isotope effects in chemical kinetics. *Adv. Chem. Phys.* **1958**, *1*, 15-76.

(34) Cleland, W. W., Multiple isotope effects in enzyme-catalyzed reactions In *Enzyme Mechanism from Isotope Effects*; Cook, P. F., Ed.; CRC Press: Boca Raton, Fl., 1991, p 247-268.

(35) Northrop, D. B., Intrinsic isotope effects in enzyme catalyzed reactions In *Enzyme mechanism from isotope effects*; Cook, P. F., Ed.; CRC Press: Boca Raton, Fl., 1991, p 181-202.

(36) Cook, P. F., Kinetic and regulatory mechanisms of enzymes from isotope effects In *Enzyme Mechanism from Isotope Effects*; Cook, P. F., Ed.; CRC Press: Boca Raton, Fl., 1991, p 203-230.

(37) Cleland, W. W., Enzyme mechanisms from isotope effects In *Isotope effects in chemistry and biology*; Kohen, A., Limbach, H. H., Eds.; Taylor & Francis, CRC Press: Boca Raton, FL, 2006; Vol. Ch. 37, p 915-930.

(38) Cleland, W. W. *Adv. Enzymol.* **1977**, *45*, 273-303.

(39) Nagel, Z. D.; Klinman, J. P. Update 1 of: Tunneling and dynamics in enzymatic hydride transfer. *Chem. Rev.* **2010**, *110*, PR41-67.

(40) Kohen, A.; Roston, D.; Stojković, V.; Wang, Z., Kinetic Isotope Effects in Enzymes In *Encyclopedia of Analytical Chemistry*; Meyers, R. A., Ed.; John Wiley & Sons, Ltd: Chichester, UK, 2011; Vol. S1-S3, p 77-99.

(41) Stojković, V.; Kohen, A. Enzymatic H-transfers: Quantum Tunneling and Coupled Motion from Kinetic Isotope Effect Studies. *Isr. J. Chem.* **2009**, *49*, 163-173.

(42) Sen, A.; Kohen, A., Quantum effects in enzyme kinetics In *Quantum tunneling in enzyme catalyzed reactions*; Allemann, R., Scrutton, N., Eds.; Royal Society of Chemistry: London, UK, 2009; Vol. CH. 6, p 161-178.

(43) Bell, R. P. *The tunnel effect in chemistry*; Chapman & Hall: London & New York., 1980.

(44) Truhlar, D. G. Tunneling in enzymatic and nonenzymatic hydrogen transfer reactions. *J. Phys. Org. Chem.* **2010**, *23*, 660–676.

(45) Alhambra, C.; Corchado, J. C.; Sanchez, M. L.; Gao, J.; Truhlar, D. G. Quantum dynamics of hydride transfer in enzyme catalysis. *J. Am. Chem. Soc.* **2000**, *122*.

(46) Alhambra, C.; Corchado, J.; Sanchez, M. L.; Garcia-Viloca, M.; Gao, J.; Truhlar, D. G. Canonical variational theory for enzyme kinetics with the protein mean force and multidimensional quantum mechanical tunneling dynamics. Theory and application to liver alcohol dehydrogenase. *J. Phys. Chem. B* **2001**, *105*, 11326–11340.

(47) Cui, Q.; Elstner, M.; Karplus, M. A theoretical analysis of the proton and hydride transfer in liver alcohol dehydrogenase (LADH). *J. Phys. Chem. B* **2002**, *106*, 2721-2740.

(48) Antoniou, D.; Schwartz, S. D. Internal enzyme motions as a source of catalytic activity: rate-promoting vibrations and hydrogen tunneling. *J. Phys. Chem. B* **2001**, *105*, 5553-5558.

(49) Pu, J.; Ma, S.; Garcia-Viloca, M.; Gao, J.; Truhlar, D. J.; Kohen, A. Nonperfect synchronization of reaction center rehybridization in the transition state of the hydride transfer catalyzed by dihydrofolate reductase. *J. Am. Chem. Soc.* **2005**, *127*, 14879-14886.

(50) Kanaan, N.; Martí, M.; Moliner, V.; Kohen, A. A QM/MM study of the catalytic mechanism of the thymidylate synthase. *Biochemistry* **2006**, *46*, 3704-3713.

(51) Kanaan, N.; Marti, S.; Moliner, V.; Kohen, A. QM/MM Study of Thymidylate Synthase: Enzymatic Motions and the Temperature Dependence of the Rate Limiting Step. *Journal of Physical Chemistry A* **2009**, *113*, 2176-2182.

(52) Sutcliffe, M. J.; Scrutton, N. S. A new conceptual framework for enzyme catalysis: Hydrogen tunneling coupled to enzyme dynamics in flavoprotein and quinoprotein enzymes. . *Eur. J. Biochem.* **2002**, *13*, 3096-3102.

(53) Francisco, W. A.; Knapp, M. J.; Blackburn, N. J.; Klinman, J. P. Hydrogen tunneling in peptidylglycine-hydroxylating monooxygenase. *J. Am. Chem. Soc.* **2002**, *124*, 8194-8195.

(54) Caratzoulas, S.; Schwartz, S. C. A computational method to discover the existence of promoting vibrations for chemical reactions in condensed phases. *J. Chem. Phys.* **2001**, *114*, 2910-2918.

(55) Borgis, D.; Hynes, J. T. Molecular-Dynamics Simulation For a Model Nonadiabatic Proton Transfer Reaction in Solution. *J. Chem. Phys.* **1991**, *94*, 3619-3628.

(56) Borgis, D.; Hynes, J. T. Dynamical theory of proton tunneling transfer rates in solution - general formulation. *Chem. Phys.* **1993**, *170*, 315-346.

(57) Kuznetsov, A.; Ulstrup, J. Proton and hydrogen atom tunneling in hydrolytic and redox enzyme catalysis. *Can. J. Chem.* **1999**, *77*, 1085-1096.

(58) Warshel, A.; Olsson, M. H. M.; Villa-Freixa, J., Computer simulations of isotope effets in enzyme catalysis In *Isotope effects in chemistry and biology*; Kohen, A., Limbach, H. H., Eds.; Taylor & Francis, CRC Press: Boca Raton, FL, 2006, p 621-644.

(59) Hatcher, E.; Soudackov, A. V.; Hammes-Schiffer, S. Proton-coupled electron transfer in soybean lipoxygenase. *J. Am. Chem. Soc.* **2004**, *126*, 5763-5775.

(60) Hatcher, E.; Soudackov, A. V.; Hammes-Schiffer, S. Proton-coupled electron transfer in soybean lipoxygenase: dynamical behavior and temperature dependence of kinetic isotope effects. *J. Am. Chem. Soc.* **2007**, *129*, 187-196.

(61) Agarwal, P. K.; Webb, S. P.; Hammes-Schiffer, S. Computational studies of the mechanism for proton and hydride transfer in liver alcohol dehydrogenase. *J. Am. Chem. Soc.* **2000**, *122*, 4803–4812.

(62) Villa, J.; Warshel, A. Energetics and dynamics of enzymatic reactions. *J. Phys. Chem B* **2001**, *105*, 7887-7907.

(63) Liu, H.; Warshel, A. Origin of the temperature dependence of isotope effects in enzymatic reactions: the case of dihydrofolate reductase. *J. Phys. Chem. B* **2007**, *111*, 7852-7861.

(64) Agarwal, P. K.; Billeter, S. R.; Hammes-Schiffer, S. Nuclear quantum effects and enzyme dynamics in dihydrofolate reductase catalysis. *J. Phys. Chem. B* **2002**, *106*, 3283-3293.

(65) Kanaan, N.; Ferrer, S.; Marti, S.; Garcia-Viloca, M.; Kohen, A.; Moliner, V. Temperature Dependence of the Kinetic Isotope Effects in Thymidylate Synthase. A Theoretical Study. *J. Am. Chem. Soc.* **2011**, *133*, 6692-6702.

(66) Pudney, C. R.; Johannissen, L. O.; Sutcliffe, M. J.; Hay, S.; Scrutton, N. S. Direct Analysis of Donor-Acceptor Distance and Relationship to Isotope Effects and the Force Constant for Barrier Compression in Enzymatic H-Tunneling Reactions. *J. Am. Chem. Soc.* **2010**, *132*, 11329-11335.

(67) Knapp, M. J.; Rickert, K. W.; Klinman, J. P. Temperature-dependent isotope effects in soybean lipoxygenase-1: Correlating hydrogen tunneling with protein dynamics. *J. Am. Chem. Soc.* **2002**, *124*, 3865-3874.

(68) Meyer, M. J.; Tomchick, D. R.; Klinman, J. P. Enzyme structure and dynamics affect hydrogen tunneling: the impact of a remote side chain (I553) in soybean lipoxygenase-1. *Proc. Natl. Acad. Sci. USA* **2008**, *105*, 1146-1151.

(69) Hay, S.; Scrutton, N. S. Incorporation of hydrostatic pressure into models of hydrogen tunneling highlights a role for pressure-modulated promoting vibrations. *Biochemistry* **2008**, *47*, 9880-9887.

(70) Knapp, M. J.; Rickert, K.; Klinman, J. P. Temperature-dependent isotope effects in soybean lipoxygenase-1: Correlating hydrogen tunneling with protein dynamics. *J. Am. Chem. Soc.* **2002**, *124*, 3865-3874.

(71) Meyer, M. P.; Tomchick, D. R.; Klinman, J. P. Enzyme structure and dynamics affect hydrogen tunneling: The impact of a remote side chain (I553) in soybean lipoxygenase-1. *Proc. Nat. Acad. Sci. U.S.A.* **2007**, *105*, 1146-1151.

(72) Roston, D.; Kohen, A. Elusive transition state of alcohol dehydrogenase unveiled *Proc. Natl. Acad. Sci.* **2010**, *107*, 9572-9577.

(73) Roston, D.; Cheatum, C. M.; Kohen, A. Hydrogen donor-acceptor fluctuations from kinetic isotope effects: a phenomenological model. *Biochemistry* **2012**, *51*, 6860-6870.

(74) Kohen, A., Kinetic isotope effects as probes for hydrogen tunneling in enzyme catalysis In *Isotope effects in chemistry and biology*; Kohen, A., Limbach, H. H., Eds.; Taylor & Francis, CRC Press: Boca Raton, FL, 2006; Vol. Ch. 28, p 743-764.

(75) Roston, D.; Wang, Z.; Kohen, A., Experimental and theoretical studies of enzyme-catalyzed hydrogen transfer reactions. In *Structural and mechanistic enzymology: Bringing together experiments and computing.*; Christov, C. Z., Karabencheva, T., Eds.; Burlington, Academic Press, Elsevier Inc.: 2012; Vol. 87, p 155-180.

(76) Masgrau, L., Roujeinikova, A., Johannissen, L. O., Hothi, P., Basran, J., Ranaghan, K. E., Mulholland, A. J., Sutcliffe, M J., Scrutton, N. S., Leys, D. Atomic Description of an Enzyme Reaction Dominated by Proton Tunneling. *Science* **2006**, *312*, 237-241.

(77) Basran, J., Sutcliffe, M. J., Scrutton, N. S. Enzymic H-Transfer Requires Vibration-Driven Extreme Tunneling. *Biochemistry* **1999**, *38*, 3218-3222.

(78) Basran, J., Sutcliffe, M. J., Scrutton, N. S. Deuterium isotope effects during carbon-hydrogen bond cleavage by trimethylamine dehydrogenase: implications for mechanism and vibrationally assisted hydrogen tunneling in wild-type and mutant enzymes *J. Biol. Chem.* **2001**, *276*, 24581-24587.

(79) Harris, R. J., Meskys, R., Sutcliffe, M. J., Scrutton, N. S. Kinetic Studies of the Mechanism of Carbon-Hydrogen Bond Breakage by the Heterotetrameric Sarcosine Oxidase of Arthrobacter sp. 1-IN. *Biochemistry* **2000**, *39*, 1189-1198.

(80) Basran, J., Harris, R. J., Sutcliffe, M. J., Scrutton, N. S. H-tunneling in the Multiple H-transfers of the Catalytic Cycle of Morphinone Reductase and in the Reductive Half-reaction of the Homologous Pentaerythritol Tetranitrate Reductase *J. Biol. Chem.* **2003**, *278*, 43973-43982.

(81) Bandarian, V., Reed, G. H. Isotope Effects in the Transient Phases of the Reaction Catalyzed by Ethanolamine Ammonia-Lyase: Determination of the Number of Exchangeable Hydrogens in the Enzyme-Cofactor Complex. *Biochemistry* **2000**, *39*, 12069-12075.

(82) Cheng, M. C., Marsh, E. N. Isotope Effects for Deuterium Transfer between Substrate and Coenzyme in Adenosylcobalamin-Dependent Glutamate Mutase. *Biochemistry* **2005**, *44*, 2686-2691.

(83) Sikorski, R. S.; Wang, L.; Markham, K. A.; Rajagopalan, P. T. R.; Benkovic, S. J.; Kohen, A. Tunneling and coupled motion in the *E. coli* dihydrofolate reductase catalysis. *J. Am. Chem. Soc.* **2004**, *126*, 4778-4779.

(84) Wang, L.; Goodey, N. M.; Benkovic, S. J.; Kohen, A. Coordinated effects of distal mutations on environmentally coupled tunneling in dihydrofolate reductase. *Proc. Nat. Acad. Sci. USA* **2006**, *103*, 15753-15758.

(85) Stojković, V.; Perissinotti, L.; Willmer, D.; Benkovic, S.; Kohen, A. Effects of the donor acceptor distance and dynamics on hydride tunneling in the dihydrofolate reductase catalyzed reaction. *J. Am. Chem. Soc.* **2012**, *134*, 1738-1745.

(86) Yahashiri, A.; Howell, E. E.; Kohen, A. Tuning of the H-Transfer Coordinate in Primitive vs. Well-Evolved Enzymes. *ChemPhysChem* **2008**, *9*, 980 – 982.

(87) Bandaria, J. N.; Cheatum, C. M.; Kohen, A. Examination of enzymatic H-tunneling through kinetics and dynamics. *J. Am. Chem. Soc.* **2009**, *131*, 10151– 10155.

(88) Agrawal, N.; Lesley, S. A.; Kuhn, P.; Kohen, A. Mechanistic studies of a flavin-dependent thymidylate synthase. *Biochemistry* **2004**, *43*, 10295-10301.

(89) Wang, Z.; Kohen, A. Thymidylate synthase catalyzed H-transfers: Two chapters in one tale. *J. Am. Chem. Soc.* **2010**, *132*, 9820-9825.

(90) Kohen, A.; Cannio, R.; Bartolucci, S.; Klinman, J. P. Enzyme dynamics and hydrogen tunneling in a thermophilic alcohol dehydrogenase. *Nature* **1999**, *399*, 496-499.

(91) Voet, D.; Voet, J. G. *Biochemistry*; 2nd ed.; Wiley, 1995.

(92) Hixson, S. S.; Hixson, S. H. Photochemical labeleing of yeast alcohol dehydrogenase with an azide analog of NAD+. *Photochem. Photobiol.* **1973**, *18*, 135-138.

(93) Cook, P. F.; Oppenheimer, N. J.; Cleland, W. W. Secondary deuterium and nitrogen- 15 isotope effects in enzyme-catalyzed reactions. Chemical mechanism of liver alcohol dehydrogenase? *Biochemistry* **1981**, *20*, 1817-1825.

(94) Stone, S. R.; Mark, A.; Morrison, J. F. Interaction of analogues of nicotinamide adenine dinucleotide phosphate with dihydrofolate reductase from *Escherichia coli*. *Biochemistry* **1984**, *23*, 4340-4346.

(95) Markham, K. A.; Sikorski, R. S.; Kohen, A. Synthesis and utility of ^{14}C-labeled nicotinamide cofactors. *Anal. Biochem.* **2004**, *325*, 62–67.

(96) Woenckhaus, C.; Jeck, R., In *Pyridine nucleotide coenzymes: chemical, biochemical, and medical aspects*; Dolphin, D., Poulson, R., Avramovic, O., Eds.; John Wiley & Sons Inc.: New York, 1987; Vol. 2, p 449-568.

(97) Dutta, S.; Cook, R. J.; Houtman, J. C. D.; Kohen, A.; Cheatum, C. M. Characterization of azo-NAD to assess its potential as a two-dimensional infrared probe of enzyme dynamics. *Anal. Biochem* **2010**, *407*, 241-246.

(98) Markham, K. A.; Kohen, A. Analytical procedures for the preparation, isolation, analysis and preservation of reduced nicotinamides. *Curr. Anal. Chem.* **2006**, *2*, 379-388.

(99) Antikainen, N. M.; Smiley, R. D.; Benkovic, S. J.; Hammes, G. G. Conformation coupled enzyme catalysis: single-molecule and transient kinetics investigation of dihydrofolate reductase. *Biochemistry* **2005**, *44*, 16835-16843.

(100) Stojkovic, V.; Perissinotti, L.; Willmer, D.; Benkovic, S.; Kohen, A. Effects of the donor acceptor distance and dynamics on hydride tunneling in the dihydrofolate reductase catalyzed reaction. *J. Am. Chem. Soc.* **2012**, *134*, 1738-1745.

(101) Wang, L.; Goodey, N. M.; Benkovic, S. J.; Kohen, A. Coordinated effects of distal mutations on environmentally coupled tunneling in dihydrofolate reductase. *Proc. Natl. Acad. Sci. USA* **2006**, *103*, 15753-15758.

(102) Cook, P. F.; Cleland, W. W. *Enzyme kinetics and mechanism*; Taylor & Francis Group LLC: New York, NY, 2007.

(103) Wang, L.; Tharp, S.; Selzer, T.; Benkovic, S. J.; Kohen, A. Effects of a distal mutation on active site chemistry. *Biochemistry* **2006**, *45*, 1383-1392.

(104) Sen, A.; Yahashiri, A.; Kohen, A. Triple isotopic labeling and kinetic isotope effects: Exposing H-transfer steps in enzymatic systems. *Biochemistry* **2011**, *50*, 6462-6468.

(105) Schramm, V. L. Binding isotope effects: boon and bane. *Curr. Opin. Chem. Biol.* **2007**, *11*, 529-536.

(106) Cameron, C. E.; Benkovic, S. J. Evidence for a functional role of the dynamics of glycine-121 of Escherichia coli dihydrofolate reductase obtained from kinetic analysis of a site-directed mutant. *Biochemistry* **1997**, *36*, 15792-15800.

(107) Blakley, R. L. Crystalline dihydropteroylglutamic acid. *Nature* **1960**, *188*, 231-232.

(108) Kohen, A.; Jonsson, T.; Klinman, J. P. Effect of protein glycosylation on catalysis: changes in hydrogen tunneling and enthalpy of activation in the glucose oxidase reaction. *Biochemistry* **1997**, *36*, 2603-2611.

(109) Markham, K. A.; Sikorski, R. S.; Kohen, A. Purification, analysis, and preservation of reduced nicotinamide adenine dinucleotide 2'-phosphate. *Anal. Biochem.* **2003**, *322*, 26-32.

(110) Yahashiri, A.; Sen, A.; Kohen, A. Microscale synthesis and kinetic isotope effect analysis of (4R)-[Ad-^{14}C, 4-^{2}H] NADPH and (4R)-[Ad-^{3}H,4-^{2}H] NADPH. *J. Labelled Compd. Radiopharm.* **2009**, *52*, 463-466.

(111) McCracken, J. A.; Wang, L.; Kohen, A. Synthesis of R and S tritiated reduced *β*-nicotinamide adenine dinucleotide 2' phosphate. *Anal. Biochem.* **2003**, *324*, 131-136.

(112) Agrawal, N.; Kohen, A. Microscale synthesis of 2-tritiated isopropanol and 4R-tritiated reduced nicotinamide adenine dinucleotide phosphate. *Anal. Biochem.* **2003**, *322*, 179-184.

(113) Ben-Hayyim, G.; Hochman, A.; Avron, M. Phosphoadenosine diphosphate ribose, a specific inhibitor of nicotinamide adenine dinucleotide phosphate enzymes. *J. Biol. Chem.* **1967**, *242*, 2837-2839.

(114) Pauling, L. Nature of forces between large molecules of biological interest. *Nature* **1948**, *161*, 707-709.

(115) Here we define dynamics as any motion along the reaction coordinate and not as only non-equilibrium motions.

(116) Schwartz, S. D., Vibrationally enhanced tunneling from the temperature dependence of KIE In *Isotope effects in chemistry and biology*; Kohen, A., Limbach, H. H., Eds.; Taylor & Francis, CRC Press: Boca Raton, FL, 2006; Vol. Ch. 18, p 475-498.

(117) Truhlar, D. G., Variational transition state theory and multidimensional tunneling for simple and complex reacrions in the gas phase, solids, Liquids, and enzymes In *Isotope effects in chemistry and biology*; Kohen, A., Limbach, H. H., Eds.; Taylor & Francis, CRC Press: Boca Raton, FL, 2006; Vol. Ch. 22, p 579-620.

(118) Kiefer, P. M.; Hynes, J. T., Interpretation of primary kinetic isotope effects for adiabatic and nonadiabatic proton-transfer reactions in a polar environment In *Isotope effects in chemistry and biology*; Kohen, A., Limbach, H. H., Eds.; Taylor & Francis, CRC Press: Boca Raton, FL, 2006; Vol. Ch. 21, p 549-578.

(119) Sutcliffe, M. J.; Masgrau, L.; Roujeinikova, A.; Johannissen, L. O.; Hothi, P.; Basran, J.; Ranaghan, K. E.; Mulholland, A. J.; Leys, D.; Scrutton, N. S. Hydrogen tunnelling in enzyme-catalyzed H-transfer reactions: flavoprotein and quinoprotein systems. *Philos. Trans. R. Soc. B, Biol. Sci.* **2006**, *361*, 1375-1386.

(120) Fan, F.; Gadda, G. Oxygen- and Temperature-Dependent Kinetic Isotope Effects in Choline Oxidase: Correlating Reversible Hydride Transfer with Environmentally Enhanced Tunneling. *J. Am. Chem. Soc.* **2005**, *127*, 17954–17961.

(121) Boehr, D. D.; McElheny, D.; Dyson, H. J.; Wright, P. E. The dynamic energy landscape of dihydrofolate reductase catalysis. *Science* **2006**, *313*, 1638-1642.

(122) Hammes-Schiffer, S., Selected Theoretical Models and Computational Methods for Enzymatic Tunnelling In *Quantum Tunnelling in Enzyme-Catalysed Reactions*; Allemann, R. K., Scrutton, N. S., Eds.; Royal Society of Chemistry: Cambridge, 2009, p 79-104.

(123) Nagel, Z. D.; Dong, M.; Bahnson, B. J.; Klinman, J. P. Impared protein conformational landscapes as revealed in anomalous Arrhenius prefactors. *Proc. Natl. Acad. Sci. U.S.A.* **2011**, *108*, 10520-10525.

(124) Hay, S.; Sutcliffe, M. J.; Scrutton, N. S., Probing coupled motions in enzymatic hydrogen tunnelling reactions: beyond temperature-dependence studies of kinetic isotope effects. In *Quantum Tunnelling in Enzyme-Catalysed Reactions* Scrutton, N. S., Allemann, R. K., Eds.; RSC Publishing: 2009, p 199-218.

(125) Bandaria, J. N.; Dutta, S.; Nydegger, M. W.; Rock, W.; Kohen, A.; Cheatum, C. M. Characterizing the dynamics of functionally relevant complexes of formate dehydrogenase. *Proc Natl Acad Sci USA* **2010**, *107*, 17974-17979.

(126) Marcus, R. A.; Sutin, N. Electron transfer in chemistry and biology. *Biochem. Biophys. Acta* **1985**, *811*, 265-322.

(127) Marcus, R. A. H and other transfers in enzymes and in solution: theory and computations, a unified View. 2. Applications to experiment and computations. *J. Phys. Chem. B.* **2007**, *111*, 6643-6654.

(128) Francisco, W. A., Knapp, M. J., Blackburn, N. J., Klinman, J. P. Hydrogen Tunneling in Peptidylglycine .alpha.-Hydroxylating Monooxygenase. *J Am Chem Soc* **2002**, *124*, 8194-8195.

(129) Antoniou, D.; Caratzoulas, S.; Kalyanaraman, C.; Mincer, J. S.; Schwartz, S. D. Barrier passage and protein dynamics in enzymatically catalyzed reactions. *Eur. J. Biochem.* **2002**, *269*, 3103–3112.

(130) Hammes-Schiffer, S. Hydrogen tunneling and protein motion in enzyme reactions. *Acc. Chem. Res.* **2006**, *39*, 93-100.

(131) Two different, yet related DADs are used in this paper: The first, DAD_e, represents the donor-acceptor distance in the energy space, i.e., the distance between the hydrogen in the reactant state and in the product state (e.g., Figure 1, the double-well system along the DHA coordinate). DAD_e depends on the overlap between the electronic orbitals of the donor and acceptor, and is most relevant to the kinetic measurements presented here. The second, DAD_c, refers to the donor-acceptor distance between two carbons that donate, or accept the hydride. The DADc is the one addressed in the structures and MD calculations. The importance of the orbital steering in catalysis has been previously shown (e.g., Mesecar, A. D.; Stoddard, B. L.; Koshland, D. E. *Science* **1997**, **1***227*, **1**202-**1**206). DAD_c relates to DAD_e, through the DHA angle and the C-H distance at each stage of the reaction coordinate. E.g., when the DHA angle is **1**180˚ and the C-H is in its ground state (~**199**1.**19**04 Å) for both reactant and product, than $DAD_c = DAD_e$ + **199**2 x **199**1.**19**04 Å. Also, when the DHA angle is fixed (on the reaction's time scale), then both DADs' fluctuations are coherent.

(132) Wang, Z.; Kohen, A. Thymidylate synthase catalyzed H-transfers: Two chapters in one tale. *J. Am. Chem. Soc.* **2010**, *132*, 9820-9825.

(133) McCusker, K. P.; Klinman, J. P. An Active-Site Phenylalanine Directs Substrate Binding and C-H Cleavage in the .alpha.-Ketoglutarate-Dependent Dioxygenase TauD. *J. Am. Chem. Soc.* **2010**, *132*, 5114-5120.

(134) Bahnson, B. J.; Colby, T. D.; Chin, J. K.; Goldstein, B. M.; Klinman, J. P. A Link between protein structure and enzyme catalyzed hydrogen tunneling. *Proc. Nat. Acad. Sci. Usa.* **1997**, *94*, 12797-12802.

(135) Colby, T. D.; Bahnson, B. J.; Chin, J. K.; Klinman, J. P.; Goldstein, B. M. Active site modifications in a double mutant of liver alcohol dehydrogenase: structural studies of two enzyme-ligand complexes. *Biochemistry* **1998**, *37*, 9295-9304.

(136) Pudney, C. R.; McGrory, T.; Lafite, P.; Pang, J.; Hay, S.; Sutcliffe, M. J.; Scrutton, N. S. Parallel pathways and free-energy landscapes for enzymatic hydride transfer probed by hydrostatic pressure. *ChemBioChem* **2009**, *10*, 1379-1384.

(137) Fierke, C. A.; Benkovic, S. J. Probing the functional role of threonine-113 of Escherichia coli dihydrofolate reductase for its effect on turnover efficiency, catalysis, and binding. *Biochemistry* **1989**, *28*, 478-486.

(138) Wang, L.; Goodey, N. M.; Benkovic, S. J.; Kohen, A. The role of enzyme dynamics and tunneling in catalyzing hydride transfer: Studies of distal mutants of dihydrofolate reductase. *Phil. Trans. R. Soc. B* **2006**, *361*, 1307-1315.

(139) Radkiewicz, J.; Brooks, C. Protein dynamics in enzymatic catalysis: exploration of dihydrofolate reductase. *J. Am. Chem. Soc.* **2000**, *122*, 225-231.

(140) Adams, J. A.; Fierke, C. A.; Benkovic, S. J. The function of amino acid residues contacting the nicotinamide ring of NADPH in dihydrofolate reductase from Escherichia coli. *Biochemistry* **1991**, *30*, 11046-11054.

(141) Stojković, V.; Perissinotti, L. L.; Lee, J.; Benkovic, S. J.; Kohen, A. The effect of active-site isoleucine to alanine mutation on the DHFR catalyzed H-transfer. *Chem. Comm.* **2010**, *46*, 8974-8976.

(142) Yahashiri, A.; Sen, A.; Kohen, A. Microscale synthesis and kinetic isotope effect analysis of (4R)-[Ad-^{14}C, 4-^{2}H] NADPH and (4R)-[Ad-^{3}H,4-^{2}H] NADPH. *J. Labelled Compd. Radiopharm.* **2009**, *52*, 463-466

(143) Case, D. A.; Darden, T. A.; Cheatham, T. E.; Simmerling, C. L.; Wang, J.; Duke, R. E.; Luo, R.; Crowley, M.; Walker, R. C.; Zhang, W.; Merz, K. M.; Wang, B.; Hayik, S.; Roitberg, A.; Seabra, G.; Kolossva´ry, I.; Wong, K. F.; Paesani, F.; Vanicek, J.; Wu, X.; Brozell, S. R.; Steinbrecher, T.; Gohlke, H.; Yang, L.; Tan, C.; Mongan, J.; Hornak, V.; Cui, G.; Mathews, D. H.; Seetin, M. G.; Sagui, C.; Babin, V.; Kollman, P. A. University of California: San Francisco, 2006.

(144) Pearlman, D. A.; Case, D. A.; Caldwell, J. W.; Ross, W. S.; Cheatham III, T. E.; DeBolt, S.; Ferguson, D.; Seibel, G.; Kollman, P. A. "AMBER", a package of computer programs for applying molecular mechanics, normal mode analysis, molecular dynamics and free energy calculations to stimulate the structural and energetic properties of molecules. *Comput. Phys. Commun.* **1995**, *91*, 1-41.

(145) Poe, M.; Hoogsteen, K.; Mathews, D. A. Proton magnetic resonance studies on Escherichia coli dihydrofolate reductase. Assignment of histidine C-2 protons in binary complexes with folates on the basis of the crystal structure with methotrexate and on chemical modifications. *J. Biol. Chem* **1979**, *254*, 8143-8152.

(146) Bystroff, C.; Oatley, S. J.; Kraut, J. Crystal structures of Escherichia coli dihydrofolate reductase: the $NADP^+$ holoenzyme and the folate.$NADP^+$ ternary complex. Substrate binding and a model for the transition state. *Biochemistry* **1990**, *29*, 3263-3277.

(147) Cummins, P. L.; Rammarayan, K.; Singh, U. C. G., J. E. Molecular dynamics/free energy perturbation study on the relative affinities of the binding of reduced and oxidized NADP to dihydrofolate reductase. *J. Am. Chem. Soc.* **1991**, *113*, 8247-8256.

(148) Jensen, J. H.; Li, H.; Bas, D. C.; Rogers, D. M. 2007.

(149) Birdsall, B.; Roberts, G. C. K.; Feeney, J.; Burgen, A. S. V. Phosphorus-31 NMR studies of the binding of adenosine-2'-phosphate to Lactobacillus casei dihydrofolate reductase. *FEBS Lett.* **1977**, *80*, 313-316.

(150) Berendsen, H. J. C.; Postma, J. P. M.; Van Gunsteren, W. F.; DiNola, A.; Haak, J. R. Molecular dynamics with coupling to an external bath. *J. Chem. Phys.* **1984**, *81*, 3684-3690.

(151) Darden, T.; York, D.; Perdersen, L. Particle mesh Ewald: an Nlog(N) method for Ewald sums in large systems. *J. Chem. Phys.* **1993**, *98*, 10089-10092.

(152) Essmann, U.; Perera, L.; Berkowitz, M. L.; Darden, T.; Lee, H.; Pedersen, L. G. A smooth particle mesh Ewald method. *J. Chem. Phys.* **1995**, *103*, 8577-8593.

(153) Ryckaert, J. P.; Ciccotti, G.; Berendsen, H. J. C. Numerical integration of the Cartesian equations of motion of a system with constraints: molecular dynamics of n-alkanes. *J. Comput. Phys.* **1977**, *23*, 327-341.

(154) Cheatham, T. E.; Cieplak, P.; Kollman, P. A. A modified version of the Cornell et al. force field with improved sugar pucker phases and helical repeat. *J. Biomol. Struct. Dyn.* **1999**, *16*, 845-862.

(155) Walker, R. C.; De Souza, M. M.; Mercer, I. P.; Gould, I. R.; Klug, D. R. Large and Fast Relaxations inside a Protein: Calculation and Measurement of Reorganization Energies in Alcohol Dehydrogenase. *J. Phys. Chem. B* **2002**, *106*, 11658-11665.

(156) Wang, J.; Wolf, R. M.; Caldwell, J. W.; Kollamn, P. A.; Case, D. A. Development and testing of a general Amber force field. *J. Comput. Chem.* **2004**, *25*, 1157-1174.

(157) Wang, J.; Cieplak, P.; Kollman, P. A. How well does a restrained electrostatic potential (RESP) model perform in calculating conformational energies of organic and biological molecules? *J. Comput. Chem.* **2000**, *21*, 1049-1074.

(158) Humphrey, W.; Dalke, A.; Schulten, K. VMD - Visual Molecular Dynamics. *J. Molec. Graphics.* **1996**, *14*, 33-38.

(159) Turner, P. J.; Grace Development Team. http://plasma-gate.weizmann.ac.il/Grace/.

(160) Vasilief, I. http://soft.proindependent.com/qtiplot.html.

(161) Ltd., P. o. V. P. In *Persistence of Vision Raytracer* 3.6 ed.; Retrieved from http://www.povray.org/download/:2004.

(162) Wojdyr, M. Fityk: a general-purpose peak fitting program. *J. Appl. Cryst.* **2010**, *43*, 1126-1128.

(163) Hay, S.; Sutcliffe, M. J.; Scrutton, N. S. Promoting motions in enzyme catalysis probed by pressure studies of kinetic isotope effects. *Proc. Natl. Acad. Sci. U.S.A.* **2007**, *104*, 507-512.

(164) Kamerlin, S. C. L.; Mavri, J.; Warshel, A. Examining the case for the effect of barrier compression on tunneling, vibrationally enhanced catalysis, catalytic entropy and related issues. *FEBS Letters* **2010**, *584*, 2759-2766.

(165) Khavrutskii, I. V.; Price, D. J.; Lee, J.; Brooks, C. L. I. Conformational change of the methionine 20 loop of Escherichia coli dihydrofolate reductase modulates pKa of the bound dihydrofolate. *Protein Science* **2007**, *16*, 1087-1100.

(166) Mesecar, A. D.; Stoddard, B. L.; Koshland, D. E. Orbital steering in the ... structural changes with large catalytic consequences. *Science* **1997**, *227*, 202-206.

(167) Garcia-Viloca, M.; Truhlar, D. G.; Gao, J. Reaction-path energetics and kinetics of the hydride transfer reaction catalyzed by dihydrofolate reductase. *Biochemistry* **2003**, *42*, 13558-13575.

(168) Creighton, T. E. *Proteins. Structure and Molecular Principles.*; Freeman: New York, N. Y., 1984.

(169) Andrews, J.; Fierke, C. A.; Birdsall, B.; Ostler, G.; Feeney, J.; Roberts, G. C.; Benkovic, S. J. A kinetic study of wild-type and mutant dihydrofolate reductases from Lactobacillus casei. *Biochemistry* **1989**, *28*, 5743-5750.

(170) Benkovic, S. J.; Fierke, C. A.; Naylor, A. M. Insights into enzyme function from studies on mutants of dihydrofolate reductase. *Science* **1988**, *239*, 1105-1110.

(171) Schnell, J. R.; Dyson, H. J.; Wright, P. E. Structure, dynamics, and catalytic function of dihydrofolate reductase. *Annu. Rev. Biophys. Biomol. Struct.* **2003**, *33*, 119-140.

(172) Reyes, V. M.; Sawaya, M. R.; Brown, K. A.; Kraut, J. Isomorphous crystal structures of Escherichia coli dihydrofolate reductase complexed with folate, 5-deazafolate, and 5,10-dideazatetrahydrofolate: mechanistic implications. *Biochemistry* **1995**, *34*, 2710-2723.

(173) Borgis, D. C.; Lee, S. Y.; Hynes, J. T. A dynamical theory of nonadiabatic proton and hydrogen atom transfer reaction rates in solution. *Chem. Phys. Lett.* **1989**, *162*, 19-26.

(174) Hammes-Schiffer, S., Kinetic isotope effects for proton-coupled electron transfer reactions In *Isotope effects in chemistry and biology*; Kohen, A., Limbach, H. H., Eds.; Taylor & Francis, CRC Press: Boca Raton, FL, 2006; Vol. Ch. 19, p 499-520.

(175) Schwartz, S. D.; Schramm, V. L. Enzymatic transition states and dynamic motion in barrier crossing. *Nat. Chem. Biol.* **2009**, *5*, 551-558.

(176) Hay, S.; Scrutton, N. S. Good vibrations in enzyme-catalyzed reactions. *Nat. Chem.* **2012**, *4*, 161-168.

(177) Wang, Z.; Abeysinghe, T.; Finer-Moore, J. S.; Stroud, R. M.; Kohen, A. A remote mutation affects the hydride transfer by disrupting concerted protein motions in thymidylate synthase. *J. Am. Chem. Soc.* **2012**, *In press*.

(178) Warshel, A.; Olsson, M. H. M.; Villa-Freixa, J., Computer simulations of isotope effects in enzyme catalysis. In *Isotope effects in chemistry and biology*; Kohen, A., Limbach, H. H., Eds.; Taylor & Francis, CRC Press: Boca Raton, FL

, 2006, p 621-644.

(179) Osborne, M. J.; Schnell, J.; Benkovic, S. J.; Dyson, H. J.; Wright, P. E. Backbone dynamics in dihydrofolate reductase complexes: role of loop flexibility in the catalytic mechanism. *Biochemistry* **2001**, *40*, 9846-9859.

(180) McElheny, D.; Schnell, J. R.; Lansing, J. C.; Dyson, H. J.; Wright, P. E. Defining the role of active-site loop fluctuations in dihydrofolate reductase catalysis. *Proc. Nat. Acad. Sci. U.S.A.* **2005**, *102*, 5032-5037.

(181) Agarwal, P. K.; Billeter, S. R.; Rajagopalan, P. T. R.; Benkovic, S. J.; Hammes-Schiffer, S. Network of coupled promoting motions in enzyme catalysis. *Proc. Nat. Acad. Sci. U.S.A.* **2002**, *99*, 2794–2799.

(182) Miller, G. P.; Benkovic, S. J. Deletion of a highly motional residue affects formation of the Michaelis complex for Escherichia coli dihydrofolate reductase. *Biochemistry* **1998**, *37*, 6327-6335.

(183) Pflugrath, J. W. The finer things in X-ray diffrcation data collection. *Acta. Cryst. D* **1999**, *55*, 1718-1725.

(184) Kabsch, W. XDS. *Acta Cryst. D* **2010**, *66*, 125-132.

(185) Collaborative Computational Project, N. The *CCP4* suite: programs for protein crystallography. *Acta. Cryst. D* **1994**, *50*, 760-763.

(186) McCoy, A. J.; Grosse-Kunstleve, R. W.; Adama, P. D.; Winn, M. D.; Storoni, L. C.; Read, R. J. *Phaser* crystallographic software. *J. Appl. Cryst.* **2007**, *40*, 658-674.

(187) Murshundov, G. N.; Vagin, A. A.; Dodson, E. J. Refinement of macromolecular structures by the maximum-likelihood method. *Acta. Cryst. D* **1997**, *53*, 240-255.

(188) Emsley, P.; Cowtan, K. *Coot*: model-building tools for molecular graphics. *Acta. Cryst. D* **2004**, *60*, 2126-2132.

(189) Li, L.; Falzone, C. J.; Wright, P. E.; Benkovic, S. J. Functional role of a mobile loop of Escherichia coli dihydrofolate reductase in transition-state stabilization. *Biochemistry* **1992**, *31*, 7826-7833.

(190) Mauldin, R. V.; Sapienza, P. J.; Petit, C. M.; Lee, A. L. Structure and dynamics of the G121V dihydrofolate reductase mutant: Lessons from a transition-state inhibitor complex. *PLoS ONE* **2012**, *7*, e33252.

(191) Colby, T. D.; Bahnson, B. J.; Chin, J. K.; Klinman, J. P.; Goldstein, B. M. Active site modifications in a double mutant of liver alcohol dehydrogenase: structural studies of two enzyme-ligand complexes. *Biochemistry* **1998**, *37*, 9295-9034.

(192) Johannissen, L. O.; Scrutton, N. S.; Sutcliffe, M. J. How does pressure affect barrier compression and isotope effects in an enzymatic hydrogen tunneling reaction? *Angew. Chem. Int. Ed.* **2011**, *50*, 2129-2132.

(193) Loveridge, E. J.; Behiry, E. M.; Guo, J.; Allemann, R. K. Evidence that a 'dynamic knockout' in Escherichia coli dihydrofolate reductase does not affect the chemical step of catalysis. *Nat. Chem.* **2012**, *4*, 292-297.

(194) Plapp, B. V. Conformational changes and catalysis by alcohol dehydrogenase. *Arch. Biochem. Biophys.* **2010**, *493*, 3-12.

(195) Antoniou, D.; Basner, J.; Nunez, S.; Schwartz, S. D. Computational and theoretical methods to expolore the relation between enzyme dynamics and catalysis. *Che. Rev.* **2006**, *106*, 3170-3187.

(196) Truhlar, D. G. Tunneling in enzymatic and nonenzymatic hydrogen transfer reactions. *J. Phys. Org. Chem.* **2010**, *23*, 660-676.

(197) Liu, H. B.; Warshel, A. Origin of the temperature dependence of isotope effects in enzymatic reactions: The case of dihydrofolate reductase. *J. Phys. Chem. B* **2007**, *111*, 7852-7861.

(198) Pu, J.; Ma, S.; Gao, J.; Truhlar, D. G. Small temperature dependence of the kinetic isotope effect for the hydride transfer reaction catalyzed by Escherichia coli dihydrofolate reductase. *J. Phys. Chem. B.* **2005**, *109*, 8551-8556.

(199) Nagel, Z. D.; Klinman, J. P. Tunneling and dynamics in enzymatic hydride transfer. *Chem. Rev.* **2006**, *106*, 3095 - 3118.

(200) Pudney, C. R.; Johannissen, L. O.; Sutcliffe, M. J.; Hay, S.; Scrutton, N. S. Direct analysis of donor-acceptor distance and relationship to isotope effects and the force constant for barrier compression in enzymatic H-tunneling reactions. *J. Am. Chem. Soc.* **2010**, *132*, 11329–11335.

(201) Hong, B.; Maley, F.; Kohen, A. The role of Y94 in proton and hydride transfers catalyzed by thymidylate synthase. *Biochemistry* **2007**, *46*, 14188-14197.

(202) Liu, H.; Warshel, A. Origin of the temperature dependence of isotope effects in enzymatic reactions: the case of dihydrofolate reductase. *J. Phys. Chem. B* **2007**, *111*, 7852-7861.

(203) Pudney, C. R.; McGrory, T.; Lafite, P.; Pang, J.; Hay, S.; Leys, D.; Sutcliffe, M. J.; Scrutton, N. S. Parallel pathways and free-energy landscapes for enzymatic hydride transfer probed by hydrostatic pressure. *ChemBioChem* **2009**, *10*, 1379-1384.

(204) Mesecar, A. D.; Stoddard, B. L.; Koshland, D. E. Orbital Steering in the Catalytic Power of Enzymes: Small Structural Changes with Large Catalytic Consequences. *Science* **1997**, *277*, 202-206.

(205) Hammes, G. G.; Benkovic, S. J.; Hammes-Schiffer, S. Flexibility, diversity, and cooperativity: Pillars of enzyme catalysis. *Biochemistry* **2011**, *50*, 10422-10430.

(206) Chen, J.; Dima, R. I.; Thirumalai, D. Allosteric communication in dihydrofolate reductase: Signaling neetwork and pathways for closed to occluded transition and back. *J. Mol. Biol.* **2007**, *374*, 250-266.

(207) Taira, K.; Benkovic, S. J. Evaluation of the importance of hydrophobic interactions in drug binding to dihydrofolate reductase. *Journal of Medicinal Chemistry* **1988**, *31*, 129-137.

(208) Chen, J. T.; Taira, K.; Tu, C. P.; Benkovic, S. J. Probing the functional role of phenylalanine-31 of Escherichia coli dihydrofolate reductase by site-directed mutagenesis. *Biochemistry* **1987**, *26*, 4093-4100.

(209) Taira, K.; Chen, J. T.; Fierke, C. A.; Benkovic, S. J. Protein engineering of dihydrofolate reductase. pH dependency of of Phe-31 mutants. *Bull. Chem. Soc. Jpn.* **1987**, *60*, 3025-3030.

(210) Nagel, Z. D.; Meadows, C. W.; Dong, M.; Bahnson, B. J.; Klinman, J. P. Active site hydrophobic residues impact hydrogen tunneling differently in a thermophilic alcohol dehydrogenase at optimal versus nonoptimal temperatures. *Biochemistry* **2012**, *51*, 4147-4156.

(211) Battye, T. G.; Kontogiannis, L.; Johnson, O.; Powell, H. R.; Leslie, A. G. iMOSFLM: a new graphical interface for diffraction-image processing with MOSFLM. *Acta Cryst. D.* **2011**, *67*, 271-281.

(212) Chen, V. B.; Arendall, W. B.; Headd, J. J.; Keedy, D. A.; Immormino, R. M.; Kapral, G. J.; Murray, L. W.; Richardson, J. S.; Richardson, D. C. MolProbity: all-atom structure validation for macromolecular crystallography. *Acta Crystallogr., Sect. D: Biol. Crystallogr.* **2010**, *D66*, 12-21.

(213) Case, D. A. AMBER 9. et. al University of California: San Francisco, 2006.

(214) Nobbmann, U.; Connah, M.; Fish, B.; Varley, P.; Gee, C.; Mulot, S.; Chen, J.; Zhou, L.; Lu, Y.; Sheng, F.; Yi, J.; Harding, S. E. Dynamic light scattering as a relative tool for assessing the molecular integrity and stability of monoclonal antibodies. *Biotechnol Genet Eng* **2007**, *24*, 117-128.

(215) Stojkovic, V.; Gahkar, L.; Kohen, A. unpublished results.

(216) Mazumder-Shivakumar, D.; Kahn, K.; Bruice, T. C. Computational study of the ground state of thermophilic indole glycerol phosphate synthase: Structural alterations at the active site with temperature. *J. Am. Chem. Soc.* **2004**, *126*, 5936-5937.

(217) Laskowski, R. A.; Swindells, M. B. LigPlot+: multiple ligand-protein interaction diagrams for drug discovery. *J. Chem. Inf. Model.* **2011**, *51*, 2778-2786.

(218) Maglia, G.; Allemann, R. K. Evidence for environmentally coupled hydrogen tunneling during dihydrofolate reductase catalysis. *J. Am. Chem. Soc.* **2003**, *125*, 13372-13373.

(219) Boekelheide, N.; Salomón-Ferrer, R.; Miller, T. F. Dynamics and dissipation in enzyme catalysis. *Proc. Natl. Acad. Sci. USA* **2011**, *108*, 16159–16163.

(220) Pisliakov, A. V.; Cao, J.; Kamerlin, S. C.; Warshel, A. Enzyme millisecond conformational dynamics do not catalyze the chemical step. *Proc. Nat. Acad. Sci. USA* **2009**, *106*, 17359-17364.

(221) Liu, H.; Warshel, A. The catalytic effect of dihydrofolate reductase and its mutants is determined by reorganization energies. *Biochemistry* **2007**, *46*, 6011–6025.

(222) Dametto, M.; Antoniou, D.; Schwartz, S. D. Barrier crossing in dihydrofolate reductase does not involve a rate-promoting vibration. *Mol. Phys.* **2012**, *110*, 531-536.

(223) Miller, G. P.; Benkovic, S. J. Strength of an interloop hydrogen bond determines the kinetic pathway in catalysis by *Escherichia coli* dihydrofolate reductase. *Biochemistry* **1998**, *37*, 6336-6342.

(224) Venkitakrishnan, R. P.; Zaborowski, E.; McElheny, D.; Benkovic, S. J.; Dyson, H. J.; Wright, P. E. Conformational changes in the active site loops of dihydrofolate reductase during the catalytic cycle. *Biochemistry* **2004**, *43*, 16046-16055.

(225) Adamczyk, A. J.; Cao, J.; Kamerlin, S. C. L.; Warshel, A. Catalysis by dihydrofolate reductase and other enzymes arises from electrostatic preorganization, not conformational motions. *Proc. Nat. Acad. Sci. USA* **2011**, *108*, 14115-14120.

(226) Benkovic, S. J.; Hammes-Schiffer, S., Dihydrofolate reductase: hydrogen tunneling and protein motion In *Hydrogen-Transfer Reactions*; Hynes, J. T., Ed.; Wiley-VCH Verlag GmbH & Co. KGaA: Weinheim, Germany, 2007; Vol. 4, p 1439-1454.